DESIGN FOR METROLOGY OF FREEFORM OPTICS

by

Kristen Venditti

A thesis submitted to the faculty of
The University of North Carolina at Charlotte
in partial fulfillment of the requirements
for the degree of Master of Science in
Mechanical Engineering

Charlotte

2020

Approved by:

_____
Dr. Christopher J. Evans

_____
Dr. Matthew A. Davies

_____
Dr. Edward P. Morse

ABSTRACT

KRISTEN VENDITTI. Design for metrology of freeform optics. (Under the direction of DR. CHRISTOPHER J. EVANS)

Freeform optics offer significant advantages over the conventional aspheric optics, but pose new challenges in metrology and manufacturing. The spatial frequencies of an optical surface that must be measured have changed due to the progression of the manufacturing processes. Unlike aspheres or elements of conventional optical systems, surface prescriptions of freeform optics do not define an optical axis. Therefore, coordinate systems for the freeforms must be established with respect to the fiducials and datums, which must be realizable at all stages of manufacturing. Concurrent engineering suggests that optical designers consider “design for metrology” with fabricators and metrologists to engage during the earlier stages of design.

Multiple metrology methods applicable to freeform optics exist, however there are no standardized descriptions of their capabilities. In this thesis is one approach to providing “design for metrology” data that allows for intercomparing alternate metrology methods and for characterizing the performance of metrology instruments with respect to freeform optics.

ACKNOWLEDGEMENTS

My deepest gratitude goes to my advisor, Chris Evans, for his guidance, support and patience throughout the last three years. I want to thank him for asking the question while I was in undergrad, “have you considered graduate school?” It has been a privilege learning from him with such insight and knowledge of metrology and optical fabrication. He has given me the opportunity to work on various projects, which allowed me to gain some experience and knowledge in these areas, and for that, I am extremely grateful.

I would like to thank my committee members, Dr. Matt Davies – for all his efforts to fabricate the round robins and Dr. Ed Morse – for our conversations involving CMM capabilities/limitations and for both accepting to be part of my committee.

I also appreciate the support from the industry affiliates and the funding for this research by the Center for Freeform Optics (CeFO). It has been great experience presenting and gaining feedback at the biannual IAB meetings. I’m also thankful for the meetings with the mentors that assisted in this project on a monthly basis; your input has been invaluable.

Many thanks for the support from the Center for Precision Metrology (CPM), including Dr. Jimmie Miller for helping me with the DMI experiments on the NexView and to Mr. Greg Caskey for teaching me how to use the NexView and helping with experiments on the Mahr LD 260.

I would also like to thank Jennifer Chastain and Tracy Beauregard for always making my life easier when it came to the administrative work.

To all my friends and colleagues in the ME and Optics department, it has been so much fun learning with and from all of you. Sam, thank you for helping with the elevator experiments. Suba, I am grateful for all our conversations in optics.

To my mom and all of my family, thank you for your love and encouragement.

To Noël and Pika, I am grateful for you.

TABLE OF CONTENTS

LIST OF TABLES

LIST OF FIGURES

LIST OF ABBREVIATIONS

AHM	Average height map
BS	Beam splitter
CCD	Charge-coupled device
CD	Capability diagram
CEFO	Center for Freeform Optics
CGH	Computer generated hologram
CMM	Coordinate Measuring Machine
CSI	Coherence Scanning Interferometer
CTE	Coefficient of thermal expansion
DAQ	Data acquisition
DCH	Duke Centennial Hall
DMI	Displacement measuring interferometry
f/#	Ratio of focal length divided by aperture
FFT	Fast Fourier Transform
FOMCD	Freeform optic metrology capability diagram
FOV	Field of view
GCD	Global capability diagram
HeNe	Helium Neon
ITF	Instrument transfer function
MSF	Mid-spatial frequency
MTF	Modulation transfer function
MWI	Multi wavelength interferometry

NA	Numerical aperture
NiP	Nickel Phosphorous
OPD	Optical path difference
PSD	Power spectral density
PSF	Point spread function
PSI	Pounds per square inch
PV	Peak-to-valley
PZT	Piezoelectric transducer, or lead zirconate titanate (Pb[Zr(x)Ti(1-x)]O3), is one of the world's most widely used piezoelectric ceramic materials
SWLI	Scanning White Light Interferometer
R/#	Ratio of the ROC divided by the clear aperture of the spherical surface
RMS	Root mean square
ROC	Radius of curvature
RR	Retroreflector
RRF	Round robin freeform
STR	Surface topography repeatability
TF	Transmission flat
TS	Transmission sphere
TWI	Tilted wave interferometry
WD	Working distance
λ	Wavelength (of light or surface spatial wavelength)
λ_{max}	Longest spatial wavelength measurable/lateral range (FOMCD)
λ_{min}	Shortest spatial wavelength measurable (FOMCD)

CHAPTER 1: BACKGROUND AND MOTIVATION

1.1 Introduction

Freeform optical surfaces are revolutionizing the optics industry with emerging design forms that allow improved performance and more compact designs for a given optical function [1]. Advancements in optical design have been made, posing new challenges in manufacturing and metrology as tolerances on freeforms have become more demanding. Manufacturing processes include ultra-precision machines, such as diamond turning and milling, sometimes in combination with a deterministic polishing process like computer-controlled polishing or magnetorheological finishing [2], [3]. Further development of these processes together with optical design have enabled optical surfaces to have no axis of invariance on or off the part [4].

Since a freeform does not have an “optical axis”, a “reference axis” is defined by ISO 10110-19 as a “theoretical axis given by the optical designer which does not depend on the symmetries of the surface and usually represents the center of the optical path for the main function”. The standard continues, “…The position and orientation of the reference axis is defined by measurable references at and/or on the general surface/component or by an approximation of the nominal surface” [5]. Therefore, according to the standard, the realization of the coordinate systems of the optical surface has some uncertainty from use of fiducials, datums and/or other references or tolerances in positioning the surface with respect to the reference axis. Multiple coordinate systems that are not physical may be established for the sole purpose of machining or measuring systems.

Producing these complex optical surfaces calls for concurrent engineering, specifically concurrent optical design, design for manufacture, design for metrology and design for assembly, which are all required for appropriate allocation of tolerances [6]. The goal of this project is to provide collated, curated[1] data to optical designers, fabricators and metrologists to enable them to identify early in the process if a part can be measured adequately and cost effectively using existing metrology capabilities. This suggests an approach using a hierarchical data structure of metrology tools and their ability to measure form, mid-spatial frequencies (MSF) and surface finish. The data structure could be realized as a web page, in a database, or – as described here and separately implemented – in a document with links to navigate between levels.

1.2 “Design for metrology” data structure

The design for metrology document, a hierarchical database, covers a large spectrum of metrology instruments. This project is a collaboration with University at Rochester (UR), which was funded by CeFO affiliates. It begins with level 1 (top level), an overview of the generic metrology instruments using the Global Capability Diagram (GCD) further explained in SECTION 1.5. These generic instruments are currently categorized as:

a. Scanning White Light Interferometers (SWLIs)

b. Profilometers

c. Coordinate Measurement Machines (CMMs)

d. Interferometers

e. Single Beam Instruments.

[1] Data may be sourced from measurements made for the purpose, from literature, or from instrument manufacturers; the source of all data is identified.

Given a freeform to measure, one could choose an appropriate class of metrology instruments from the GCD that leads to level 2 with more details of that particular generic technology. Level 2 focuses on the “use case” of the generic system along with the suitable measurands and constraints. It also lists commercially available systems, which leads to level 3 containing specific vendor data. The specific instruments comprise commercially available systems that are located at UNCC, other CeFO affiliate sites, in industry and systems in development at UNCC and UR (also independently funded by CeFO). The list includes, but is not limited to:

1. Zygo NexView [7]
2. Zygo Zegage [8]
3. Mahr LD 260 [9]
4. OptiTrace 5000 [10]
5. Taylor Hobson Form Talysurf PGI Matrix [11]
6. Taylor Hobson Form Talysurf PGI Freeform [12]
7. Panasonic UA3P – 500H High Accuracy Equipment [13], [14]
8. Panasonic UA3P – 4000 Large Scale Equipment [14]
9. Zeiss Prismo Navigator [15]
10. Zeiss F25 [16]
11. Leitz PMM-F [17]
12. Moore UM 100 (in development at UNCC) [18]
13. UltraSurf 5x [19]
14. Zygo Fizeau HD [20]
15. Zygo Fizeau AT [manufacturer data no longer posted]

16. Cascade optical coherence tomography (in development at UR) [21]
17. Multi wavelength interferometer (in development at UR) [22]
18. Reconfigurable Computer-generated hologram (CGH) using spatial light modulation (in development at UR) [23]
19. Transverse Translation Diverse Phase Retrieval (in development at UR) [24]
20. Phasics SID4-HR [25]

Level 3 data starts with a visual of the instrument's capabilities and limitations with either a "Freeform Optics Metrology Capability Diagram" (FOMCD) or an illumination diagram. These diagrams are followed by experience data that is compiled through experiments with that particular instrument, which will also include measurements that will be done using two round robin freeforms (RRF). With the continuing CeFO funding, the "design for metrology" document is considered a "living document" in that further additions with other metrology instruments and emerging technologies will be made to current database.

1.2.1 Measuring RRFs

Measuring the RRFs was a second project launched during the ongoing "design for metrology" project (initial project), which officially became an extension. The goal of this second project is to intercompare measurements of 2 nominally identical sub-100 mm aperture concave freeform mirrors made on the same machine tool by two different operators three months apart. The parts will be measured using a wide variety of flexible metrology tools (having at least two of the same tool type at different locations) and to include this data in the "living document" alongside the experience data in level 3 of the hierarchy. A set of instructions were written for measuring the RRFs, logging the

temperature for drift tests and while measuring. RRF #1 can be measured using contact or non-contact measurement methods, but RRF #2 is strictly for non-contact measurement. Given that the RRF optical surfaces are electrodeposited nickel phosphorus (NiP), Hertzian stresses for the different size diamond and ruby styli were calculated and plotted for a quick reference for the participants to avoid stylus damage to RRF #1. Flexible guidelines to perform measurements were given, defining the measurands and uncertainties, but including metrologists' experience and expertise among the variables. Measurands and procedures defined are:

a. height map of deviations from prescription that include the parameters peak-to-valley (PV) and root mean square (RMS)
b. measure form and if possible, MSF at the center defect
c. filtering the measurements and fitting up to a third order spherical using the Zernike fringe coefficients
d. record measurement times

And defining the measurements:

a. 24-hour drift test with temperature logging
b. minimum of two nominally identical form measurements with temperature logging by the same operator for testing repeatability
c. if time permits, a third measurement made the following day by second operator for testing reproducibility

At the time of writing this thesis, both RRFs were measured at UNCC and sent to two different CeFO affiliates for measurements.

1.3 Outline of thesis

The remainder of Chapter 1 continues with guides to understanding an FOMCD (level 3), GCD (level 1) and illumination diagram (level 3) in detail that are within the data structure developed. There's also an example of how an optical designer or fabricator might navigate through the hierarchy given a specification to determine if there is an available, adequate metrology solution. Chapters 2 – 4 describe the development of three example data sets, first explaining the generic class of instruments (level 2) followed by an FOMCD and/or an illumination diagram (level 3) for each specific metrology instrument. Chapter 2 focuses on SWLIs, drilling down to detailed experiments (level 3 experience data) showing specific, previously unpublished, spatially correlated contributions to Type A uncertainty evaluation when measuring diamond turned surfaces. Chapter 3 takes a similar approach to measurement of diamond machined freeform optics using a stylus profilometer. Here the detailed experiments focus on the consequences (but not the detailed theory) of the interaction of probes with the optical surfaces. Handbook values of yield stress ignore work hardening, and possible metallurgical transformations in diamond turning of ductile metals. The resulting plastic deformation, when styli with probe radii that are similar to the tool nose radius, are surprising. Chapter 4 addresses the use of Fizeau interferometry starting off with both an FOMCD for transmission flats and an illumination diagram for transmission spheres, also looking into detailed experiments with Type A uncertainty and retrace errors. Chapter 5 offers concluding remarks and suggestions for future work.

1.4 A guide to understanding the FOMCD

Mathematically influenced by the Stedman diagram [26] and building upon previous work [27], the FOMCD or simply Capability Diagram (CD) plots the resolution and range of an instrument. These limits result in a polygon in amplitude wavelength space. The log-log axes represent sag (Z), the departure from the reference, as a function of aperture (λ), the projected maximum dimension of the optic under test (FIGURE 1). These terms are more familiar to optical designers and fabricators than the Fourier representation Stedman originally proposed and hence more appropriate for this use. It is also important to note that the CD assumes smooth, continuous surfaces, especially for optical measurement methods. The CD should be used with caution (if at all) when considering surfaces that give stronger diffraction effects [28].

The Z direction is parallel to the reference axis of a freeform optical surface, as defined in ISO 10110 Part 19 [5] and cited in section 1.1 above. For a spherical element or rotationally invariant aspheric surface, according to ISO 10110 Part 12 [29], the reference axis would be the optical axis. In CDs, Z_{max} represents the maximum measurable sag. Z_{min} can be understood, conceptually, as the resolution in the Z direction. However, a more appropriate term for many instruments is the noise floor, which depends of averaging time [30]. ISO 25178 Part 604 [31] defines surface topography repeatability (STR) as: “repeatability of topography map in successive measurements of the same surface under the same conditions of measurement” or measurement of noise.

The lateral resolution and range of an instrument are defined by λ_{min} and λ_{max} respectively. These limits can be understood by considering the surface profile to be measured as the sum of sine waves, i.e. in the Fourier domain. Like Stedman diagrams,

the CD assumes a smooth continuous surface that is described by the sum of sinusoidal surface profiles: $z_i = A_i /2 \sin(2\pi x/\lambda)$. λ_{min} is the minimum resolvable spatial wavelength, which depending on the specific instrument and its limiting case may be defined by the Nyquist limit (2 pixels per one period cannot be resolved), optical resolution (Rayleigh or Sparrow criterion), the "spot size" of an optical probe or the radius of curvature (ROC) of a probe contacting the surface.

Conceptually, λ_{max} represents the maximum measurable aperture, not the longest wavelength sine wave measurable. Freeform (and other) optical surfaces may have components such as astigmatism or third order spherical aberration which can – and must – be measured on instruments discussed here, but which are not sensibly described by long wavelength Fourier components.

Two further limits to the polygon are surface slope and curvature, respectively Θ_{max} and C_{max}, which are found by taking the first and second derivative of the sinusoid equation and finding the maxima of each, resulting in equations:

$$z = \frac{\Theta_{max}\,\lambda}{\pi}$$

$$z = \frac{C_{max}\,\lambda^2}{2\pi^2} \text{ where } C_{max} = \frac{1}{R_{min}}$$

Θ_{max} may be the flank angle of a contact probe or the steepest resolvable slope of an optical probe or objective. C_{max} is the reciprocal of the minimum radius of a contact probe.

FIGURE 1 shows a generic CD; with a specific instrument, the CD has an accompanying table with numeric values for the limits, the source of the information and/or how it was calculated. Note that the limits plotted appear as hard limits, but in practice, they are more nuanced or may be better expressed as "fuzzy boundaries". For

example, Z_{min} (the minimum sag or vertical resolution) for a Scanning White Light Interferometer (SWLI) is, in practice, noise limited. Trading off resolvable amplitude with increased measurement time by averaging pushes down the minimum vertical resolution. At the same time, the minimum spatial wavelength "measurable" in a SWLI depends on instrument design and objective lens used. At the highest spatial frequencies, the instrument transfer function shows that the ratio of "true" to measured amplitude decreases as the spatial frequency approaches the Nyquist limit [32]. The measurement may be optics limited or detector limited. Dynamic range may be expanded by stitching.

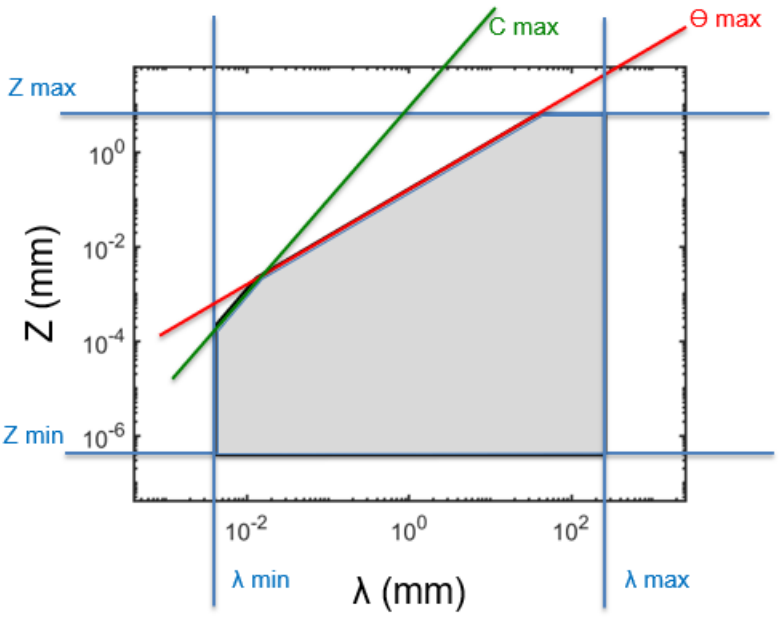

FIGURE 1: Generic Capability Diagram

λ_{min}: lateral resolution of probe/stylus or objective

λ_{max}: lateral range of instrument

Z_{min}: vertical resolution or "noise level" of the instrument

Z_{max}: vertical range of instrument

C_{max}: sharpest curvature, reciprocal of the radius

Θ_{max}: steepest slope

1.5 Global Capability Diagram (GCD)

The GCD (level 1) depicts an overview of all the generic instrument's CDs in one plot categorized as SWLIs, Profilometers, Coordinate measuring machines (CMMs), and Interferometers (FIGURE 2). At the time the GCD was developed, the maxima and minima limits (TABLE 1) are from instruments that are commercially available at the Center for Freeform Optics (CEFO) sites. Limits and even categories of instruments may expand as new technologies are developed.

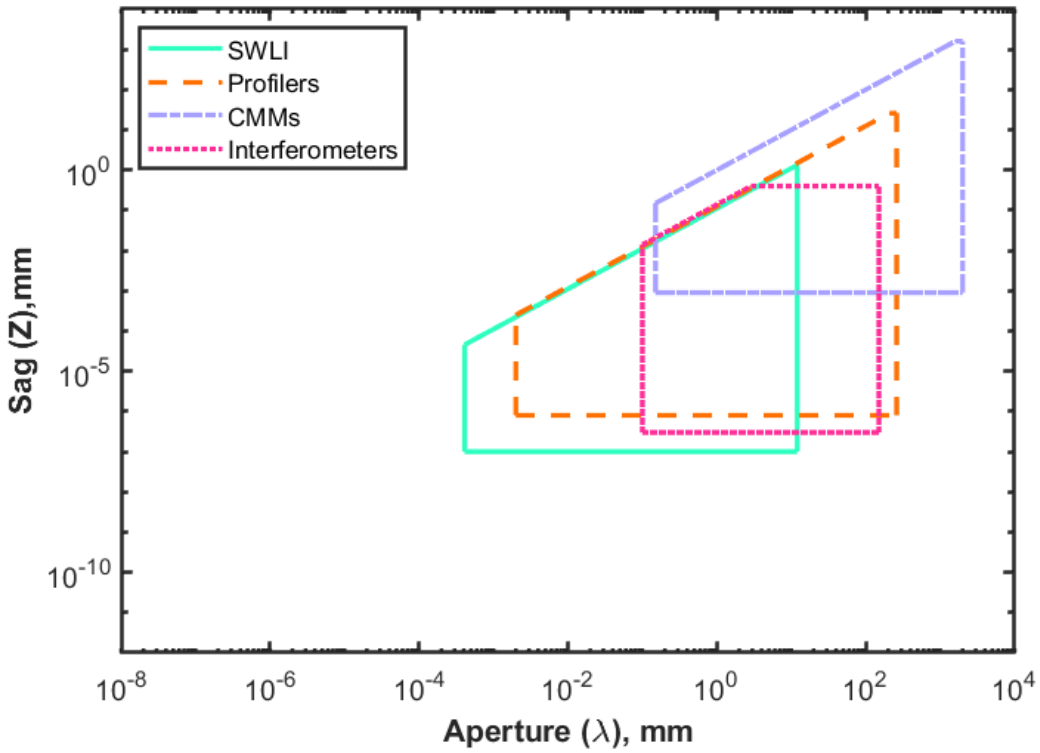

FIGURE 2: Global Capability Diagram

TABLE 1: Generic instrument's parameters

	λ_{min} (µm)	λ_{max} (mm)	Z_{min} (nm)	Z_{max} (mm)	Θ (deg)
SWLIs	0.41[a]	12[b]	0.1[c]	20[d]	40[e]
Mechanical Profilers	2[f]	260	0.8[g]	26	45
CMMs	15[h]	2000[i]	900[j]	1600[k]	-
Interferometers	100[l]	150[m]	0.3[n]	0.4[o]	50[p]

The limits listed in (TABLE 1) were obtained by the:

a. Optical resolution based on 100x objective, calculated using Rayleigh criteria
b. Single field of view based on 1.4x objective with 0.5x tube lens
c. Surface topography repeatability (STR) from single measurements [7]. Note that reported STR values depend on a number of factors including the roughness of the surface being measured and the details of the measurement procedure
d. Commercially available capability based on extended scan length; may be relevant in stitching for freeform optics
e. Based on Zygo NexView 100x Mirau objective, where slope is limited by Nyquist limit; some systems capture scattered light to increase slope limit
f. ROC of commercially available diamond styli
g. Mahr probe system resolution [9]. Other commercially available systems may have different zmin
h. Smallest stylus radius for Zeiss Prismo Navigator at UNCC
i. Largest circular aperture measurable using Leitz PMM-F at UNCC
j. First term of the Maximum Permissible Error (MPE) for length measurement, E0, of the Zeiss Prismo 7 Navigator with the VAST gold probe at UNCC, according to ISO 10360-2 [33], [34]

k. 1600 mm measurable using Leitz PMM-F at UNC, although unlikely to be required even for a 2000 mm aperture surface.

l. Instrument transfer function (ITF) measurement results using Zygo Fizeau Verifire HD [35]

m. Commercially available, converging, transmission spheres [36]

n. Rms wavefront repeatability using Fizeau Verifire HD [20]

o. Departure from the reference using Zygo Verifire HD at UNCC, based on HeNe illumination, 1000 fringes/aperture, 2300 x 2300-pixel detector

p. Maximum slope of the fastest commercially available transmission sphere f/.65 [36]

1.6 A guide to understanding the Illumination Diagram

Some instruments do not operate within a physically limited measurement volume in a way that makes it difficult to represent the performance limits in the implied cartesian coordinate system of an FOMCD, hence the illumination diagram may be required for such optical measurements. One example is a Fizeau interferometer with a transmission sphere (TS); FIGURE 3 is specifically for a nominal 100 mm aperture Fizeau interferometer, showing part aperture as a function of part radius of curvature (ROC) and is based on given f/# for a TS. When measuring freeform optics, some auxiliary null optics are required to match the test wavefront with the surface prescription. Nulls are also required for many aspheres. For a detailed discussion see, for example, Chapter 12 in Optical Shop Testing [37]. For the illumination diagram, Computer-Generated Hologram (CGH) with a mount that takes up 100 mm of spacing within the cavity is assumed (assumption #1). The TS f/# converts to illumination cones. For concave surface testing, a physical limitation of 2 m for the table on which the

interferometer sits is also assumed (assumption #2). Otherwise, these illumination beam lengths would be constrained on the right side by the coherence length of the source and turbulence.

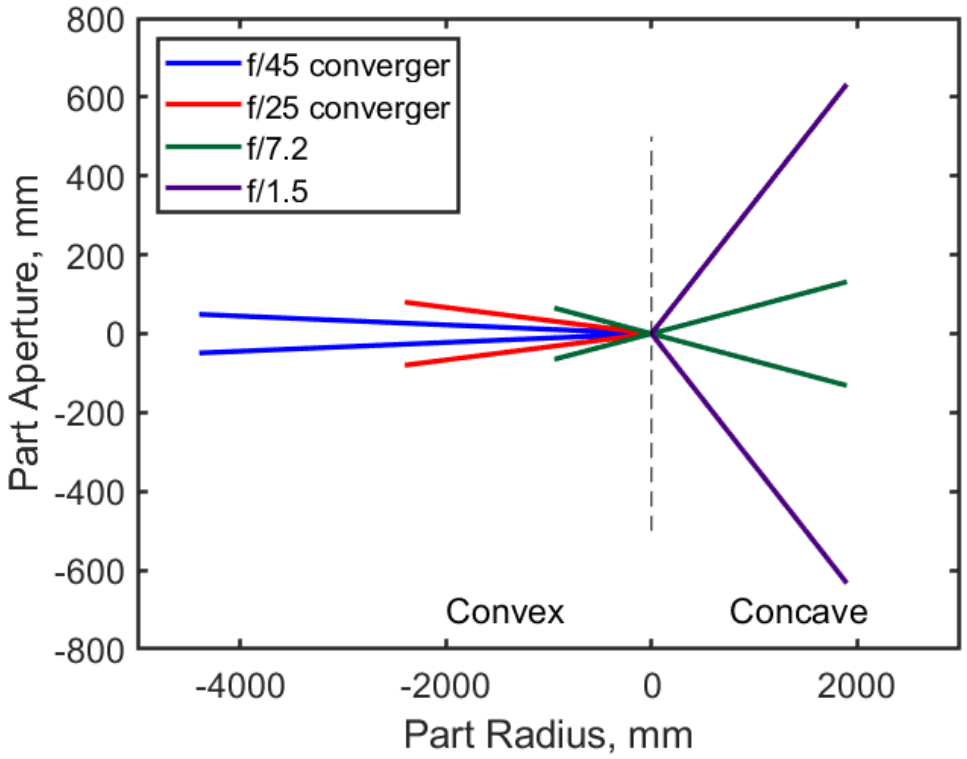

FIGURE 3: Illumination Diagram of a Fizeau with Transmission Spheres

Very low NA single element transmission spheres, sometimes known as "convergers" and "divergers" are commercially available with f/#s ranging from f/80 to f/15. This diagram shows two convergers and a slow (f/7.2) TS on the left, which have the ability to measure convex parts. Considering the f/45 converger with 100 mm aperture and again, assuming that 100 mm of space along the interferometer's optical axis is required for a CGH and mount, then 96 mm aperture convex freeforms with a base ROC less than 4400 mm can be measured [36]. Using an f/25 converger and a CGH (with

the same assumptions about space) allows measurement of 160 mm aperture convex freeforms with a ROC of 2400 mm or less [36]. As the ROC decreases, so does the testable aperture. More conventional, multi-element TS with an aplanatic reference element have limitations for measuring convex surfaces, imposed by the numerical aperture, the ROC of the reference surface (for smaller apertures) and the mechanical design of the housing [36]. A 150 mm nominal aperture f/7.2 with a CGH (same assumptions as above) can measure a 130 mm aperture convex freeform with a radius of 945 mm. Note that these limits can be expanded using additional optics in the test cavity.

The right side of FIGURE 3 is an illustration of a fast (f/1.5) and slow (f/7.2) TS used to measure concave parts. Again, assuming the space of the CGH and now the length of the table, an f/7.2 can measure up to a 263 mm aperture concave freeform with a ROC of 1900 mm. An f/1.5, with same assumptions, can measure up to a 1266 mm aperture concave freeform with a ROC of 1900 mm as well.

Although not shown in FIGURE 3, is the zone around the TS internal cavity focus (for “conventional” TS) where it is impossible to focus properly [38]. The size of that zone depends on the TS and the design of the internal optics and focus system of the Fizeau. It should also be noted that FIGURE 3 shows a small fraction of the TSs that are, and have been, commercially available from various sources over the last 2 decades; the detailed design of each TS affects the characteristics discussed above. Also, the illumination diagram does not capture λ_{min}, Z_{min}, or Z_{max} from the CD. Additional work is required to provide a graphical representation of these limits.

1.7 Navigating the document

1.7.1 Optic example

Here is an optic with the following specifications:

- diamond turned plano concave optic
- aperture 40 mm
- sag +0.004 mm
- want to analyze finish (i.e. roughness, cutoff 2.5 – 80 µm per ISO 10110 – 8 [39])

Based on the specifications and starting at the top of the hierarchy at level 1 with the GCD (in FIGURE 4), the SWLIs or Profilers are chosen indicated by the black circle.

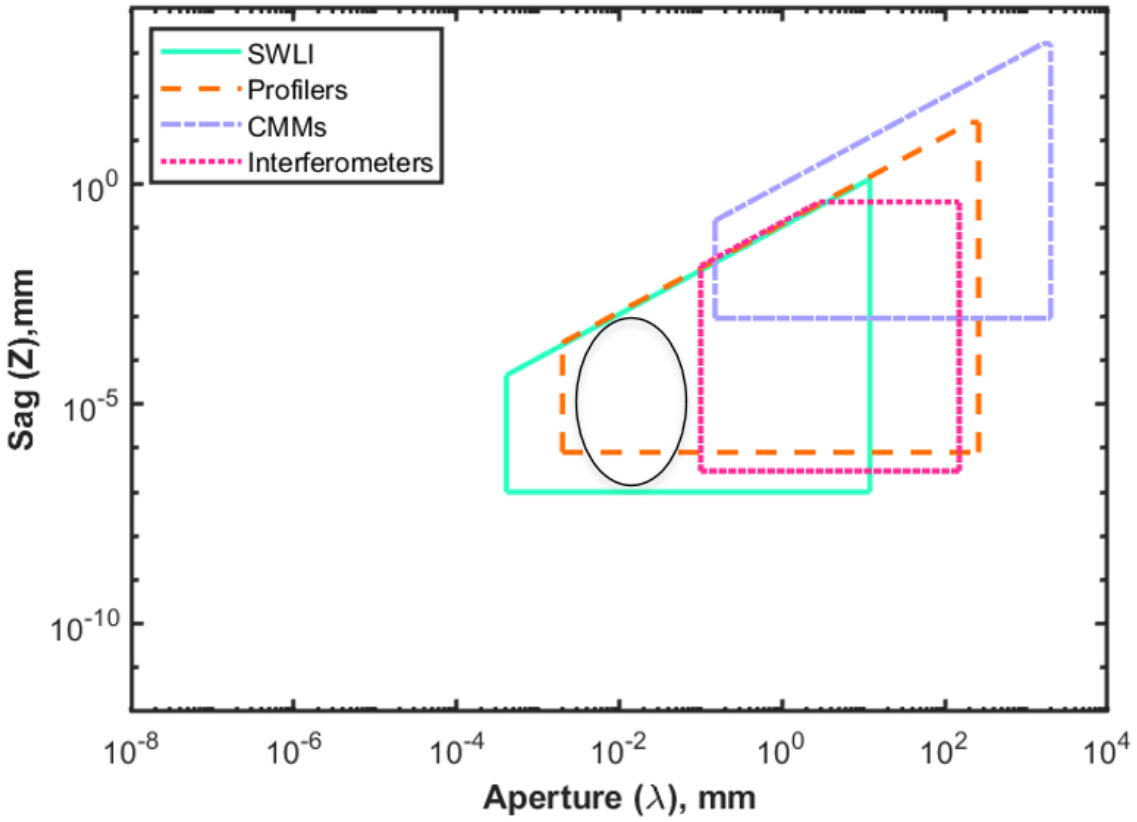

FIGURE 4: GCD showing approximate region of interest

Beginning with the first option, SWLIs, would lead to more detail in level 2, which shows that the use case of measuring finish is satisfied. Stitching is also described, which may be a viable option in obtaining the full aperture if necessary. So, from level 2, a specific SWLI such as the NexView may be chosen. Looking further into its FOMCD in level 3 with the available objectives (FIGURE 5), it appears that the 10, 20x and 50x may be an option, but the 2.75x does not cover the highest spatial frequency (2.5 µm).

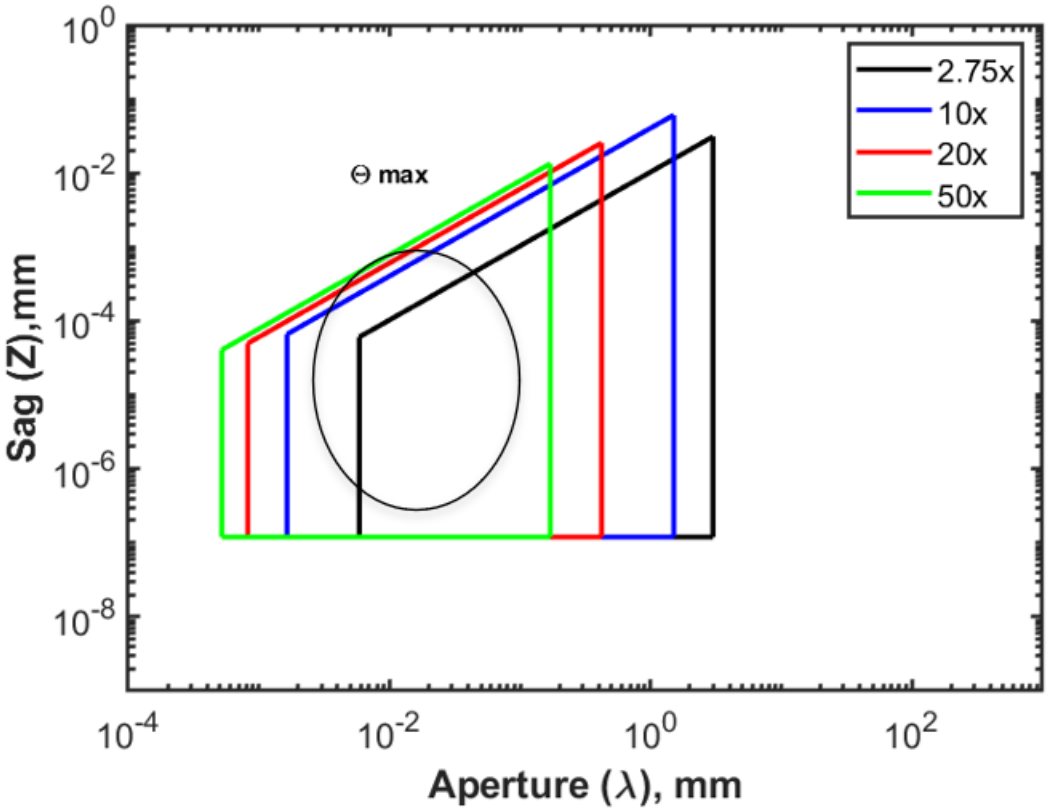

FIGURE 5: FOMCD for the NexView with the available objectives at UNCC

Choosing profilers as a second option from the GCD would lead to level 2 data, which also satisfies the use case of measuring roughness. In this section, a specific profiler is selected, the Mahr LD 260 for instance, which leads to level 3. It has an

FOMCD for the Mahr at UNCC (FIGURE 6), which shows us that the diamond stylus would be the tool for performing the roughness measurements.

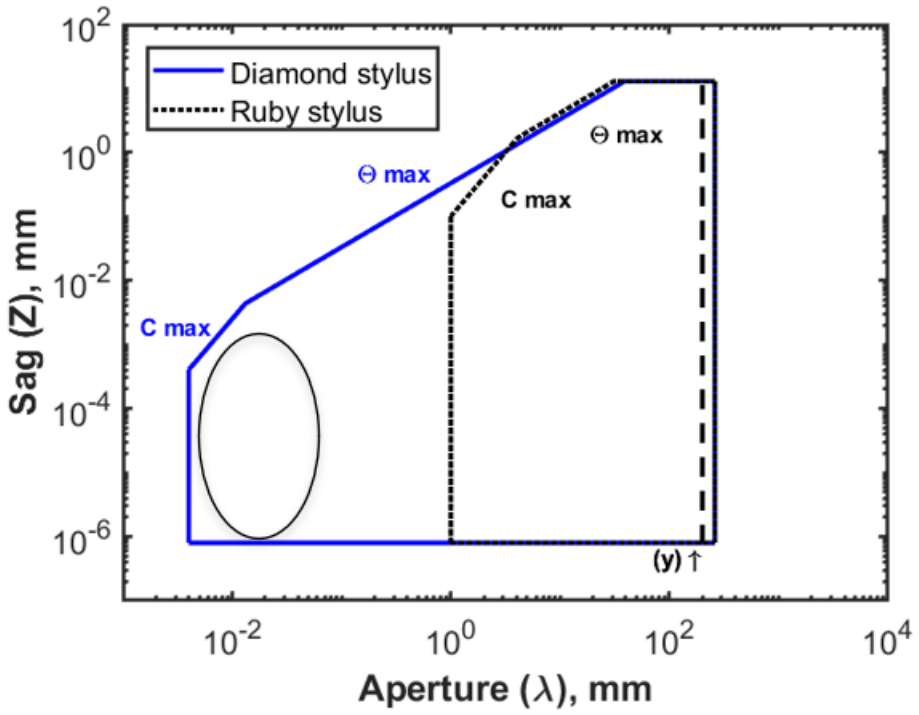

FIGURE 6: Mahr LD 260 with its styli at UNCC

Level 3 points out that one of the issues to consider is Hertzian stress. There are examples in the experience data that show the Hertzian stress as a function of load for different materials.

CHAPTER 2: CHARACTERIZING AND TESTING SCANNING WHITELIGHT INTERFEROMETERS (SWLI), SPECIFICALLY USING THE ZYGO NEXVIEW

2.1 Introduction to scanning white light interferometry, exemplary level 2 data

SWLI (also known by a number of other names including Coherence Scanning Interferometer or CSI [40]) is a class of interference microscope-based instruments that perform surface height measurements using a broad-band illumination (white light) source. The objective typically scans vertically splitting the light into two beams, one to the part under test and the other to the reference mirror where both reflect back and recombine to get interference fringes. The z-position or height at each pixel on the surface is found by one of many analyses of the intensity within the modulation envelope [40]. For freeform and other optics applications, these instruments operate within the "smooth surface limit" where metrological behavior is well approximated by linear systems theory [41]. For "smooth" surfaces, SWLI instruments may provide measurements of amplitude parameters defined in ISO 10110-8 [39] and ISO 25178 -2 [42] with uncertainties well below 1 nm for amplitude parameters in well controlled environmental conditions. Software supplied with commercial instruments frequently provides power spectral density (PSD) plots enabling evaluation of PSD limits according to ISO 10110-8 and a variety of other measurands. At the time of writing, no commercial instrument (to our knowledge) provides software allowing evaluation of MSF errors using expansions to high orders of Forbes (Forbes – polynomials on steroids) [43] or Zernike polynomials [44] or the structure function [43], [44].

SWLIs are used for areal measurements of finish and mid-spatial frequencies (MSFs). Characterizing MSFs on freeform optics (over a spatial period of 0.08 – 2.5 mm

[39]) with significant departure from a plane surface entails a higher numerical aperture (NA) with stitching [45]. Form can also be measured by SWLIs with limitations on the aperture's size and slope again using stitching. In order to measure surfaces with steep slopes, a high magnification objective must be selected, resulting in reduced field of view (FOV). The FOV limitation is one of the "fuzzy boundaries", which is extended by stitching together multiple measurements. Measurement time increases with the number of stitched measurements introducing uncertainties in the measurement results [46], [47]. For instance, as the slopes in a measurement increase so do the comatic errors that also lead to a greater magnitude of form errors post-stitching [45] as well as quadratic errors associated with quadratic bias in the reference surface calibration [48].

In addition to limits on measurable aperture, the SWLI instrument's structural and mechanical design can limit the optic's size and weight. Other instrument types have the ability to measure large optics [49], [50], in situ [51], where refined replication methods have been used [52]. The earliest commercially available instruments of this type used "phase shifting" technology, i.e. longer coherence length sources and relatively small number of intensity frames [53].

2.2 FOMCD for Zygo NexView, exemplary level 3 data

The Zygo NexView, located in the Metrology Suite at Duke Centennial Hall (DCH) has 4 different objectives: 2.75x (Michelson), 10x (Mirau), 20x (Mirau) and 50x (Mirau), which depict the FOMCD in FIGURE 7 with the corresponding numerical values in TABLE 2. All FOMCDs were created in MATLAB with script available for the NexView FOMCD in Appendix A. Other objectives that are commercially available for NexView and similar SWLIs are the 1.4x (Zygo Wide-Field, ZWF), 5.5x (Michelson),

22x (Michelson) and 100x (Mirau). Higher magnification objectives have the ability to measure optical surfaces with steeper slopes in which the maximum slope is represented by θ_{max} (FIGURE 7). When measuring large departure freeforms, care has to be taken with higher magnification objectives since the working distance (WD) generally decreases (with the exception of 1.4x and 2.5x). It is important to note objectives that have similar magnification, such as the 20x and 22x (commercially available) differ significantly in terms of NA and slope acceptance. A Mirau type objective (such as 20x) does not have an internal beamsplitter cube whereas the 22x, a Michelson type objective, uses a beamsplitter and requires a longer working WD and therefore a lower NA and slope acceptance.

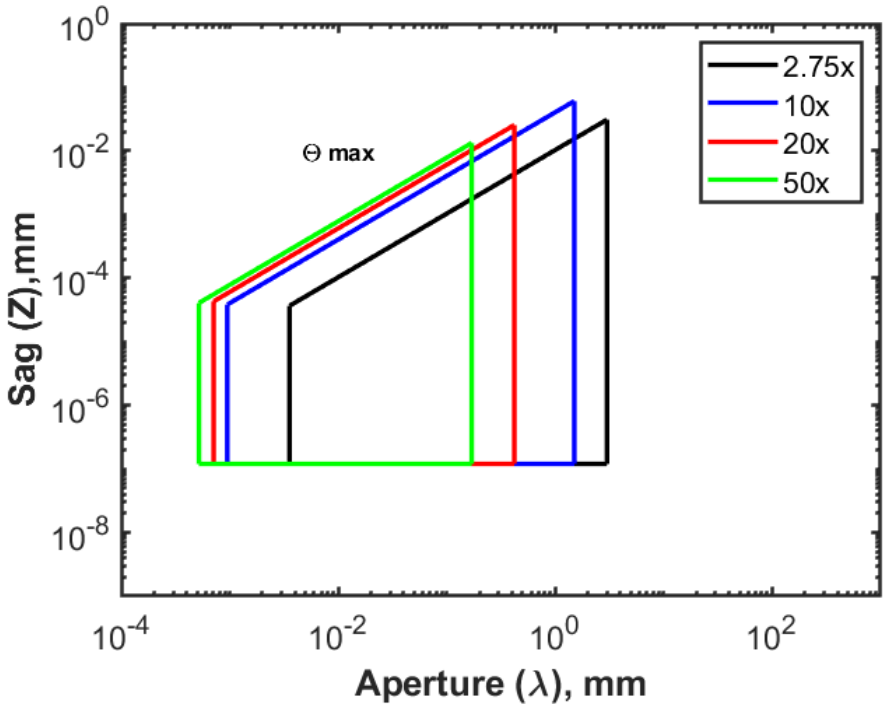

FIGURE 7: CD for Zygo NexView objectives available at UNCC

TABLE 2: Numerical limits for the Zygo NexView CD

	Unit	**2.75x**	**10x**	**20x**	**50x**
$\boldsymbol{\theta_{max}}$	(deg)	3.71	14.53	21.8	28.13
$\boldsymbol{\lambda_{min}}$	(μm)	5.86	1.64	0.82	0.52
$\boldsymbol{\lambda_{max}}$	(mm)	3	0.83	0.42	0.17
$\boldsymbol{Z_{min}}$	(mm)	0.1e-6	0.1e-6	0.1e-6	0.1e-6
$\boldsymbol{Z_{max}}$	(mm)	0.15	0.15	0.15	0.15

The lateral resolution of each objective, λ_{min}, is based on the diffraction limit (either the Nyquist limit or the Sparrow criterion). In ISO 25178-604, the instrument transfer function (ITF) describes how a SWLI responds to a surface (ratio of measured amplitude to true amplitude) as a function of frequency [31], [32]. The ITF will drop to zero at a higher spatial frequency, given by the Sparrow limit for the optical system or the Nyquist limit imposed by the detector. The Sparrow limit is the spacing of two discrete sources where there is no minimum in the center of the overlapping Airy disks ($0.47\lambda/NA$), i.e. the peaks cannot be distinguished. A more conservative value is given by the Raleigh criterion ($0.61\lambda/NA$), which gives the separation of two adjacent point sources where the peak intensity in the Airy disk overlaps the first minimum from the second source, where two point like emitters can be distinguished [54]. From an instrument user's perspective, it does not matter which is specified by an instrument manufacturer, as long as the choice is clearly stated.

According to NexView's objective chart, the manufacturer states the optical resolution for each objective based on Sparrow criterion and spatial sampling [55]. For the objectives with the magnification of 2.75x, 10x and 20x, the Nyquist limit (two pixels per sinusoidal period) is larger than the Sparrow criterion, hence making these objectives "detector limited". The resolution for the 50x objective is "optics limited" so λ_{min} for 50x

is defined by the Sparrow criterion. Notice when using the Rayleigh criterion, also listed in TABLE 3, that the 20x objective becomes “optics limited” when compared to the Nyquist. It is also important to note that changing the tube lens will only change the spatial sampling, not the optical resolution. If a ½ x tube lens is used, then Nyquist is larger for all objectives here and thus become “detector limited” when compared to either the Rayleigh or Sparrow criteria. If a 2x tube lens is used, then either the Rayleigh or Sparrow criteria is larger than Nyquist, resulting in all the objectives becoming “optics limited”.

TABLE 3: Optic vs detector limits for Zygo NexView at UNCC

Magnification	**2.75x**	**10x**	**20x**	**50x**
Optical Resolution - Rayleigh (um)	5.34	1.16	0.87	0.63
Optical Resolution - Sparrow (um)	3.56	0.95	0.71	0.52
Spatial Sampling at 1x (um)	2.93	0.82	0.41	0.17
Nyquist limit (um)	5.86	1.64	0.82	0.34
Optic vs Detector limited based on Rayleigh	Detector	Detector	Optic	Optic
Optic vs Detector limited based on Sparrow	Detector	Detector	Detector	Optic

The field of view (FOV) of an objective is represented by λ_{max}, the vertical boundary on the right of the polygon. As the magnification of the objective decreases, the FOV increases shifting each objective’s polygon to the right in FIGURE 7. The 2.75x (Michelson) objective has the largest FOV of 3 mm, which can be modified using 2x or

0.5x tube lenses to 1.5 or 6 mm respectively, changing the detector limit but not the optical resolution. It should be noted that Mirau based interferometric objectives partially obscure the FOV due to the presence of an internal reference mirror, this has no practical effect because it is a small deviation from Köhler (uniform) illumination across the field [56].

As mentioned in section 2.1, λ_{max} is considered a "fuzzy boundary" since stitching can extend this limit. Stitching with a high magnification objective would be a solution for a surface that has steep slopes and needs high resolution with a large FOV.

The vertical resolution of a SWLI is sometimes specified via the instrument's noise floor or Z_{min} in the FOMCD. A number of approaches have been described to quantify the "noise floor", with the result depending in detail on parameters of the evaluation (see Section 2.3 below). Surface Topography Repeatability (STR) has been considered as an instrument specification by some authors (de Groot), but more recently has been parsed to describe "instrument noise" and "measurement noise". Semantically, one cannot evaluate instrument noise without making a measurement.

Current ISO standards describe a variety of ways to quantify STR as a measure of the standard deviation per pixel (ISO 25178-600 and -604 [31], [57]) discussed more in detail in Section 2.3.1, STR is not yet a commonly used term among instrument manufacturers [58]. Building upon the current ISO standard, de Groot suggests that STR values should also include data acquisition rate and any filtering techniques [59]. The Z_{min} is another "fuzzy boundary" where averaging measurements reduces the noise (thus lowering the Z_{min}), but increases the time to acquire the measurement and hence susceptibility to thermal drifts. This boundary is also affected by filtering choices.

Z_{max} is the maximum vertical range of an instrument. For the NexView, the vertical scan range, using the Piezoelectric transducer (PZT) for the objective turret is the same for all objectives (0.150 mm). Combination of the PZT and the coarse stage extends scanning capability to 20 mm for higher sag parts. In the case of the NexView, θ_{max} and Z_{max} for the PZT combined give the peak in the diagram for each objective.

2.3 STR experiments using NexView, a continuation of level 3 data

2.3.1 STR background and the three different methods

Measurement noise is a metrological characteristic of systems that measure surface topography [58], [60]. STR is the measure of "noise" in repeat measurements of nominally the same interferometric cavity in an "ideal" environment. According to ISO [57], STR is a numerical value obtained by taking the difference of two repeat topography maps and then finding the root mean square (rms) and dividing by the square root of two [57]. Three different methods of STR are conducted during the analyses so the abovementioned (first method) is referred to as the subtraction method.

A second method, the synthetic reference, is also a numerical STR value with a series of steps. First the average height map (AHM) pixel by pixel from N number of measurements is found. The AHM is subtracted from each of the N measurements resulting in N difference height maps, then taking the root mean square (RMS) of each map to get multiple STR values, which are averaged to get a mean STR value.

The third method, generates a standard deviation map and is also known as Type A uncertainty map. The standard deviation is simply taken down the stack of N measurements pixel by pixel. It differs from the first two methods in that it provides a visual of the surface measurement, which may be more insightful than just a numerical

value. The mean of the uncertainty map is also calculated for comparison with the other two methods. A variety of other analyses can be applied to the uncertainty map. Since the first and second STR methods have multiple STR values from N measurements, they are also averaged to get a mean STR value for comparison purposes.

2.3.2 STR experimental setup and procedure

Three different nominally flat optics; a super polished Silicon Carbide (SiC), polished Fused Silica (FS) and diamond turned electrodeposited nickel (NiP) were measured using the Zygo NexView with the 2.75x, 20x and 50x objectives. The NexView is located in the Metrology suite in the Duke Centennial Hall Building, which is climate controlled (20C +/- 0.1C). In order to compute STR, 20 consecutive measurements were made at nominally the same spot on the optical surface[2] where there was a time delay of three seconds with a total data acquisition time of four minutes (approximately). The three different methods of STR were computed using MATLAB (Appendix B) and the 20 height maps (1024 x 1024 pixels) after piston and tilt were removed. A sanity check of the STR calculations in MATLAB was done by comparing the subtraction and calculation of height maps using Zygo's Mx software supplied with the instrument.

All the results reported here are computed after removal of piston and tilt. No further filtering was performed. Five data acquisition "runs" over a period of five nonconsecutive weeks. The specific run numbers are reported as these provide some explanation of run to run variability attributed to vibration, although the lab is well within the manufacturer's specifications.

[2] Differences in the center of the field of view for the 4 objectives in the turret of the NexView are included in the calibration file. Stage position is adjusted automatically when changing objective

2.3.3 STR results

Certain samples, such as the FS, were measured several times. For example, the first run (three second intervals, total data acquisition time of four minutes) resulted in similar STR values for the three methods, but different STR values across the different objectives (TABLE 4). While the STR values give quantitative data, the standard deviation maps reveal what may be happening with the surface measurement. Objectives 2.75x and 50x have higher STR values than the 20x, but the maps (FIGURE 8 (b) & FIGURE 9 (b)) show a spatial variation across the field. For the 2.75x measurements, all 20 measurements were loaded at once into the Mx software where each intensity map appears one after another revealing a change between one to two fringes for the 2.75x. The ratio of the fringes in the standard deviation map (FIGURE 8 (b)) to the intensity map fringes are nearly 2:1 indicating vibration[3].

TABLE 4: Run 1, FS STR values for each objective

	2.75x	**20x**	**50x**
Subtraction Method	0.17 nm	0.07 nm	0.11 nm
Synthetic Reference	0.19 nm	0.07 nm	0.13 nm
Standard Deviation Map	0.18 nm	0.07 nm	0.13 nm

[3] Personal discussions with C.J. Evans reviewing the data, based on previous experience

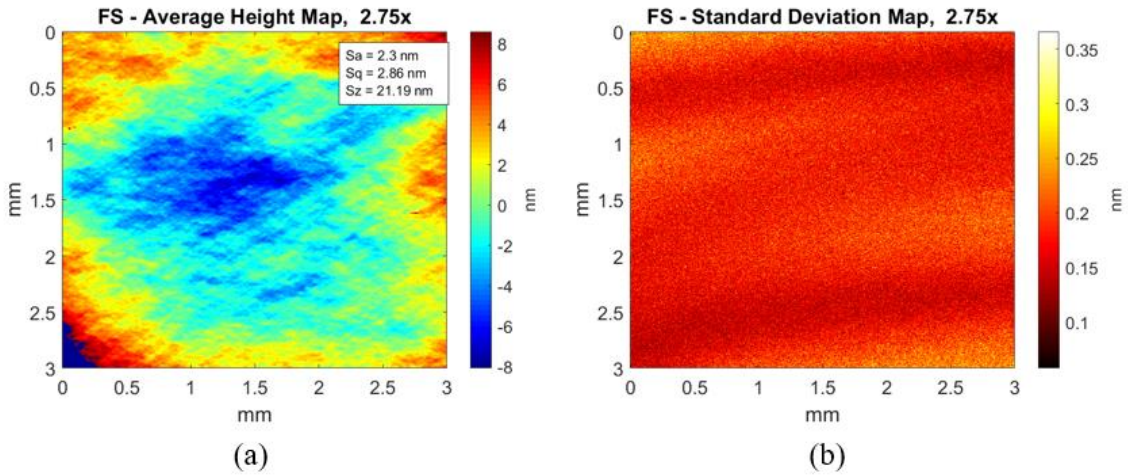

FIGURE 8: Run 1 using 2.75x objective, FS (a) average height map and (b) standard deviation map

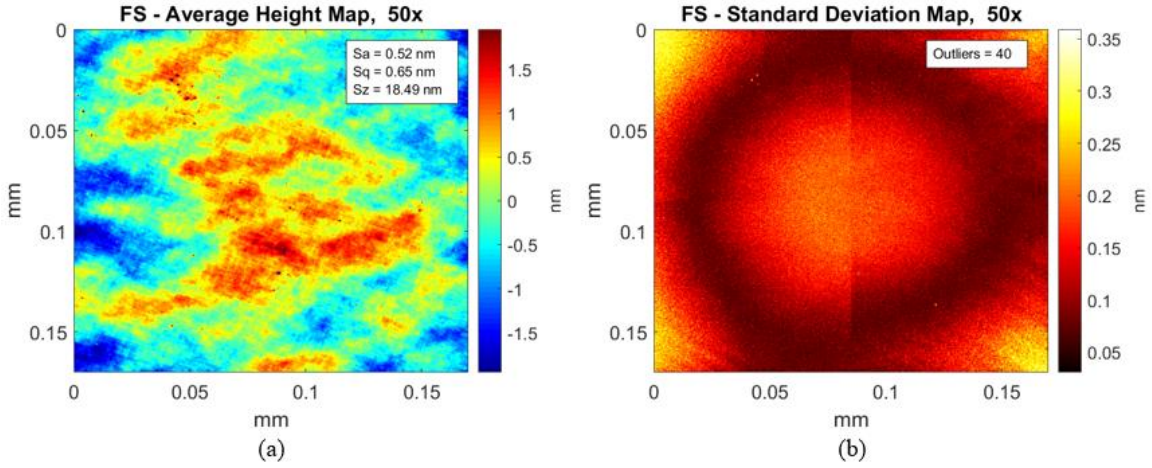

FIGURE 9: Run 1 using 50x objective, FS (a) average height map and (b) standard deviation map truncated at 70th percentile for visualization purposes

The circular pattern for the 50x (FIGURE 9 (b)) suggests a change in a quadratic term [38] in the reference, the part, the index of air, or a thermally induced change in the reference leg. Assuming a monotonic variation, the sag from the “circular fringe” in FIGURE 9 (b) is ~0.3 nm (where sag is approximately 5x standard deviation), which

implies a corresponding 1.6 m change in ROC. There are two other aspects of this 50x standard deviation map that deserve comment: 1) both bottom corners of the map reveal what appears to be residual polishing marks and 2) there is a discontinuity at the middle of the field that shows an imbalance of the quad-taps on the charge-coupled device (CCD) sensor [61] affecting signal to noise. Both aspects demonstrate the standard deviation map's superb sensitivity to explain the physics of the manufacturing process and environmental effects where no effect is visible in the height map.

At times, the standard deviation maps may have a number of outliers listed, which is computed in MATLAB by truncating at a certain percentile for visualization purposes when the image is too dark or for comparing with similar color bar ranges. For both FIGURE 9 (b) and FIGURE 10 (b) , the standard deviation maps were truncated at the 70^{th} percentile where respectively 40 and 68 outliers were removed. FIGURE 10 shows a more visible surface of the standard deviation map for the FS after truncation. A low mean STR value and the visual map indicate that this measurement was made with a smooth surface that had no vibration effects.

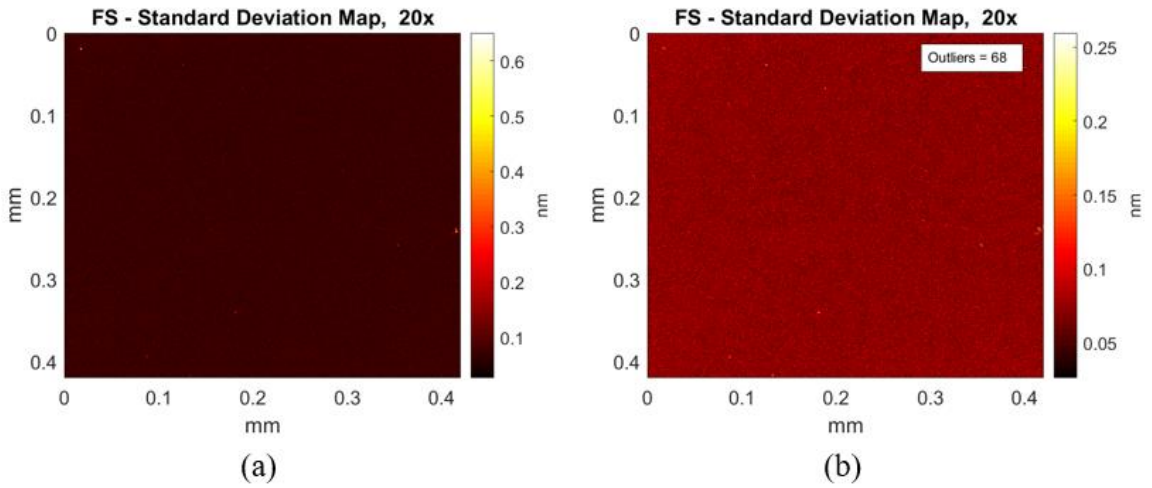

FIGURE 10: Run 1 using 20x, FS standard deviation map (a) before and (b) after outliers are removed, truncated at 70th percentile for visualization purposes

The third run for the FS demonstrated repeatability across all three objectives and methods in TABLE 5. It was observed that timing of when the measurements were taken may also yield different results. For instance, run 3 was done between 4:47 – 5:03 pm when there was less traffic in the building (four classes in session) whereas run 1 was spread throughout the day (3:15 – 6:45 pm) where change of classes increases the foot traffic and the use of the elevator in the building. All three FS standard deviation maps for each objective show a smooth surface with similar color bar ranges with no truncation.

TABLE 5: Run 3, FS STR values for each objective

	2.75x	**20x**	**50x**
Subtraction Method	0.14 nm	0.13 nm	0.14 nm
Synthetic Reference	0.14 nm	0.13 nm	0.14 nm
Standard Deviation Map	0.14 nm	0.14 nm	0.14 nm

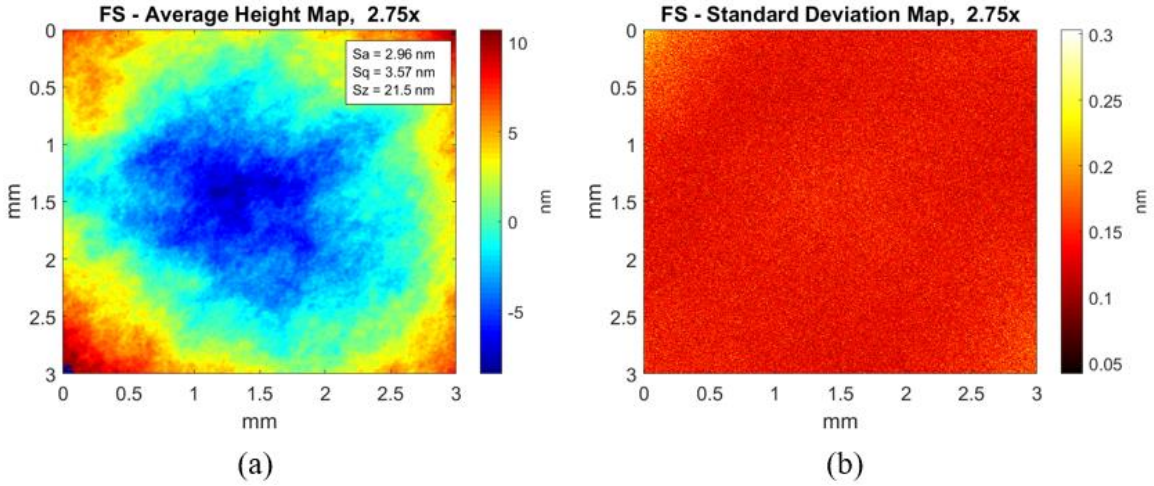

FIGURE 11: Run 3 using 2.75x objective, FS (a) average height map and (b) standard deviation map

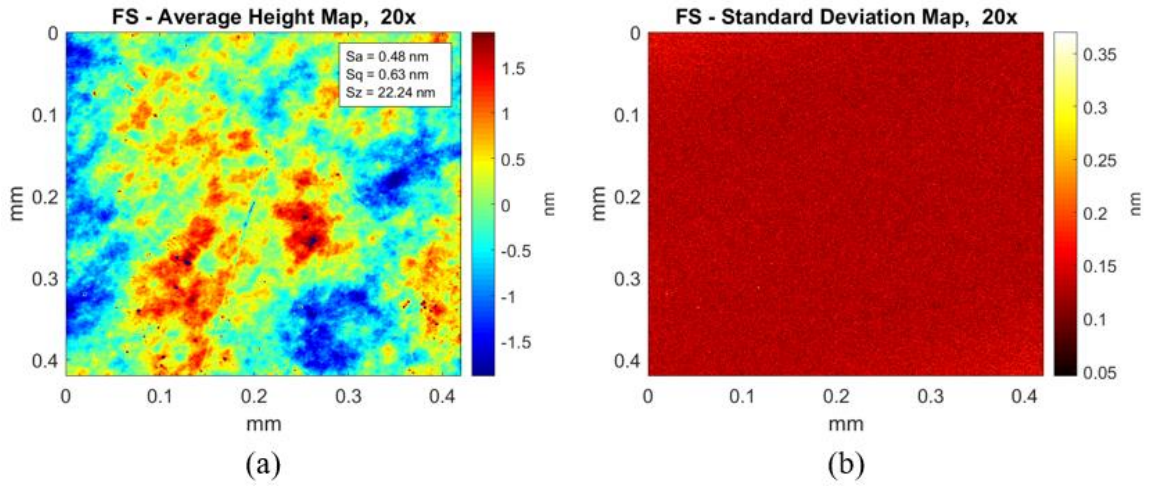

FIGURE 12: Run 3 using 20x, FS (a) average height map and (b) standard deviation map

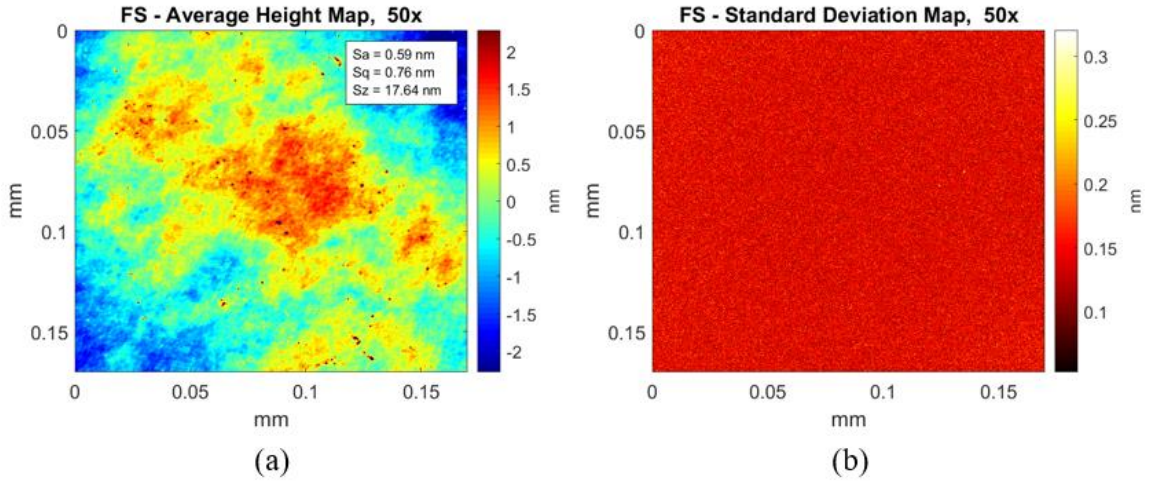

FIGURE 13: Run 3 using 50x, FS (a) average height map and (b)standard deviation map

The fifth run of measurements consisted of measuring the Silicon Carbide (SiC) flat of the type typically provided for calibration of SWLIs in general. These measurements reported here were taken after hours between 7:06 – 7:26 pm on March 18, 2020, the night before the shutdown for Covid 19, which was an ideal time to conduct measurements since the building was nearly empty. Like run 3 for the FS, run 5 for SiC

also exhibited repeatable STR across all methods and objectives (TABLE 6) and matched the STR specification [7].

TABLE 6: Run 5, SiC STR values for each objective

	2.75x	**20x**	**50x**
Subtraction Method	0.10 nm	0.10 nm	0.10 nm
Synthetic Reference	0.10 nm	0.10 nm	0.10 nm
Standard Deviation Map	0.10 nm	0.10 nm	0.10 nm

The average height and standard deviation maps for all three objectives also show smooth, highly polished surfaces. The 2.75x and 50x were truncated at 55^{th} and 65^{th} percentiles respectively so that the surfaces could be visible with similar standard deviation ranges. Running the 20 measurements for the 2.75x and 20x through the Mx software produces some intensity maps with a single fringe where both FIGURE 14 (b) and FIGURE 15 (b) have two times the fringe frequency, suggesting minor vibration.

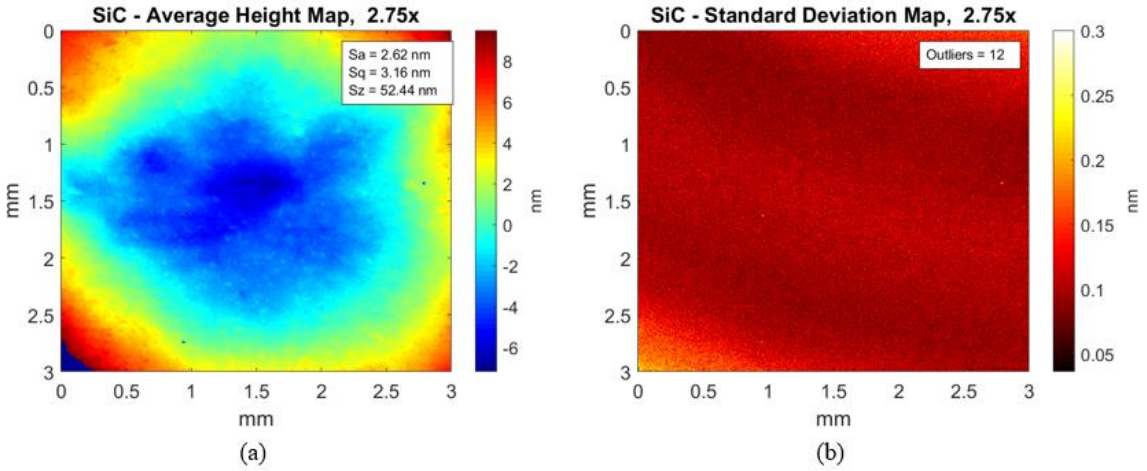

FIGURE 14: Run 5 using 2.75x, SiC (a) average height map and (b) standard deviation map truncated at 55th percentile for visualization purposes

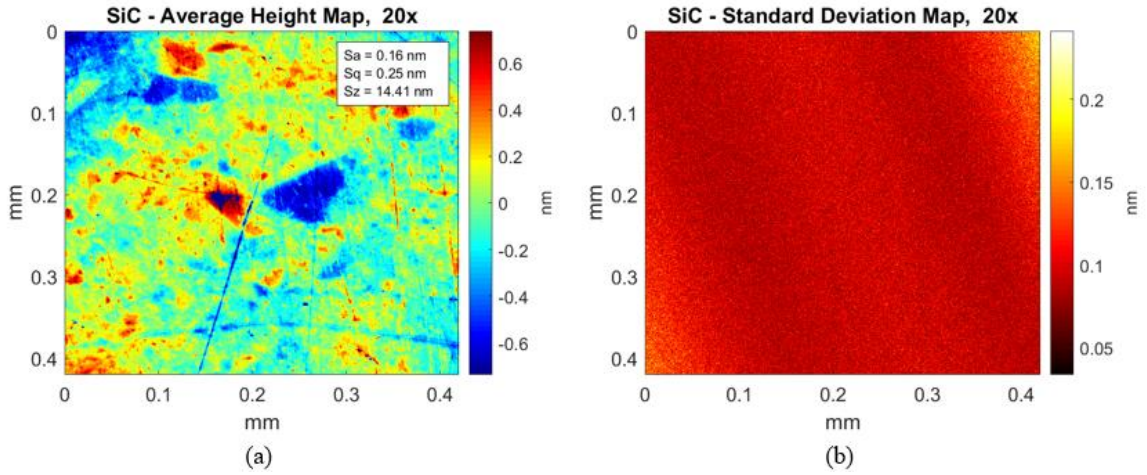

FIGURE 15: Run 5 using 20x, SiC (a) average height map and (b) standard deviation map with no truncation

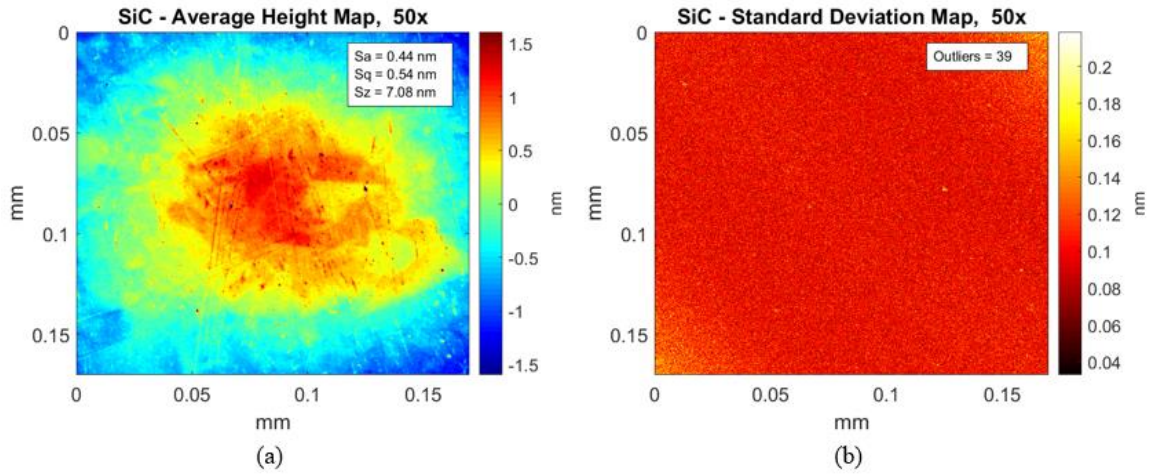

FIGURE 16: Run 5 using 50x, SiC (a) average height map and (b) standard deviation map truncated at 65th percentile for visualization purposes

NiP diamond turned at 10, 20 and 30 µm/rev (with a 0.4 mm nose radius tool) were also analyzed how surface roughness affected the STR value. The DT surfaces at all three feed rates and objectives were also part of run 5 measurements, which was around the same time as the SiC flat. These measurements of the DT surface were taken after hours between 5:47 – 7:00 pm on March 18, 2020, the night before the shutdown for Covid 19, which again, was an ideal time to conduct measurements since the building was nearly empty.

TABLE 7: Run 5, NiP 10 µm/rev STR values for all objectives

	2.75x	20x	50x
Subtraction Method	0.1 nm	0.1 nm	0.1 nm
Synthetic Reference	0.1 nm	0.1 nm	0.1 nm
Standard Deviation Map	0.1 nm	0.1 nm	0.1 nm

The NiP DT at 10 µm/rev measurements all show repeatability as seen in TABLE 7. Note, however, that the 2.75x objective (with 1x tube lens) gives three pixels per feed (cusp) for the 10 µm/rev, close to Nyquist where the ITF is expected to be low. The average height map in FIGURE 17 (a) shows some MSF content at approximately 1 mm period. There is a similar period in the standard deviation map. The curvature of the 1 mm level variation in the standard map differs from the curvature in the feed marks.

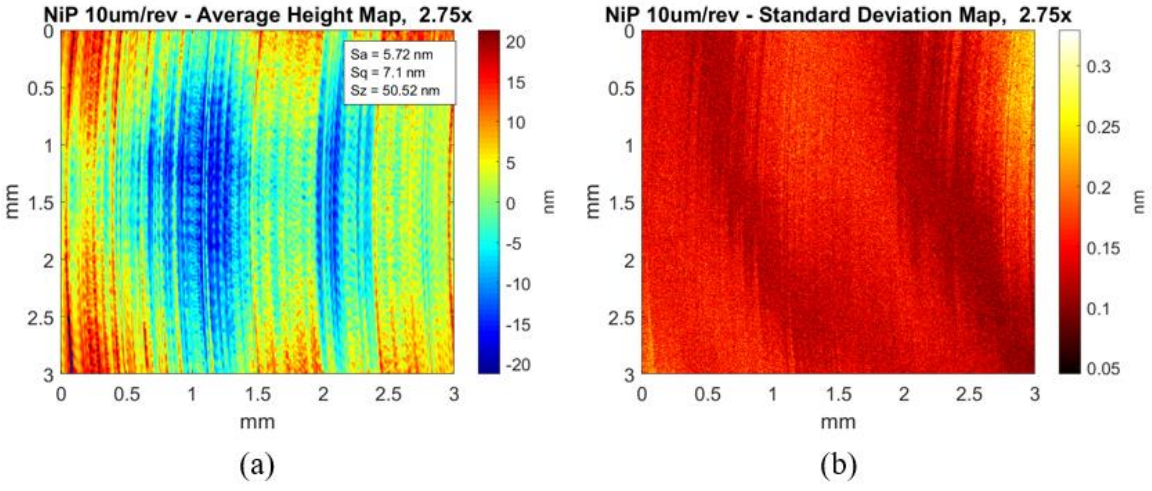

FIGURE 17: Run 5 using 2.75x, NiP DT at 10 µm/rev (a) average height map and (b) standard deviation map before filtering cone

From other measurements, we know that part has “cone” error (presumably arising from squareness errors uncorrected at the time this part was made). Close to Nyquist, this may affect signal to noise and hence variation in measured height over the 20 measurements reported here.

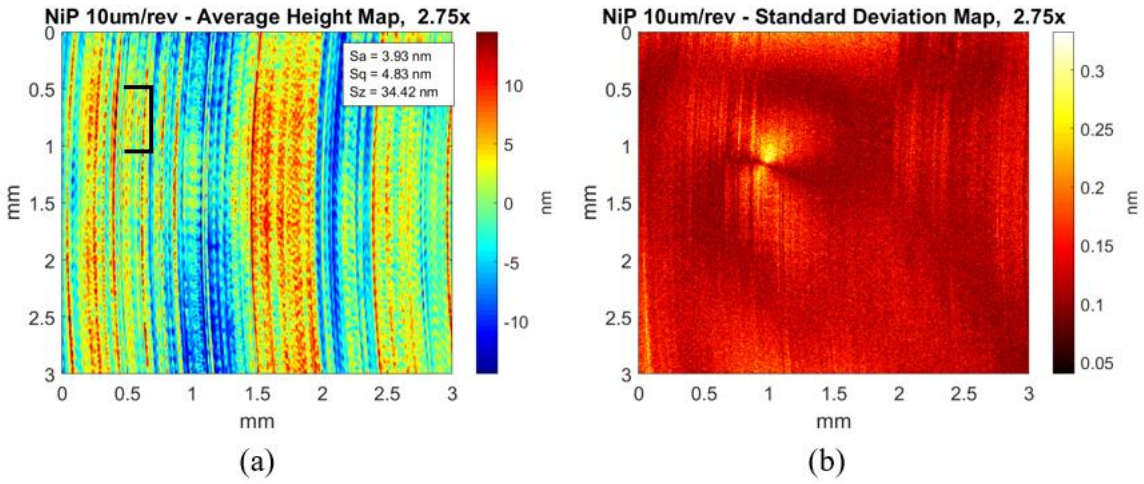

FIGURE 18: Run 5 using 2.75x, NiP DT at 10 µm/rev (a) average height map and (b) standard deviation map after further filtering cone

Cone was filtered from the measurements in Mx and then run through STR code filtering piston and tilt (FIGURE 18), now revealing lower amplitudes, MSFs and that Nyquist is indeed affecting the signal to noise (FIGURE 19). In the top left corner in the yellow patch, there is a dark (i.e. low standard deviation) swirl–pattern probably from turbulence where the length of it is pointed out in FIGURE 18 (a) with a bracket. After filtering cone, ghosts of DT marks and a bright spot (higher standard deviation) became visible in the standard deviation map (FIGURE 18 (b)). The mechanism for forming this bright spot has not yet been determined. Further analysis of the bright spot and models of other DT surfaces have not been considered in Sections 2.4 and 2.5, and should be in future work.

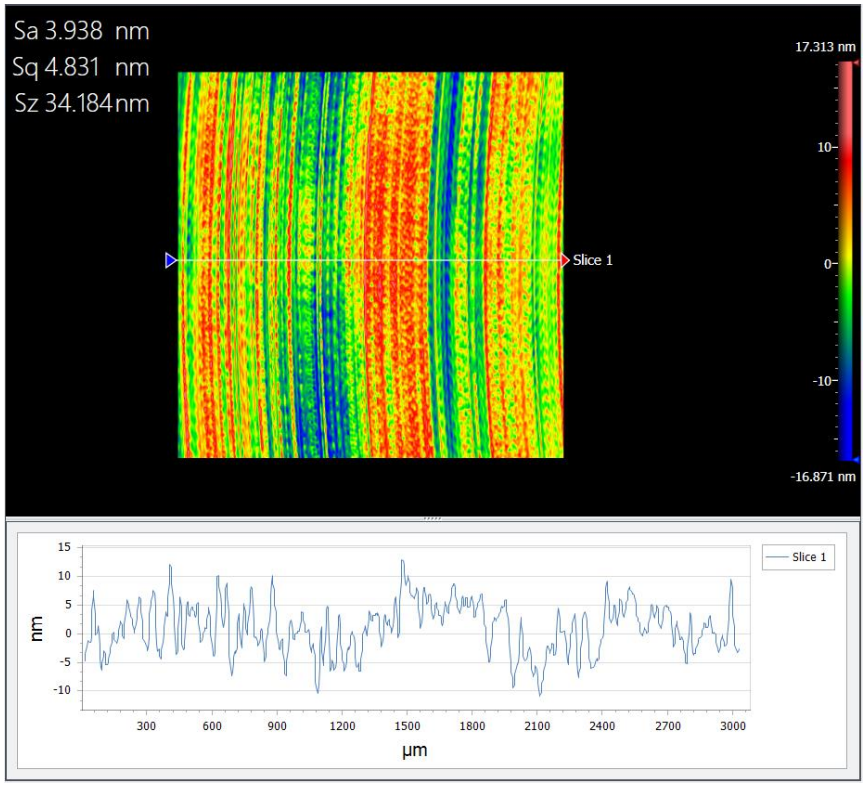

FIGURE 19: DT surface after filtering cone with slice illustrating how resolution of the cusp marks deteriorate approaching Nyquist with the 2.75x

The 20x and 50x measurements of the 10 µm/rev contain no surprises (FIGURE 20 and FIGURE 21) since the individual cusps are easily resolved. Height variations with 50 – 100 µm periods are apparent in both the 20x and 50x standard deviation map.

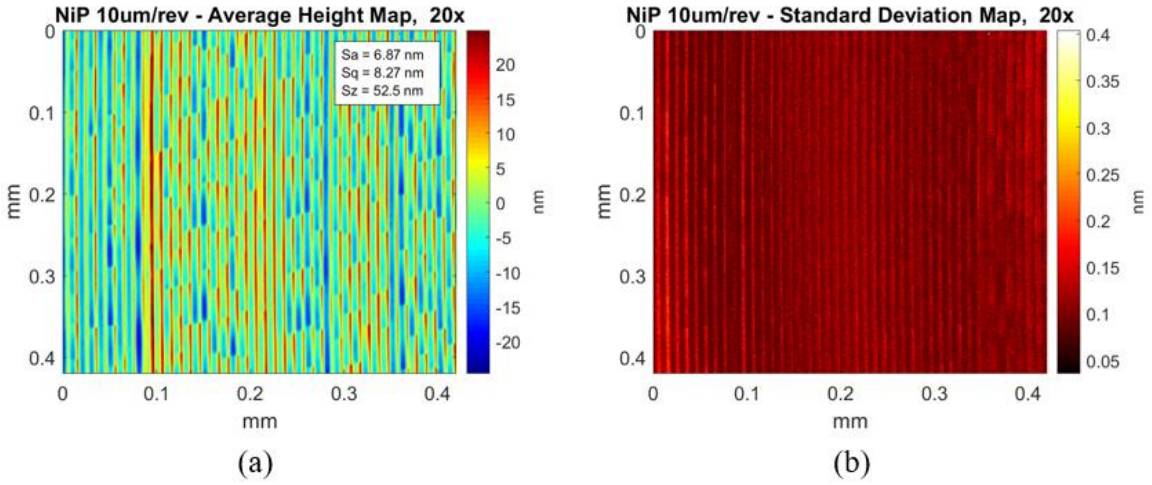

FIGURE 20: Run 5 using 20x, NiP DT at 10 µm/rev (a) average height map and (b) standard deviation map

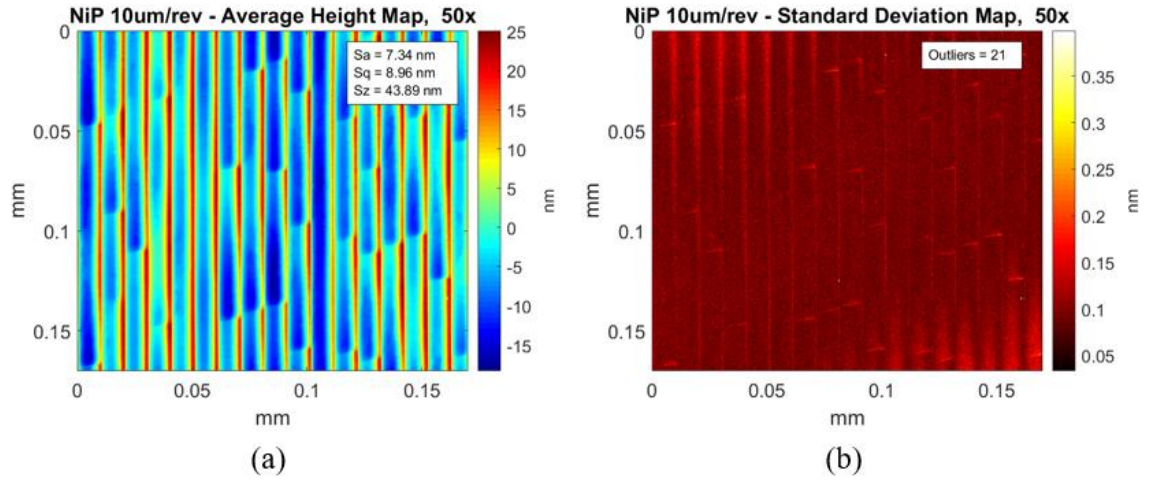

FIGURE 21: Run 5 using 50x, NiP DT at 10 µm/rev (a) average height map and (b) standard deviation map truncated at 61st percentile for visualization purposes

The 20 µm/rev STR value differences in TABLE 8 are within rounding error for the three methods. Values for all three methods are higher than the values for the smooth isotropic surfaces, such as the SiC flat and FS, but give no indication of the root cause.

TABLE 8: Run 5, NiP 20 µm/rev STR values for all objectives

	2.75x Cone filter	**20x**	**50x**
Subtraction Method	0.2 nm	0.3 nm	0.3 nm
Synthetic Reference	0.2 nm	0.2 nm	0.2 nm
Standard Deviation Map	0.2 nm	0.3 nm	0.3 nm

The 2.75x data for the 20 µm/rev sample suggests similar issues as the 10 µm/rev sample, but at a higher amplitude (FIGURE 22 (a)). Like 10 µm/rev 2.75x, cone was filtered with the 20 µm/rev and the standard deviation map was truncated so the map could be seen in FIGURE 22 (b). The average height map still exhibited a wave pattern on top of the DT marks, which may suggest chatter. In the standard deviation map, height variations of the DT marks are visible with the same wave pattern. Further investigations into what is causing this wave could be considered for future work.

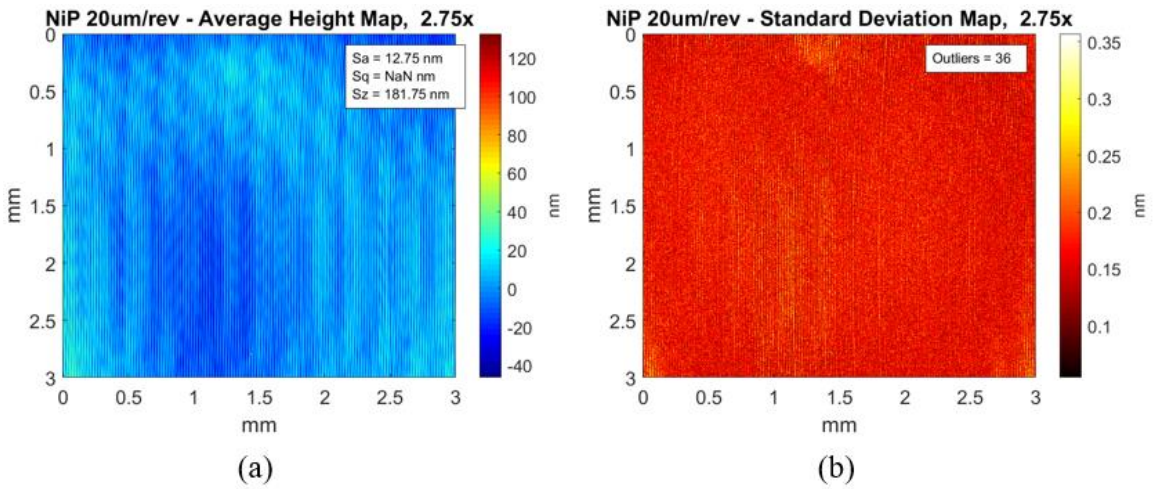

FIGURE 22: Run 5 using 2.75x, NiP DT at 20 µm/rev (a) average height map and (b) standard deviation map truncated at 50th percentile for visualization purposes after further filtering cone

The 20x (FIGURE 23) standard deviation map showed the ghost of the DT cusp mark surface well where another initial run of the same feed rate prompted further analysis on the stage motions of the NexView (See Section 2.4 and 2.5).

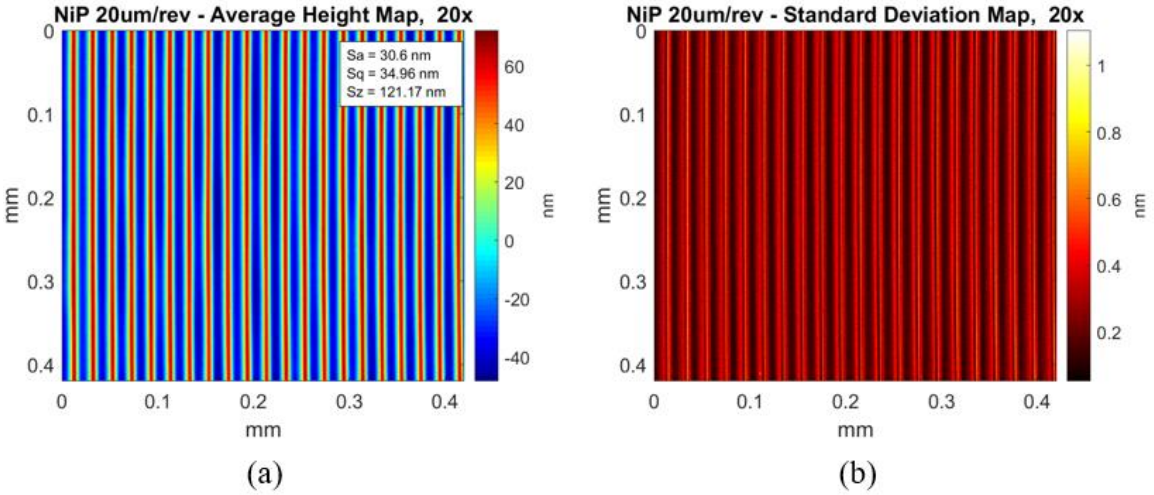

FIGURE 23: Run 5 using 20x, NiP DT at 20 µm/rev (a) average height map and (b) standard deviation map

Like the 20x for the 20 µm/rev, the 50x was similar in showing the ghost of the DT cusp marks after it was truncated at 59th percentile.

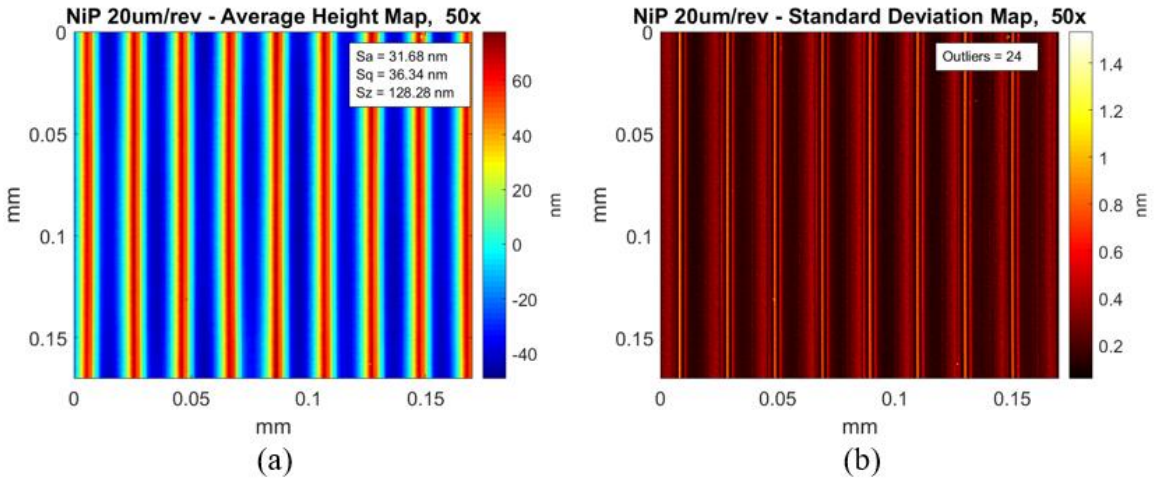

FIGURE 24: Run 5 using 50x, NiP DT at 20 µm/rev (a) average height map and (b) standard deviation map truncated at 59th percentile for visualization purposes

The 30 µm/rev STR values in TABLE 9 did not show repeatability as did the 10 and 20 µm/rev STR values. Results for the 2.75x and 20x measurements were anomalous even after further filtering was performed with 2.75x data. The STR values were initially higher for the 2.75x for all three methods (6.8, 6.6 and 2.7 nm respectively).

TABLE 9: Run 5, NiP 30 µm/rev STR values for all objectives

	2.75x FFT	**20x**	**50x**
Subtraction Method	1.6 nm	1.2 nm	0.2 nm
Synthetic Reference	1.5 nm	0.2 nm	0.1 nm
Standard Deviation Map	1.3 nm	1.2 nm	0.2 nm

Before filtering (besides piston and tilt), the average height map and standard deviation map were showing a Moiré pattern as seen in FIGURE 25.

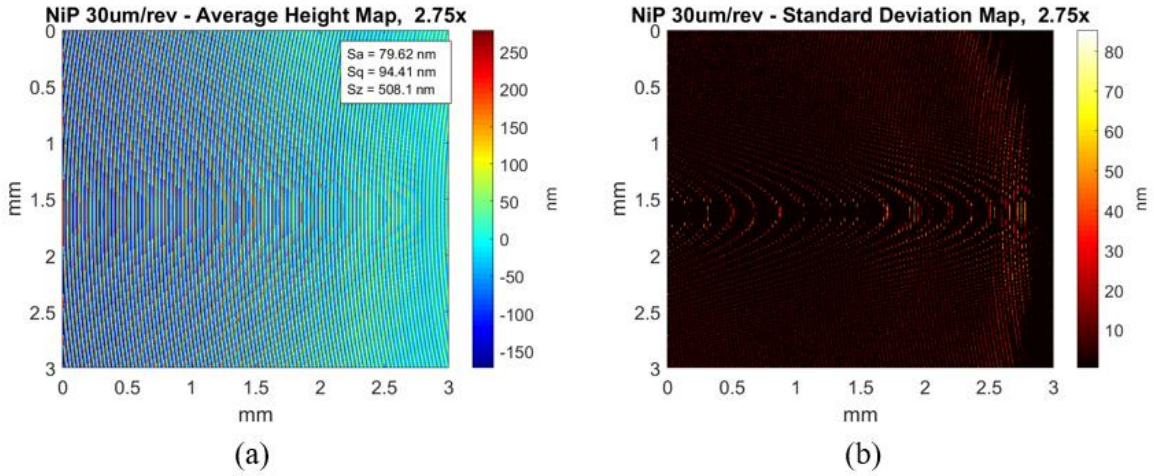

FIGURE 25: Run 5 using 2.75x, NiP DT at 30 µm/rev (a) average height map and (b) standard deviation map before additional filtering

A Fast Fourier Transform (FFT) low pass filter with a 60 µm cutoff (based on the period) was performed on the 30 µm/rev measurements with the 2.75x in FIGURE 26. Now the MSFs are visible, but the wave could not be filtered out, which suggests a

diffraction effect. Another set of measurements with the 2.75x should be considered in the future work to determine whether these STR values and maps were anomalies.

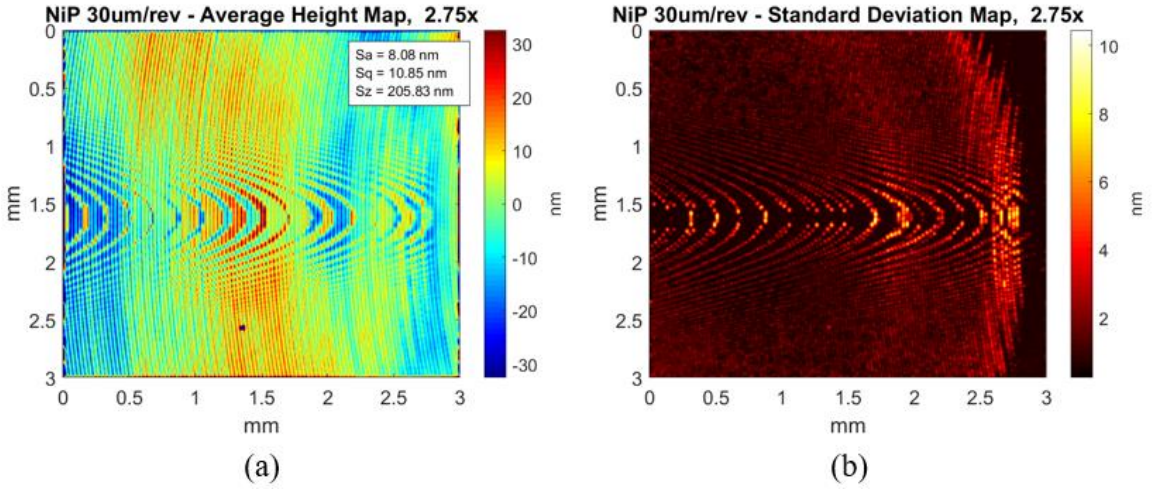

FIGURE 26: Run 5 using 2.75x, NiP DT at 30 µm/rev (a) average height map and (b) standard deviation map after an FFT low pass filter was applied

The 20x 30 µm/rev height map and standard deviation map (FIGURE 27) did not show any visible differences but a higher amplitude than the 20x 20 µm/rev maps (FIGURE 23).

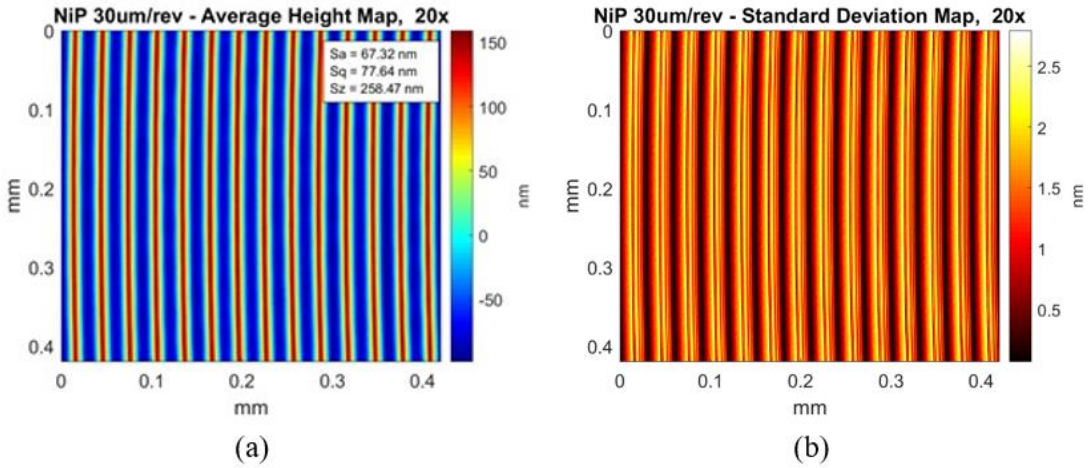

FIGURE 27: Run 5 using 20x objective, NiP DT at 30 µm/rev (a) average height map and (b) standard deviation map

Run 1 of the 20x 20 µm/rev was performed on 5/2/19 at 10:43 – 10:45 am (FIGURE 33) with STR values of all three methods in TABLE 10. This first run demonstrated repeatability opposed to Run 5 among the STR methods.

TABLE 10: Run 1, NiP DT 20 µm/rev STR values

	20x
Subtraction Method	0.3 nm
Synthetic Reference	0.3 nm
Standard Deviation Map	0.2 nm

The 50x 30 µm/rev STR values (TABLE 9) were repeatable among the three methods and again, the standard deviation map (FIGURE 28 (b)) showed the diamond turned marks at a much lower amplitude.

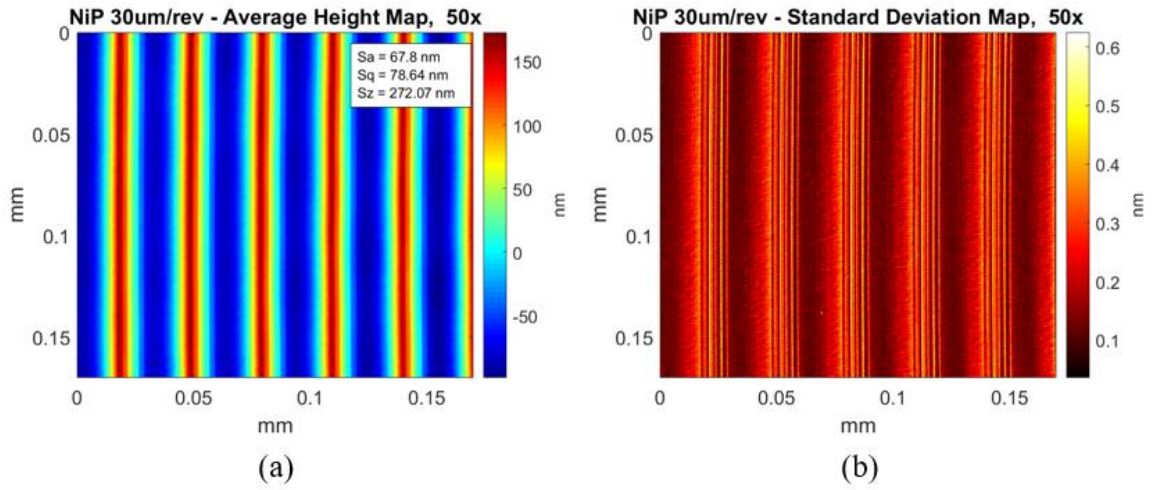

FIGURE 28: Run 5 using 50x, NiP DT at 30 µm/rev (a) average height map and (b) standard deviation map

All three methods, objectives and DT feed rates were observed where the 10 and 20 µm/rev NiP STR values were repeatable, but the results for the 30 µm/rev NiP for the 2.75x were anomalous. Although the 30 µm/rev 20x results were inconsistent across the three methods in run 5, run 1 suggests it as an anomaly.

2.3.4 Relationships between STR and other surface parameter specifications

STR values as a function of each surface parameter such as, surface roughness (Sa), RMS, peak-to-valley (Sq), Skewness (Ssk) and Kurtosis (Sku) were all evaluated with respect to objectives and surface types, but no clear correlation could be found. The Power Spectral Density (PSD), like many surface parameters, has its roots in signal processing (see for example Whitehouse, D.J., PhD thesis 1974) [62]. The PSD function was initially used to evaluate surface roughness and waviness [63], [64], where Church et al also compared the measurements with two different instruments [64]. Several years later, Church and Takacs demonstrated that light scattering from artifacts in the surface are a function of the PSD [65]. Elson and Bennett pointed out two smoothing methods to

reduce the variance bringing attention to problematic areas of a one-dimensional PSD [66]. As a driver towards ISO standardization, Herman et al explains the transition from other standards that optical fabricators and designers used to a single standard, ISO 10110-8 [39], [67]. Recently, Aryan et al illustrate how anisotropic DT surfaces at different feed rates can all fall under same specifications according to ISO 10110-8, but have different optical performance [39], [68].

In this work, the PSD was analyzed for an entire surface and a profile in the x-direction for each objective and surface. The PSDs, computed in Mx software, were exported to MATLAB (Appendix C). A profile PSD on an anisotropic surface is direction dependent, therefore, a slice was placed in the x-direction, which was orthogonal to the dominant lay of the DT surface. The SiC and FS surfaces are smooth and isotropic.

An average-x PSD for an entire surface improves the signal-to-noise [69] and smooths out the data, even for a DT surface with a feed rate of 30 μm/rev (FIGURE 29). The surface average-x PSDs indeed turned out to be smoother than the profile PSDs.

The cusp structure of the DT surface is not well fit by a single Fourier component at the feed rate. As shown in FIGURE 29, they are components at the fundamental (i.e. feed rate – 30 μm/rev or 33 cycles/mm) and higher harmonics, as shown consistently for all three objectives. A list of induced MSFs [70], includes the stepover from a diamond tool. The periodicity from the 30 μm/rev falls well below the default roughness cut-off of 80 μm in ISO 10110-8 [39]. All three objectives roll off to Nyquist (refer to TABLE 3).

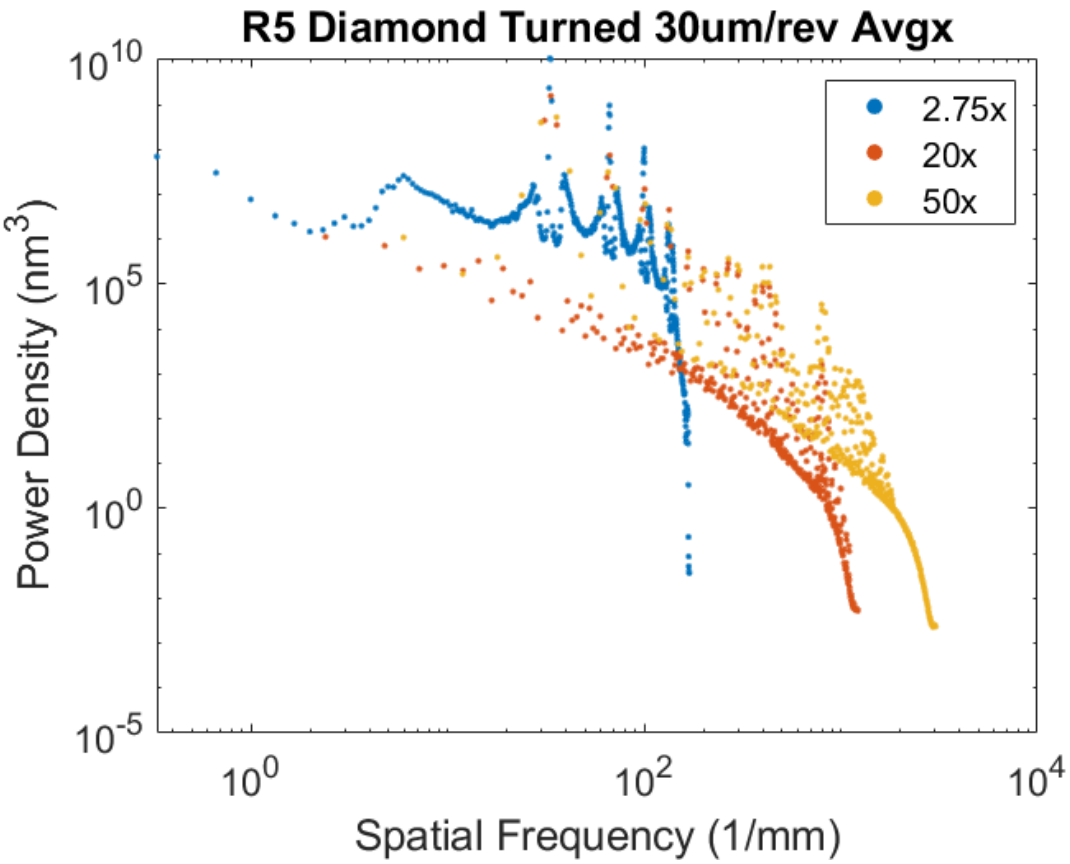

FIGURE 29: PSD for each objective for run 5, DT 30 µm/rev surface

The PSDs for FS and SiC produced smoother curves (FIGURE 30 and FIGURE 31), which is expected for an isotropic surface with a single-digit-nm to sub-nm surface roughness. Both figures clearly show the roll off in the PSD as spatial frequencies approach Nyquist.

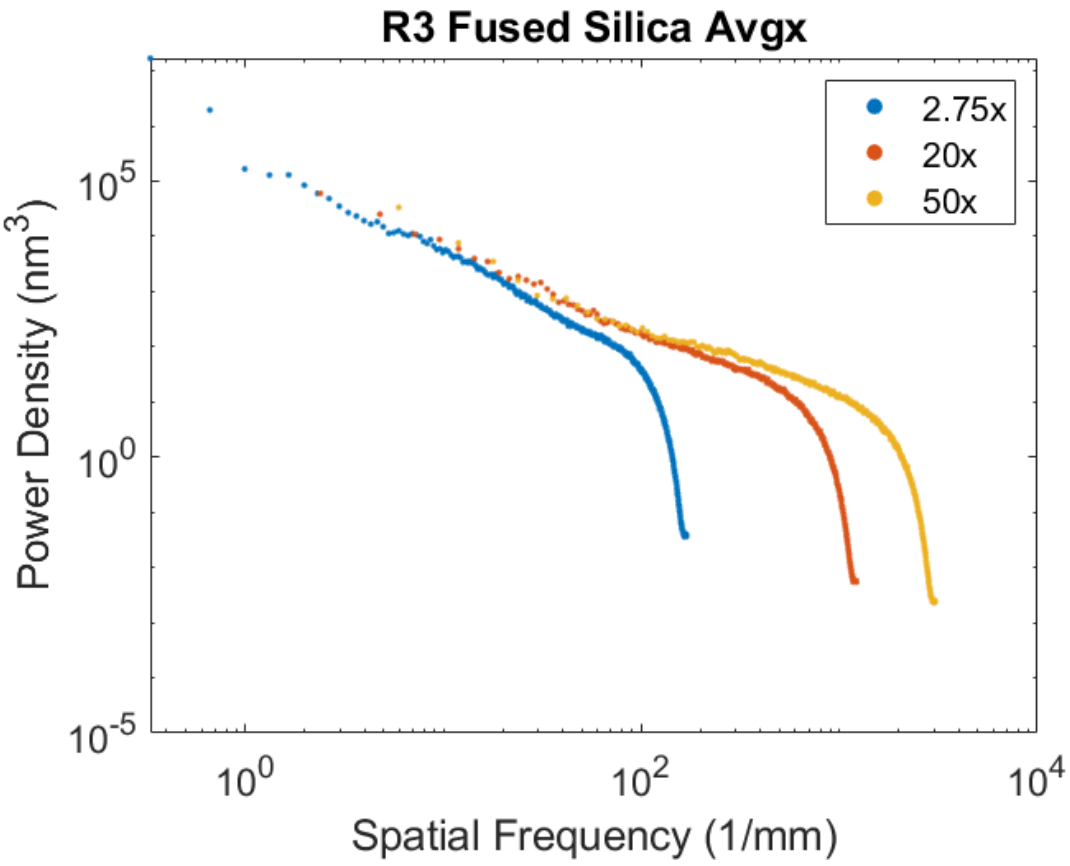

FIGURE 30: PSD for each objective for run 3, FS surface

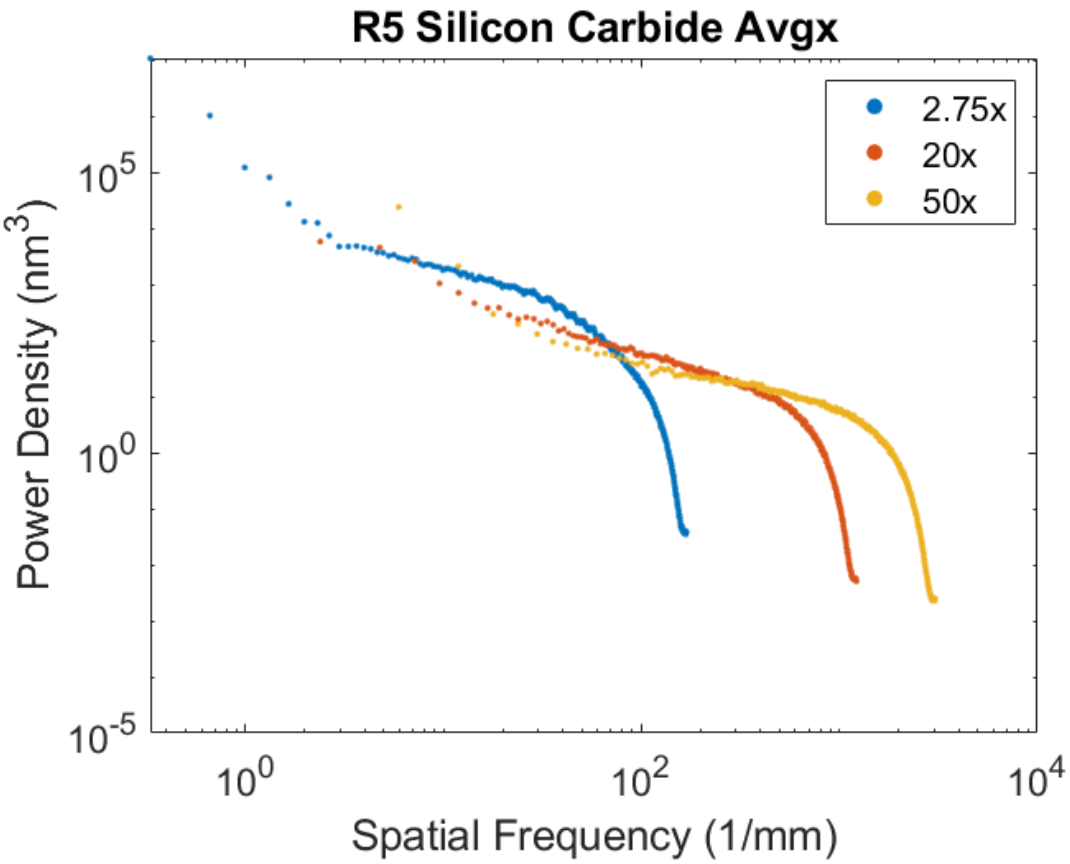

FIGURE 31: PSD for each objective for run 5, SiC flat surface

For the 20x and 50x objectives, apart from the difference in high frequency roll off, the PSDs show bandwidth limited PSD = A/f^B characteristic[4] [39] expected from such a surface, and used in ISO 10110-8 as the basis for a limit line specification.

Over the spatial frequency range of 10-1000 cycles/mm, the power density drops from approximately 2000 to 5 nm^3 in FIGURE 31. The 2.75x objective shows a similar "linear" region, albeit at a slightly higher power and a distinct slope change at low spatial frequencies. Both effects may be a result of the low order form error (FIGURE 14 (a)).

[4] Where A is a constant, f is spatial frequency of roughness or waviness in mm^{-1}, and B is greater than zero and typically $1 < B < 3$ for many real surfaces

PSDs of the 30 µm/rev DT NiP (FIGURE 32) are significantly different than those of SiC. First, over the 10-1000 cycles/mm range, the power density range is approximately 5.6e6 to 1200 nm^3 as seen in FIGURE 29. Measurements made using the 50x objective show wear in the leading edge of the tool leaving a ripple with a mean period of ~10 µm (FIGURE 29). The surface variation at the longer wavelengths (including components traditionally considered "finish" and MSFs give increased scatter. MSFs produce a phenomena called "small-angle scatter", which broadens the point spread function (PSF) and decreases the resolution of the optical system [71].

The STR values for the NiP DT at 10 µm/rev were all 0.1 nm, similar to that for the isotropic SiC and FS which have approximately an order of magnitude lower rms roughness. PSDs of the SiC or FS are smoother than the 10 µm/rev DT NiP (FIGURE 32). Over the 10-1000 cycles/mm range, the power density range is approximately 200,000 to 1000 nm^3 as shown in FIGURE 32.

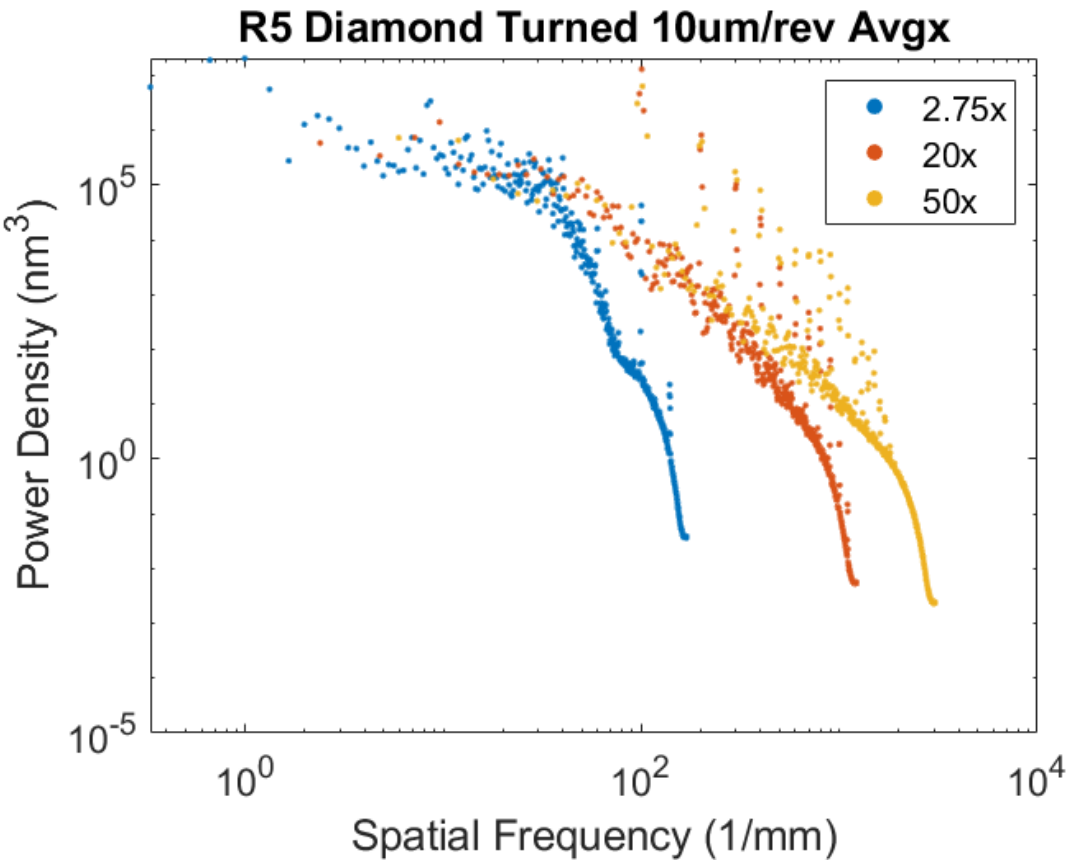

FIGURE 32: PSD for each objective for DT 10 µm/rev surface

Although it is not required by the ISO standards to state the surface type, it is ideal for manufacturers to measure super polished surfaces if their goal is to quantify the noise floor of their instrument under ideal circumstances. The results from different smooth surfaces demonstrates that STR values can be similar, but when they are different, the question is why? In the absence of a temporal effect, why should STR values differ systematically for different surfaces measured on the same instrument by the same operator in the same (good) environment? Since STR is simply a numerical value, including a standard deviation map may be more insightful as to why, as previous

examples of the standard deviation maps exhibited vibration, drift or turbulence occurring during the measurement.

2.3.5 STR measurements that led to evaluating stage motion errors on the Zygo NexView

Initial run 1 for the STR experiments consisted of NiP DT at 20 µm/rev, FS and SiC optics. The DT surface was apparent in the standard deviation map resembling the average height map (FIGURE 33) at a much lower amplitude with additional harmonics at each "cusp". This anisotropic surface produced an anisotropic standard deviation map, while isotropic surfaces (FIGURES 8 – 16) produced essentially isotropic standard deviation maps. This observation led to investigating the motion errors through other metrology methods.

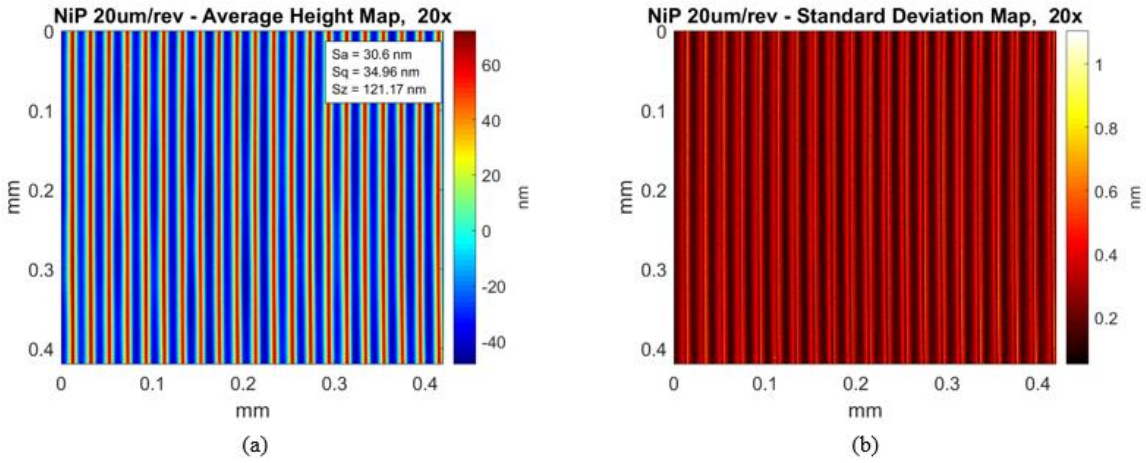

FIGURE 33: Run 1 using 20x objective, NiP DT at 20 µm/rev (a) average height map and (b) standard deviation map

2.4 Setup and use of Displacement measuring interferometry (DMI) to measure stage motion

The DT marks in the standard deviation map prompted questions on whether the NexView stage was imperceptibly moving to produce a "shadow effect" in the standard

deviation map. Hence, x- and y-carriage static stability tests were conducted using displacement measuring interferometry (DMI), a high-precision metrology method for stage positioning, among many applications [38], [72], [73]. The DMI setup shown in FIGURE 34 consists of the Agilent 5519a 633 nm Helium Neon (HeNe) laser, inherently traceable to the unit of length [72], a beam splitter and retroreflector (RR) connected to the stand that was glued to the instrument's frame and another RR mounted on the stage.

FIGURE 34: DMI set up on the NexView stage

The laser beam emerges from the laser head and gets split at the BS where one beam gets reflected traveling to the reference RR and the second gets transmitted to the measurement RR. Both beams get reflected back from the RRs recombining and causing interference where the difference in path length of the two beams is evaluated by the change in phase. Through signal processing, extracting the phase will yield a measurement of displacement. Using the Agilent Technologies software to collect the data and having sub-micron resolution, the x- and y- carriage's positions were measured separately. A sampling frequency of 1 KHz over a period of 10 s was taken since it takes approximately 4 seconds to acquire an image with the SWLI. The results in FIGURE 35 showed that the x-carriage moved between 50 – 70 nm PV and the y-carriage with a larger range of 30 – 80 nm.

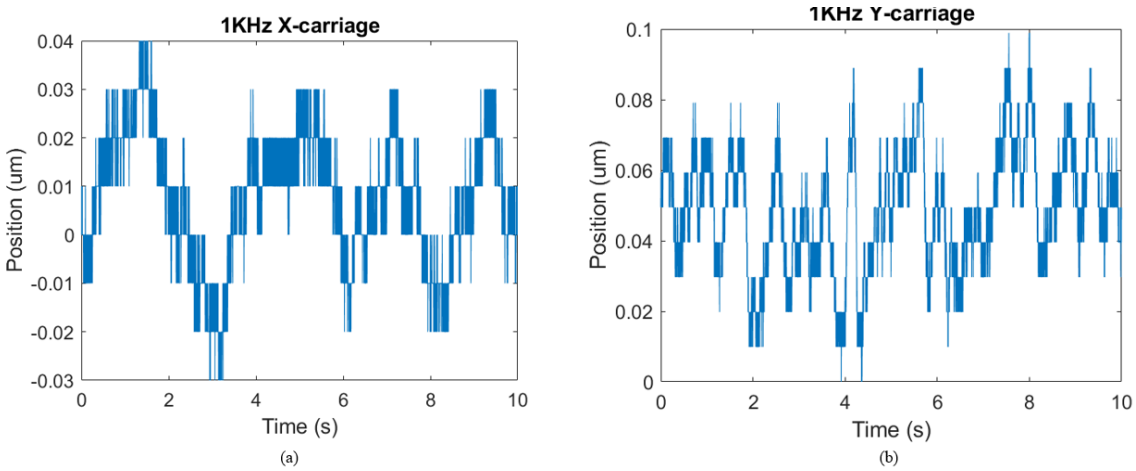

FIGURE 35: DMI results of the (a) x- and (b) y-carriage movement

The dead path (FIGURE 34) was approximately 100 mm and air temperature control specification is ±0.1C, although recent measurements adjacent to the NexView have

shown stability over longer periods to ±0.04C. Measurement uncertainty associated with refractive index changes in air are an order of 10 nm.

Simultaneous dual axis motion measurement of the x-y stage is possible through, for example, plane-mirror interferometry [72] or simply using two Michelson interferometers. The required hardware was not available at the time these measurements were made.

2.5 Emulating the stage motion errors via Monte Carlo Simulation in MATLAB

Since the DMI experiment resulted in the stage position moving approximately 50 - 70 nm in the x-carriage, a Monte Carlo simulation (MCS) was computed with an extracted profile of the cusp structure from the DT surface interferogram, randomly shifted. A profile was analyzed instead of an entire surface to test quickly. Since the surface has minimal variation along the lay, this simplification seemed appropriate. The profile was interpolated, randomly shifted using rectangular distribution and then decimated in MATLAB to compare to the same profile that was extracted after the STR standard deviation map was computed. Increasing the shift amount increased the amplitude of the data; the 60 nm MCS profile most closely matched the amplitude of the standard deviation map after calculating STR in FIGURE 36. Although there is a shift in the STR standard deviation map profile, PV for both profiles is roughly 1 nm.

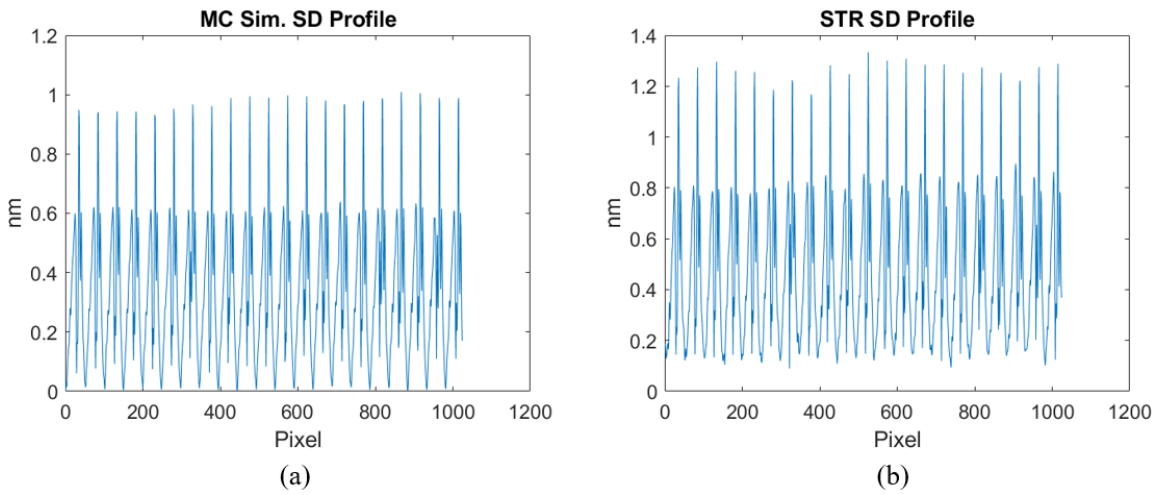

FIGURE 36: Profiles from the (a) MCS with a 60 nm shift vs (b) standard deviation map after calculating STR

To get a closer look of the profile's shape, both were zoomed in on the first 200 pixels (~84 µm). The MCS standard deviation profile exhibited a very similar distorted cusp structure to the STR standard deviation profile with the same magnitude, which suggests that the stage was moving approximately 60 nm when the measurements were being taken.

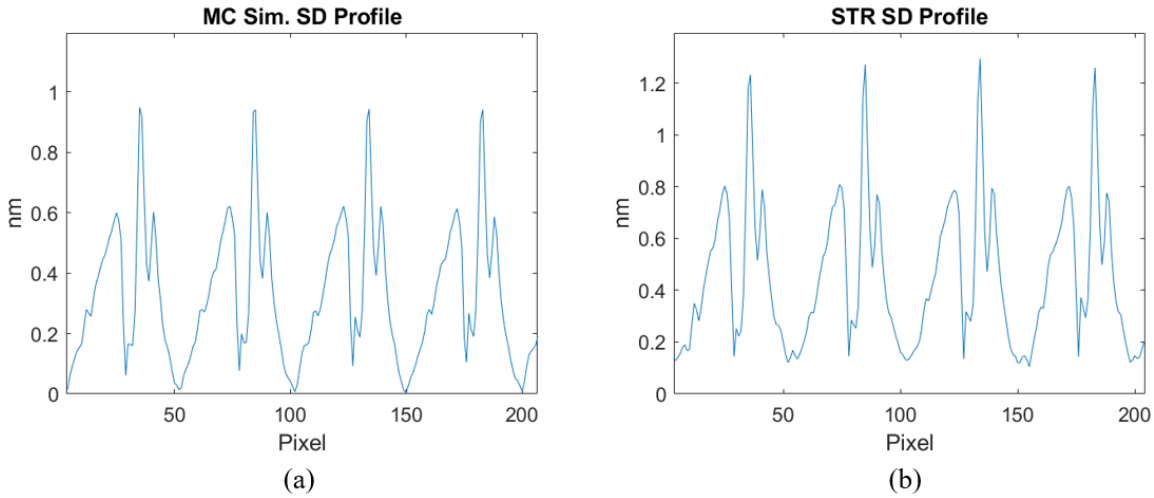

FIGURE 37: Zoomed in profiles from the (a) MCS with a 60 nm shift vs (b) standard deviation map after calculating STR

2.6 Setup of the dual-axis motion errors of the NexView stage via capacitance probe testing

The setup in FIGURE 38 and FIGURE 39 consisted of the Lion Precision CPL 290 modules, NI USB-6251 16-bit data acquisition (DAQ), two Lion capacitive displacement sensors with a 500 µm range, housing to hold the sensors, laptop with LabVIEW program (Appendix E) and a machined aluminum rectangular bar used as an extension of the NexView stage to be measured easily.

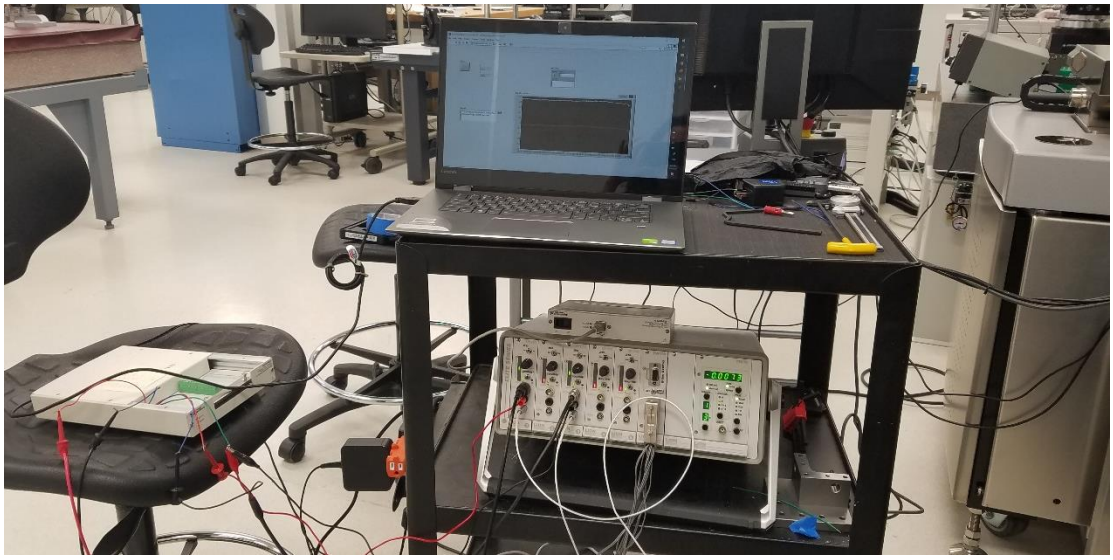

FIGURE 38: First part of setup of the capacitance probe testing with Lion Precision CPL 290 Module, NI USB-6251 DAQ and laptop with LabVIEW program

FIGURE 39: Second part of setup of capacitance probe testing with NexView stage, Al bar extension, capacitive sensors and their housing

The coefficient of thermal expansion (CTE) of aluminum (~24 µm/mº C) [74] was also calculated with a temperature change of 0.1º C in both the length of x and y of the bar where the bar could expand approximately 0.36 µm in x and 0.06 µm in y. The capacitance probes were connected to the CPL 290 modules that were used in high sensitivity (2000 mV/µm) mode so that the resolution of the probes yielded 0.15 nm. The probe resolution was calculated by dividing the resolution of the DAQ by the sensitivity of the module. A 16-bit DAQ was used instead of a 12-bit DAQ due to a smaller step size of 0.3 mV. The capacitance probes were aligned with the bar extension in both x and y so that they were in the middle of their calibrated range and secured in the housing. The capacitance probe wires were strain relieved by being taped down to the NexView's

vibration isolation table. Before testing, the capacitance probes underwent drift tests in v-bar holders and were checked to see if they were within compliance of the calibrated sensitivity. All the equipment brought into the Metrology Suite was left for 24 hours to reach thermal equilibrium before experiments were run. An experiment was initiated by pressing start in the LabVIEW program and leaving the lab with no one entering or leaving in between. Drift tests were run for a period of 60 minutes with a sampling frequency at 1 KHz.

These capacitance probe experiments were carried out for several reasons; both axes could be simultaneously tested and it was hypothesized as to whether the elevator may be coupled to the Metrology Suite even though the lab floor is isolated from the rest of the first floor in DCH. If the x-carriage is being affected by vibration, then both carriages should be jointly affected since the x-carriage is stacked on the y-carriage within the structural loop.

2.6.1 Capacitance probe testing of the NexView stage motion errors in both x- and y-carriages

Hour drift tests were conducted the day before the spring semester started (1/7/2020 at 4:52 pm) where a colleague helped by standing by the elevator and noting each time it started and stopped with a stopwatch. The elevator starting times, marked on the drift test plot, aligned well with when the change in amplitude occurred for both x- and y-carriages in FIGURE 40. Within the hour, the elevator continuously ran during the second run for a period just under three minutes, which was the longest run. The seventh run, the shortest, ran for only five seconds. The elevator had 11 discrete times that it was started within an hour when it was considered to be low foot traffic in the building.

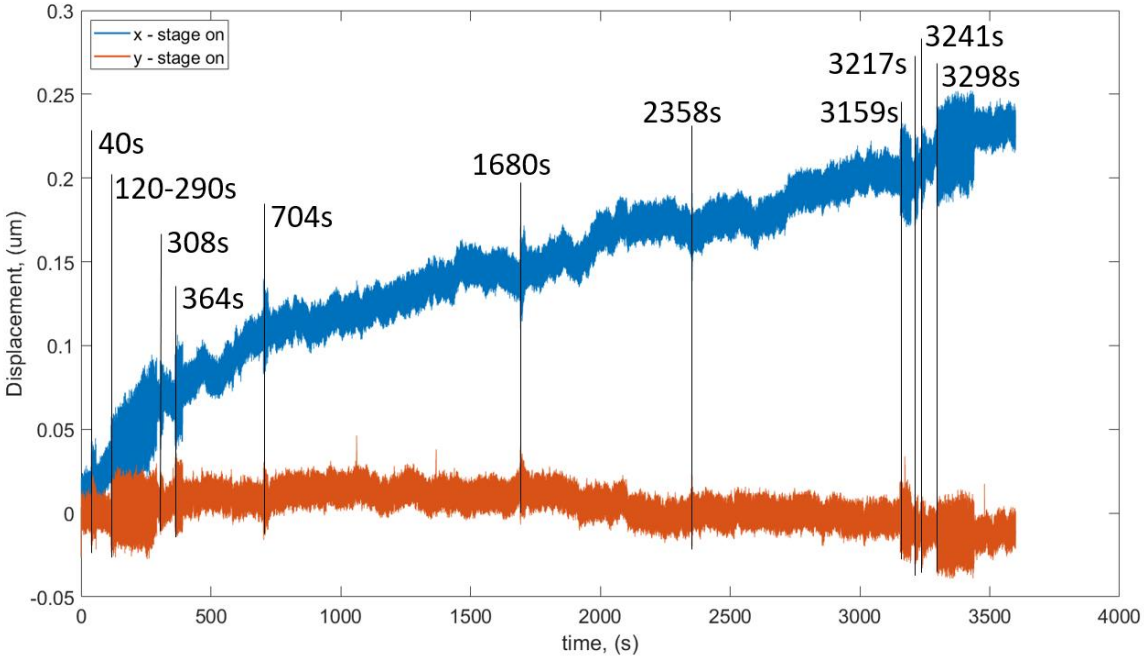

FIGURE 40: An overview of the drift plot in x- and y-carriages where the times were marked when the elevator began running

Drift tests with the stage on and off were made so that when the stage was on, there was approximately 245 nm and 34 nm in the x- and y-carriage respectively over an hour. Having this change in drift within the hour could be due to the uncertainties of the aluminum bar CTE, the probes and wires, or when the stage is on because when the stage was off, the drift was 140 nm and 100 nm for x- and y-carriage. There was also a capacitance probe in a v-bar test that was conducted where the drift was 140 nm for the probe used in the x-carriage as well, but only 3 nm for the probe used in the y-carriage. This drift test for when the stage was off was done on 12/24/19 between 6:09 – 7:16 pm, which was a time that the building was nearly empty. It was also noted that the elevator was used three times, around 7, 17 and 49 minutes where the amplitude has notably increased.

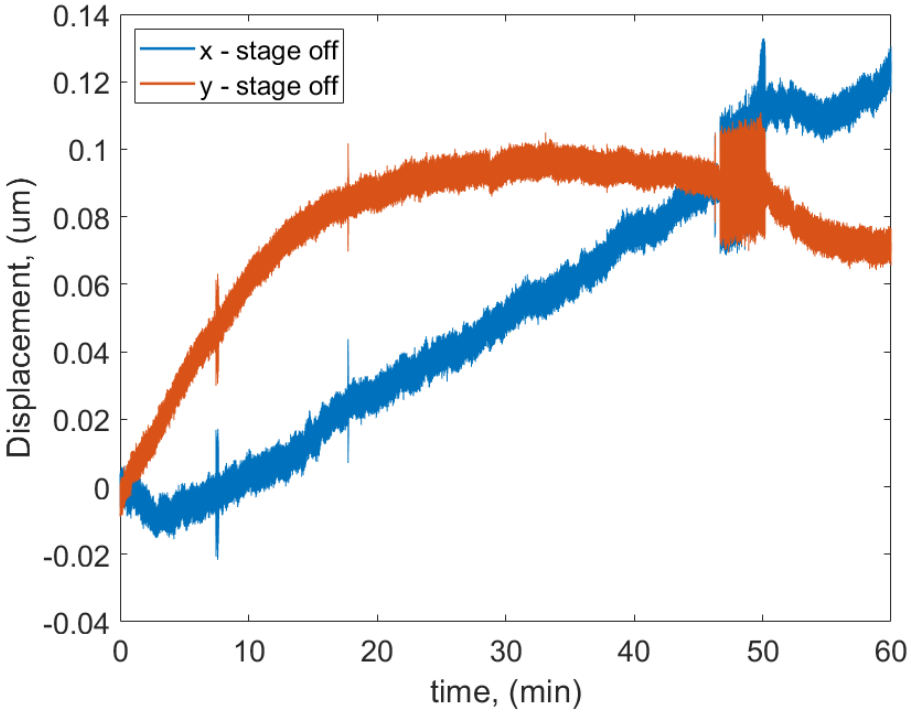

FIGURE 41: Drift test of the x- and y-carriages when the NexView stage was off

Each run was looked at more closely in MATLAB where the local minimum and maximum PV were found within each run, noted in TABLE 11. The minimum PV values, which some have been rounded up are close to the resolution of the probes. The maximum PV values in both the x- and y-carriages for the capacitance probe testing were within range of the DMI tests, but the y-carriage values fell within the lower set of values in that DMI range.

TABLE 11: Local PV of stage motion in the x- and y-carriage for each run during the hour

Run	Local min - max PV in x (nm)	Local min - max PV in y (nm)
1	0.2 – 49	0.3 – 37
2	0.3 – 62	0.3 – 45
3	0.2 – 48	0.2 – 34
4	0.3 – 58	0.2 – 44
5	0.3 – 55	0.3 – 39
6	0.3 – 56	0.2 – 41
7	0.2 – 52	0.2 – 41
8	0.3 – 55	0.2 – 56
9	0.3 – 50	0.3 – 40
10	0.2 – 48	0.2 – 36
11	0.3 – 58	0.2 – 46

The change in amplitude for the runs with both the stage on and off was looked into more closely, applying a Gaussian filter with a window of three to smooth out the data and zooming in. When the stage is on for run 4, in the x-carriage, the PV hovers around 10 nm, but begins to increase to 18 nm when the elevator has started. It continues oscillating within the range of 30 – 45 nm while the elevator continues running in FIGURE 42. At the same time in the y-carriage, the PV also drifts normally around 10 nm, which increases to approximately 15 nm when the elevator starts. The y-carriage oscillates between 22 – 28 nm when the elevator continues running.

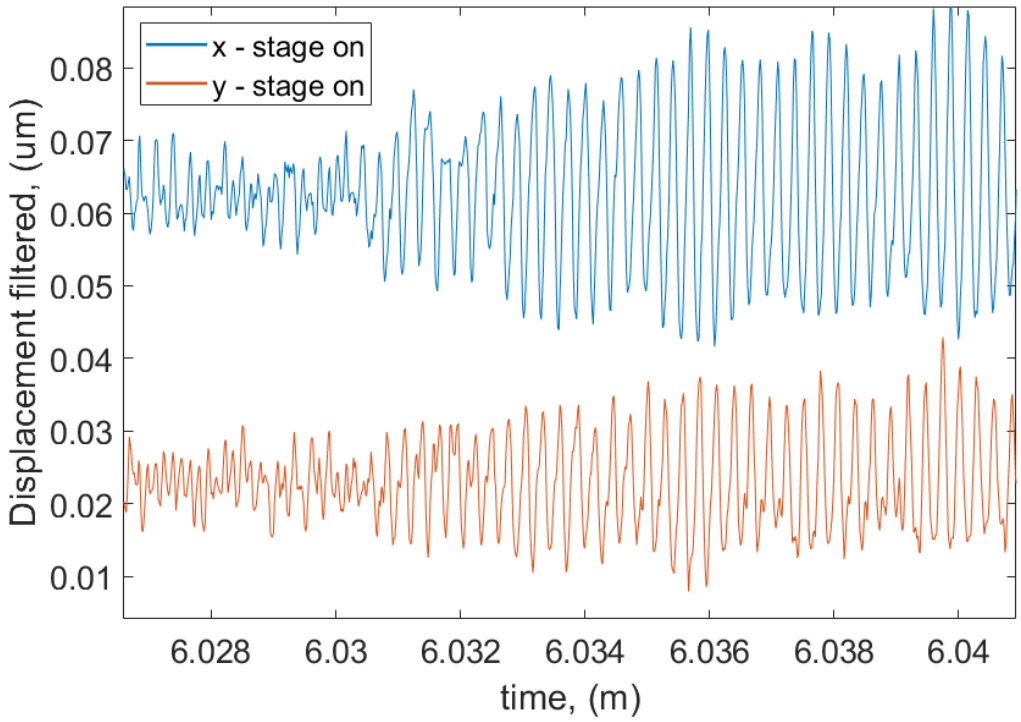

FIGURE 42: Change in amplitude after the elevator starts during the fourth run when the stage is on in the x- and y-carriages, after smoothing out the data

Having the same Gaussian filter as the stage on data, the stage off data for both x- and y-carriages showed a decrease in amplitude of 10 nm (stage on) to 6 nm when the stage is off (FIGURE 43). With the stage off, the x- and y-carriages oscillated between 15 – 25 nm and 13 – 29 nm respectively, which were both a decrease from when the stage was on.

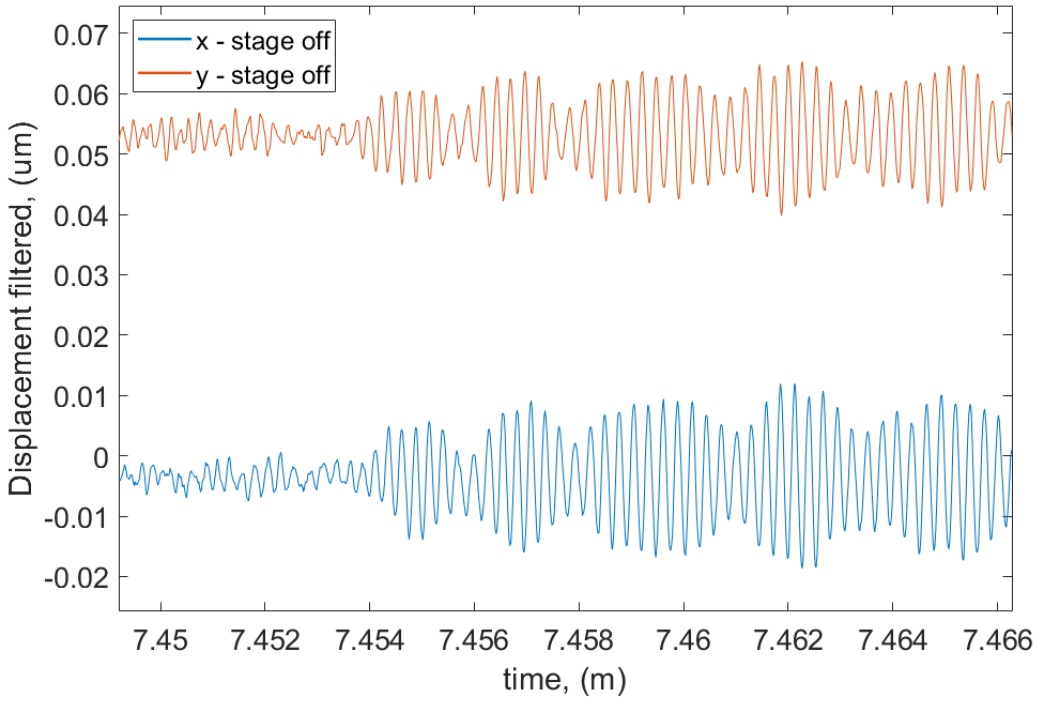

FIGURE 43: Change in amplitude after the elevator starts during the 1st run when the stage is off in the x- and y-carriages, after smoothing out the data

2.7 Concluding remarks about the tests that followed the STR measurements and future recommendations

The MCS of the STR profile data with the random shift generated a very similar plot to the profile that underwent the STR, which suggests that the stage was moving 60 nm when the measurements were being done. The DMI test values fell within the range of the capacitance probe tests for the displacement in both the x- and y-carriages. The hypothesis of the increase in amplitude in the stage motion errors was the elevator, which was confirmed by the 11 elevator runs in the capacitance probe data.

CHAPTER 3: CHARACTERIZING AND TESTING PROFILOMETERS, SPECIFICALLY THE MAHR LD 260

3.1 Introduction to tactile profilometry, exemplary level 2 data

With nearly a century of history in development [75], [76], stylus profilometers are another class of instruments commonly used to measure roughness, waviness, and form (typically referred to as finish, MSFs and figure of optical surfaces). Roughness measurements are limited at high spatial frequencies by stylus geometries such as size and shape [77], [78]. Waviness and form metrology are limited by measurable slopes, curvatures, sag range, and resolution parallel to the "aperture" [79]. Stylus instruments can be configured with additional axes allowing areal surface measurements by combining traces taken sequentially. This increases measurement time and susceptibility to drift.

Stylus profilers typically use a contact probe that travels over the surface at a constant speed. As the probe scans, the vertical movement (movement in Z) is sensed by the transducer, which converts the mechanical motion to an electrical signal [80]. The signal gets amplified and collected by a DAQ where the surface profile gets generated. Vertical resolution is limited by the transducer in the probe or mechanical noise during traversing, which can be in the sub-nanometer range [81]. The subtraction technique of two topography profiles or the averaging of N measurements according to ISO 25178-701 [82] can be done to determine the profilometer's measurement noise [83]–[85]. The subtraction method is comparable to method 1 in Section 2.3.1 as the averaging technique is comparable to method 2 (also in Section 2.3.1), but for a profile instead of a surface.

A sample is placed on the stage where either the stage, probe, or even both move. Probe geometry affects the CDs as flank angles or the probe tip radius vary. Lateral resolution is limited by the contact area of the probe tip with the optical surface, which is dependent upon the tip diameter, probe loads and the optical surface hardness [81]. Small, fine tip diameters yield higher lateral resolutions, although the output is morphologically filtered by the probe radius [86]. FIGURE 44 demonstrates that even a small 2 µm probe tip acts as a filter affecting the spatial frequencies. To avoid this issue,

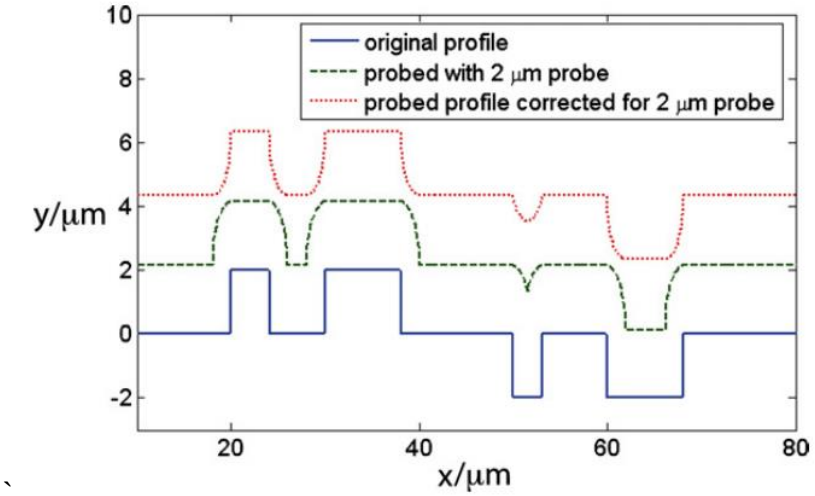

FIGURE 44: True profile data compared to the probed and corrected data [86], note that the three profiles have been offset in the y-axis for visibility and clarity

a specification for defining and filtering the surface texture can be done according to ISO 25178-3 [86], [87]. Tips with large radii or flank angles are not able to trace a surface with steep valleys so the surface data reported is a filtered version of the "true" geometry [47]. The stylus system's ability to trace the surface geometry without losing contact has been characterized as the system's frequency response or "trackability", which is related to probe dynamics and scan speed [88], [89]. Probe force must be considered when

measuring to avoid damaging the optical surface. Surface damage occurs when the Hertzian stress resulting from stylus contact is greater than the yield strength of the material's surface [89], [90].

3.2 FOMCD of the Mahr Profilometer LD 260, exemplary level 3 data

The Mahr LD 260 (FIGURE 45), located in the Metrology Suite next to the Zygo NexView, is used with either the diamond or ruby styli, where a probe tip force can be set between 0.5 and 30 mN [9]. The diamond stylus that has a nominal 2.5 µm probe tip, which, by industry standards, may be between 2 – 4 µm [9] with a 60 degree flank angle. The ruby tipped probe has a nominal radius of 500 µm. The Mahr instrument at UNCC is configured with an additional linear (Y) axis, an Aerotech ABL 1500, which is an air-bearing direct drive linear stage that can travel up to 200 mm with a load capacity 35 kg. Stacked on the Y axis is an air bearing rotary table (B axis). Fine Z travel is provided by arcuate motion of a 100 mm probe arm which provides 13 mm of vertical travel. Longer Z travel to accommodate varying thicknesses of parts is provided, but never used during a measurement.

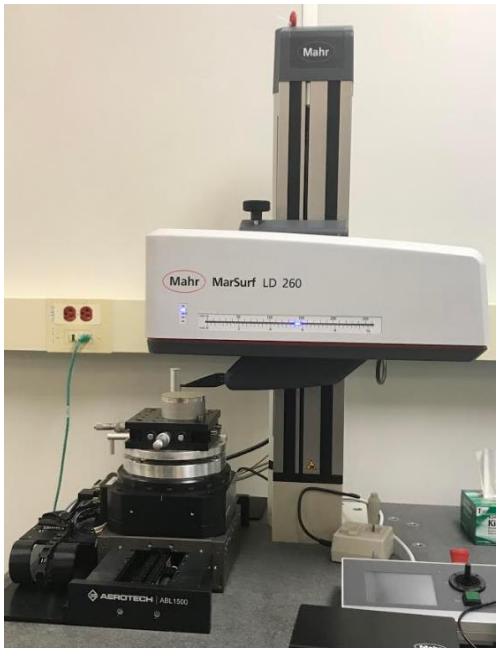

FIGURE 45: Mahr Profilometer LD 260 measuring a DT surface located in the Metrology Suite

In FIGURE 46, λ_{max} and Z_{max} are set by the limits of the instrument itself, the Mahr LD 260, which have a maximum lateral and vertical range of 260 mm and 13 mm respectively [9]. The limit in the y-axis, an additional dimension that comes from the maximum travel of the Aerotech stage is 200 mm. The specifications for the Mahr LD 260 list both the vertical resolution as 0.8 nm and the residual noise that is less than 20 nm Rz [9], where Rz averages the vertical distance of the five highest peaks and deepest valleys [91]. The ambiguous term “vertical resolution” among manufacturers for optical instruments such as SWLIs [58], [85] applies equally to profilometers. In this case for the Mahr CD, Z_{min} will refer to the vertical resolution (least count) of 0.8 nm, noting that an average of 400 measurements would be required to bring the quoted “residual noise” close to this.

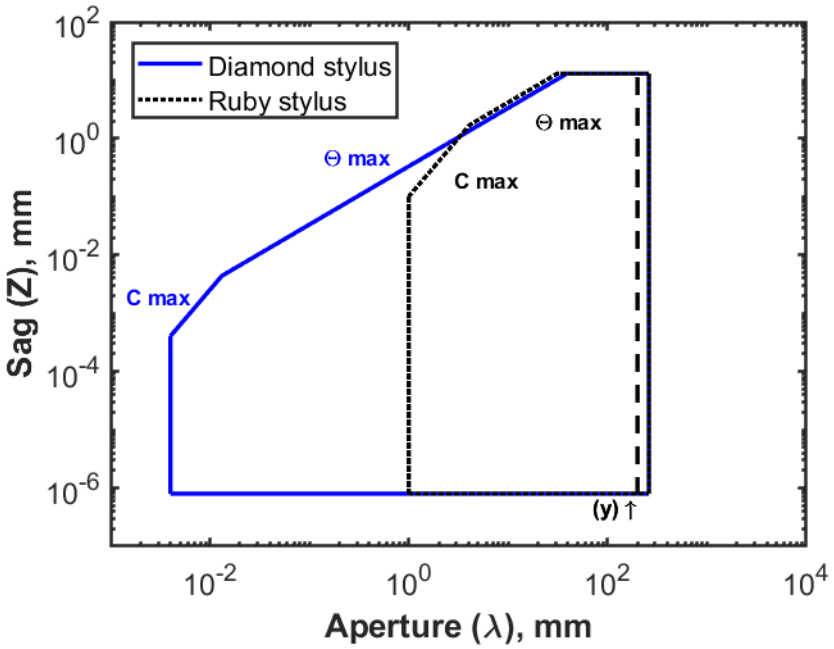

FIGURE 46: CD for the Mahr LD 260 with the available styli at UNCC

TABLE 12: Numerical limits for the Mahr LD 260 with both styli

	Unit	**Diamond**	**Ruby**
θ_{max}	(deg)	60	75
C_{max} **(1/** R_{min}**)**	(1/mm)	500	2
λ_{min}	(µm)	0.004	1
λ_{max}	(mm)	260	260
Z_{min}	(mm)	0.8e-6	0.8e-6
Z_{max}	(mm)	13	13

For the measurement of figure of freeform optics using the Mahr LD 260, circular apertures approaching 260 mm diameter can be measured using Z and B axes with uneven data spacing. A variety of measurement strategies using all 3 axes are being explored that allow compensation of thermal drifts.

3.2.1 Details relating the slope limits to the FOMCD for the Mahr LD 260

The maximum slope is a function of the probe tip geometry. As the flank angle increases, the maximum slope line (θ_{max}) shifts in and down causing the "measurement area" to decrease. The maximum curvature and the lateral resolution are dependent upon the probe tip radius. As the radius decreases, "features to measure" increase, thus shifting the C_{max} line out and up in the CD. Large probe tip radii or flank angles will limit measuring higher spatial frequencies (shorter wavelengths), which shows the left side of the CD for the ruby in FIGURE 46 starting at 1 mm whereas the left side of the CD for the diamond starts at 4 micrometers. The volume of the CD for the ruby is smaller than the CD for the diamond since the ruby's radius is 250 times the size of the diamond, limiting measurable surface features.

3.3 Experiments using the Mahr LD 260, a continuation of level 3 data

3.3.1 Testing of probe force (load) and metrologist's viewpoints on tactile profilometry

Measuring an optical surface with a tactile probe carries opposing viewpoints for metrologists on using profilometry, where one critical reason is dealing with surface damage. On one side, Thomas argues that tactile profilers are too slow, delicate and cause an unknown amount of surface damage [75], [92] whereas Whitehouse explains that when stylus pressures are accounted for in elastic theory and are less than the yield stress of the material, damage will not occur [89], [90]. Church et al has an impartial view towards optical and tactile profilers after measuring random and periodic surfaces because both instrument types demonstrated quantitative agreement after applying the appropriate filters and accounting for the bandwidths [64].

3.3.2 Profilometer load testing setup for the Mahr LD 260

Four optics of different materials under five different loads were tested taking traces from the Mahr LD 260 from both the diamond and ruby styli. The materials were DT copper (Cu) coated brass substrate, DT electrodeposited NiP coated brass substrate, naval brass 464 and BK7. The five probe loads were 1, 5, 10, 20 and 30 mN. The diamond and ruby traces were spaced 1 mm apart from either side of the center line and from each load as illustrated in FIGURE 47. This 1 mm spacing helped to locate the traces when they were analyzed and measured with the SWLI, Zygo NexView 50x objective. Theoretical Hertzian stresses were calculated for each case considering the contact area of a sphere (stylus) and a plane (material) and then compared to the actual experiment [93], [94]. (MATLAB code for all Hertzian stress figures is in Appendix F).

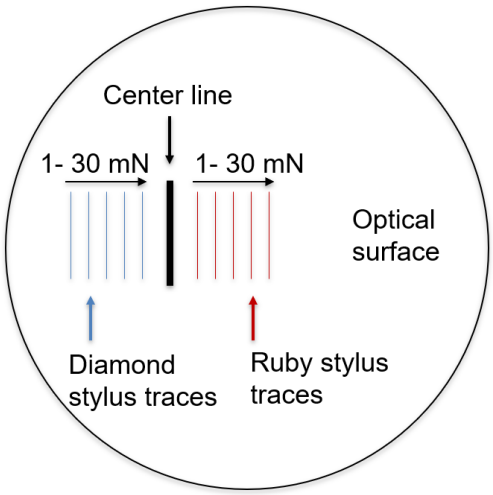

FIGURE 47: Setup of how the profilometer traces were made on each of the optical surfaces

3.3.3 Results of the Mahr profilometer data

The following plots show the calculated Hertzian stresses on a log scale as the ruby and diamond are run at the five loads on each material. A theoretical yield strength of the material was also plotted and compared to the Hertzian stresses to see how well the theoretical values related to the experimental results. The gray range on the plots is an area where the actual yield strength of the material lies according to the experiments. With each material, this area was set between the two loads where the traces were visible and not visible with the NexView.

The yield strength of the electrodeposited NiP coating was greater than the Hertzian stress for all the ruby traces, which matched the experimental results because there were no traces found on the sample's surface (FIGURE 48). The NexView results showed that there were no marks from the diamond stylus 1 mN load (FIGURE 49 (a) however, theoretically, the Hertzian stress exceeded the yield strength. It is uncommon for manufacturers of plated materials to disclose mechanical properties so an estimated yield strength for electroplated NiP based on experiments [95] was used for these calculations. One source of error from the Hertzian stress calculations was that work hardening of the NiP during diamond turning was not taken into consideration; recent investigations suggest that some level of transformation from amorphous include intermetallic formation may be taking place. Further work in this area is required.

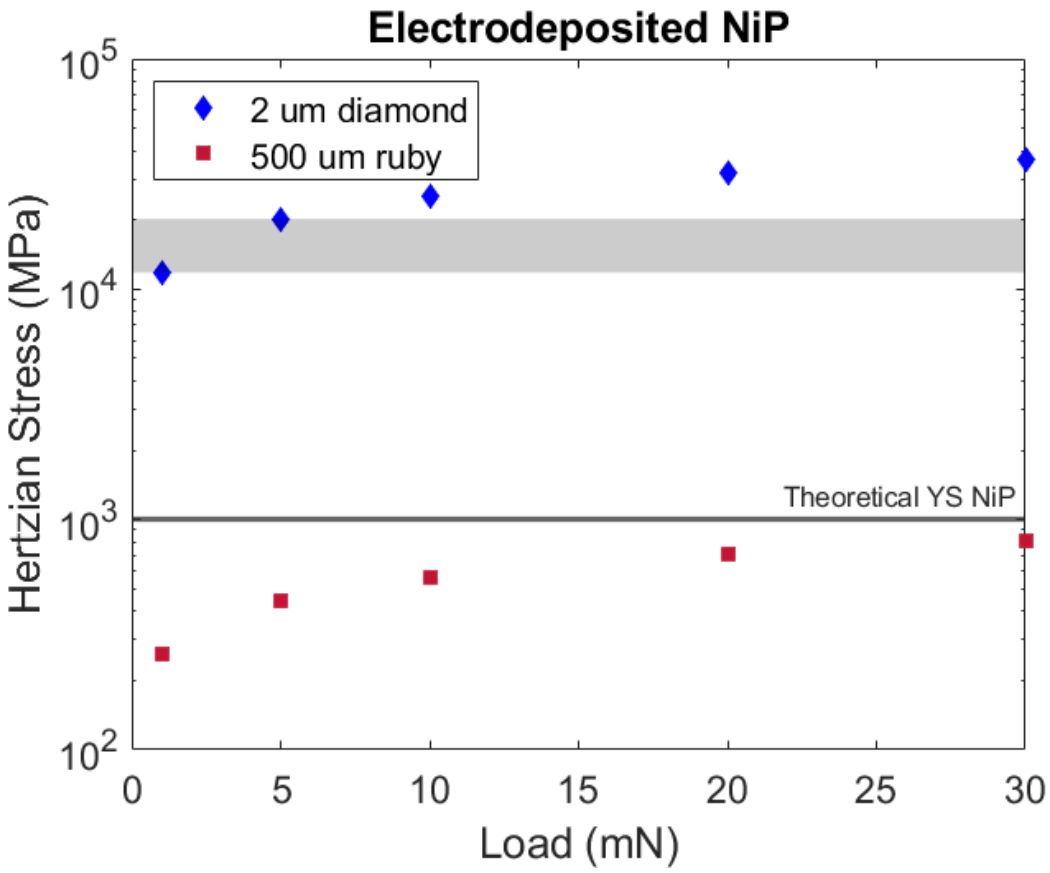

FIGURE 48: Hertzian stresses as a function of load for electrodeposited NiP

A trace of the diamond stylus with the 5 mN load in FIGURE 49 (b) was apparent causing plastic deformation.

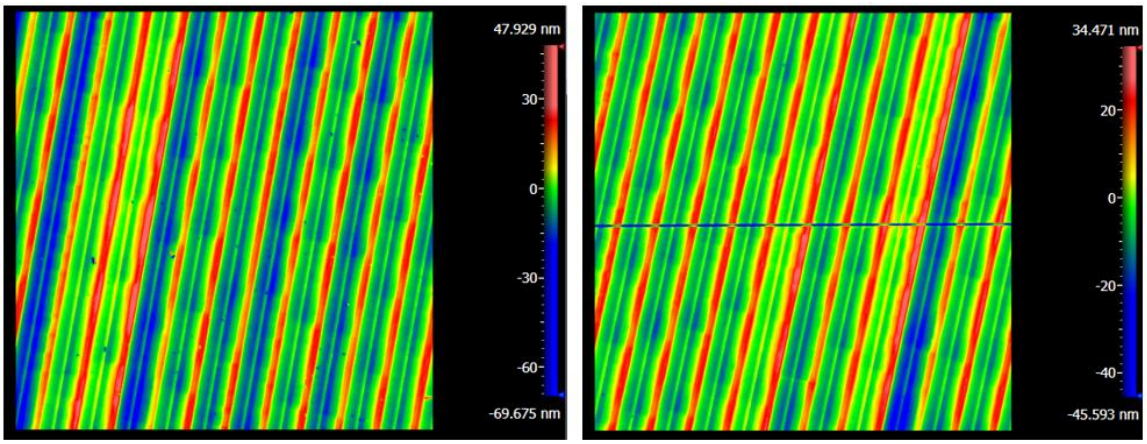

FIGURE 49: 50x objective interferograms of DT electrodeposited NiP after traces of (a) 1 mN load and (b) 5 mN load using diamond stylus

Plane was filtered from the measurement and a slice was taken perpendicular to the stylus motion showing an approximate groove depth of 25 nm in FIGURE 50.

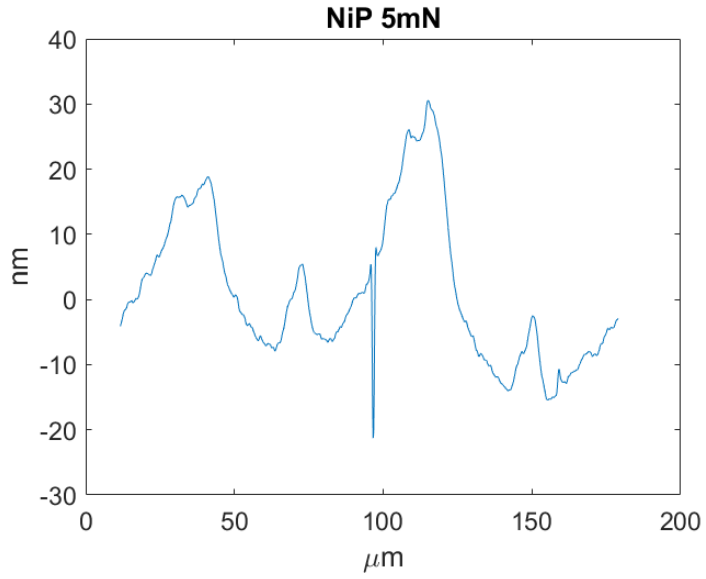

FIGURE 50: Groove in NiP caused by the diamond stylus at a 5 mN load

For loads 10, 20 and 30 mN, plane and a low pass FFT filter were used for the interferograms. Loads of 10, 20 and 30 mN also showed groove depths of 70, 230 and 570 nm respectively and plowed material on either side of the trace.

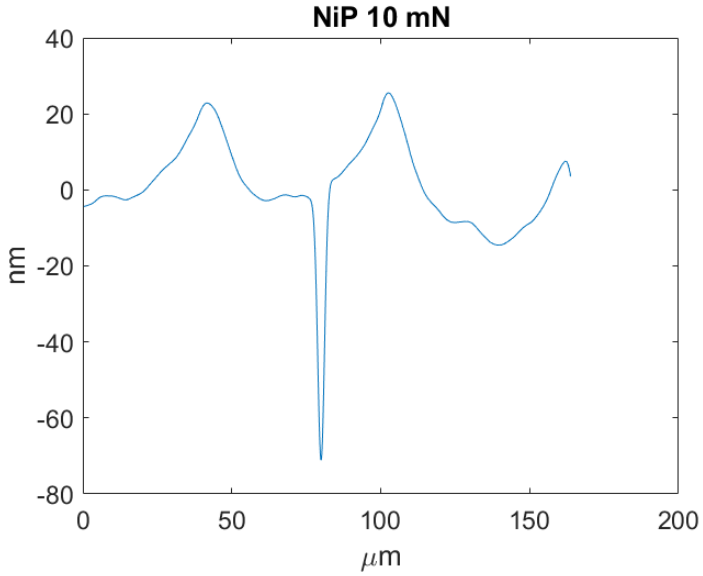

FIGURE 51: Groove in NiP caused by the diamond stylus at a 10 mN load

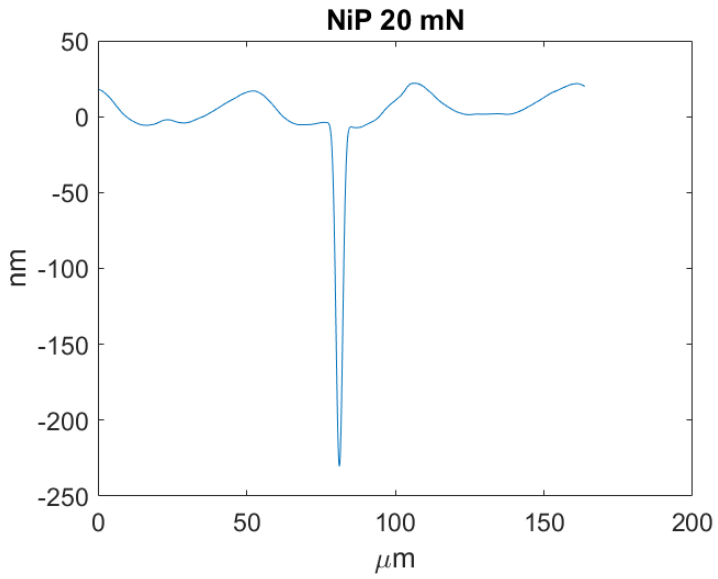

FIGURE 52: Groove in NiP caused by the diamond stylus at a 10 mN load

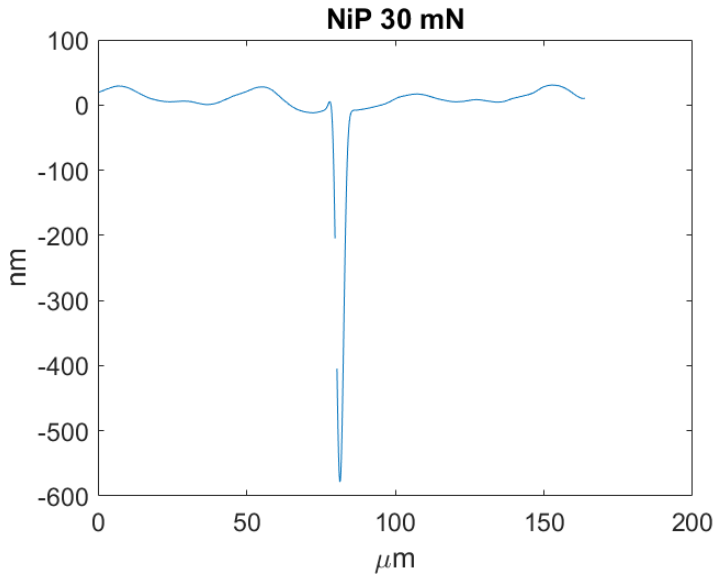

FIGURE 53: Groove in NiP caused by the diamond stylus at a 30 mN load

In FIGURES 50 – 53 across the surface, there is a repeating cusp structure at the bottom of the DT cusps, known as a secondary helix. This signifies tool wear damage to

the nose of the diamond tool, which is also shown in FIGURE 54 with a trace taken perpendicular to the lay.

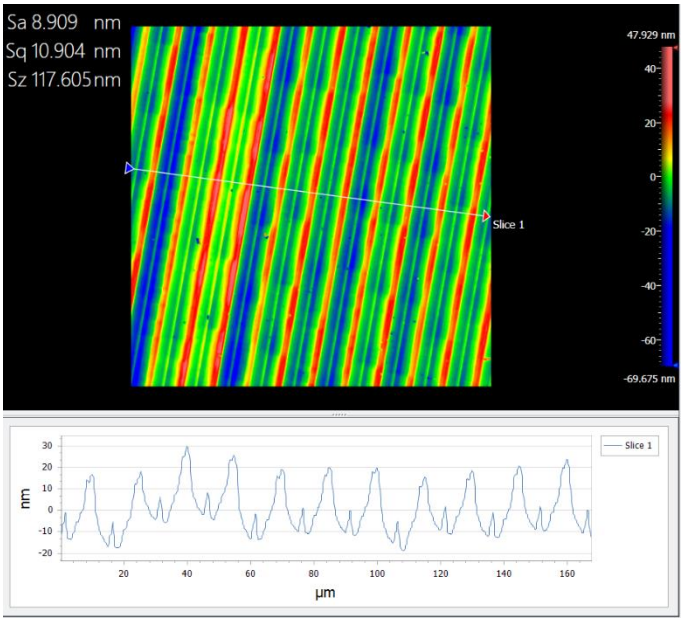

FIGURE 54: Diamond tool wear damage at the bottom of the cusp structure

As shown in the NexView data, all traces but the 1 mN ruby trace produced deformation on the copper surface (FIGURE 55). The yield strength of the copper coating [96] was estimated close to the literature value because the experimental data corresponded to the theoretical Hertzian stresses.

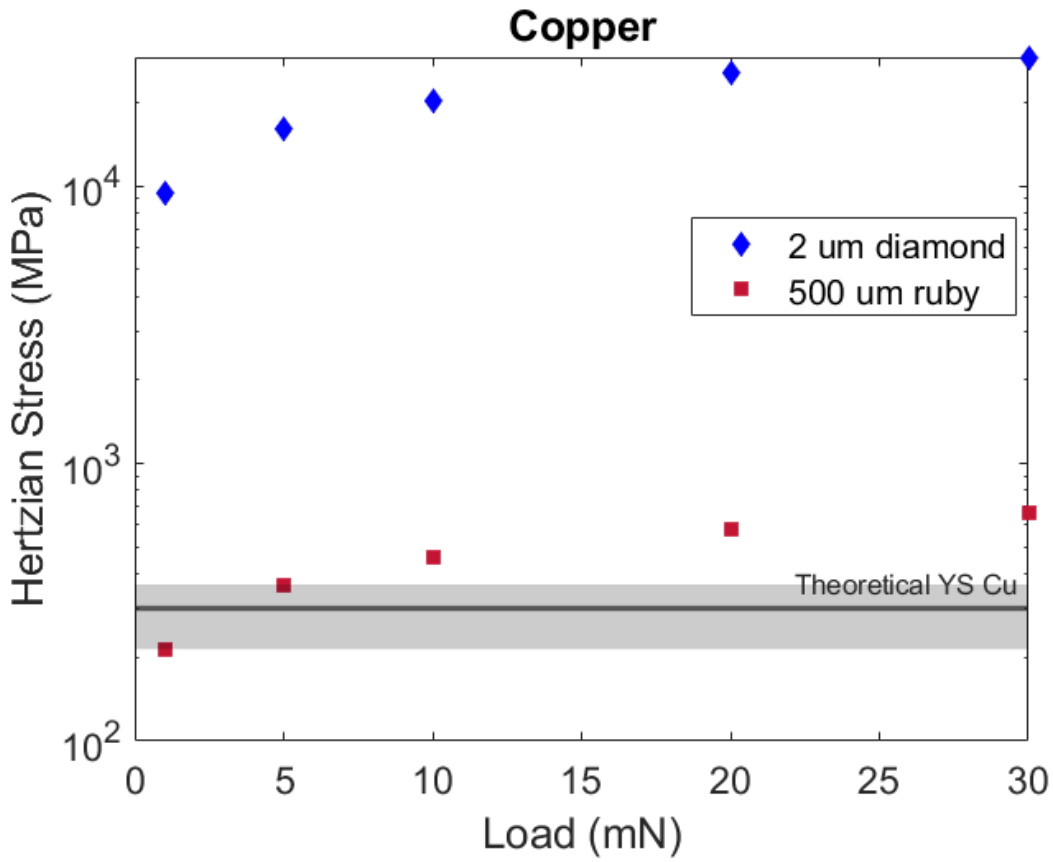

FIGURE 55: Hertzian stresses as a function of the load for copper

The traces from the ruby stylus suggest that the stylus may be damaged since increasing the load from 1 mN to 5 mN showed 2 separate indented traces in FIGURE 56.

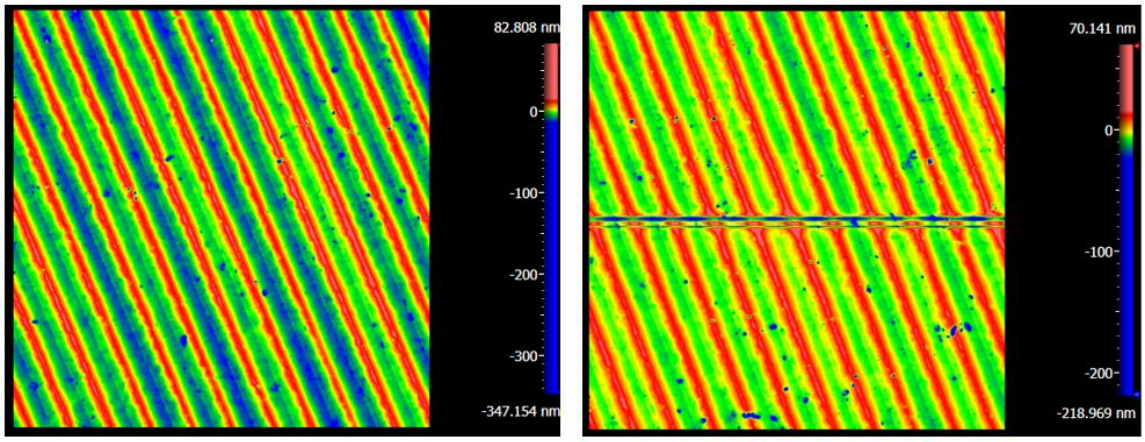

FIGURE 56: 50x objective interferograms of Cu after (a) no trace with 1 mN 1oad and (b) a trace with 5 mN load using ruby stylus

Two traces from the ruby showed up in the 10, 20 and 30 mN as well becoming more pronounced in the material as the load increased (FIGURE 57).

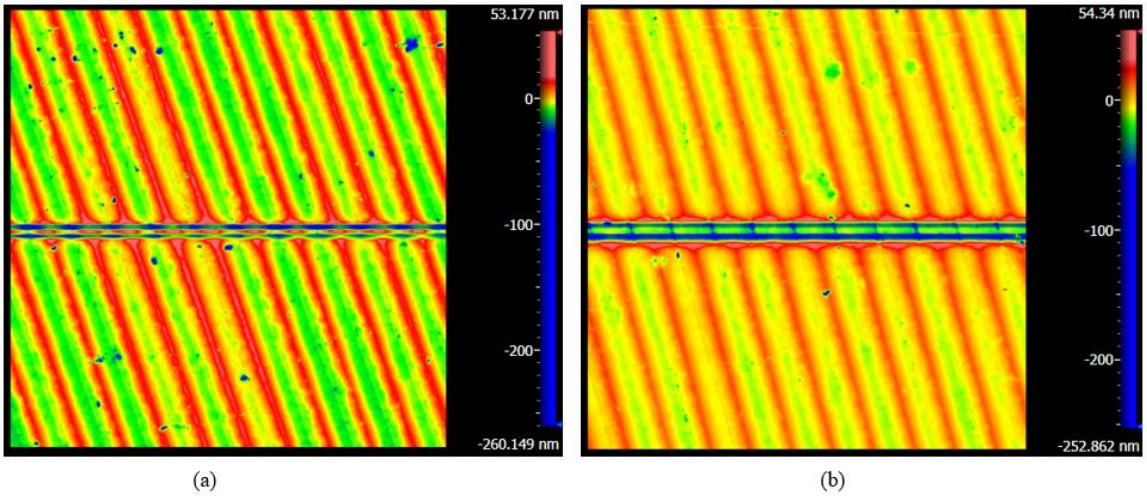

FIGURE 57: 50x objective interferograms of Cu after traces of (a) 10 mN load and (b) 30 mN load using ruby stylus

A slice between the cusp marks from the interferogram in FIGURE 58 (b) of the 5 mN load indeed had two grooves, which were approximately 25 and 21 nm deep and 5 µm apart from the peaks of the plowed-up material.

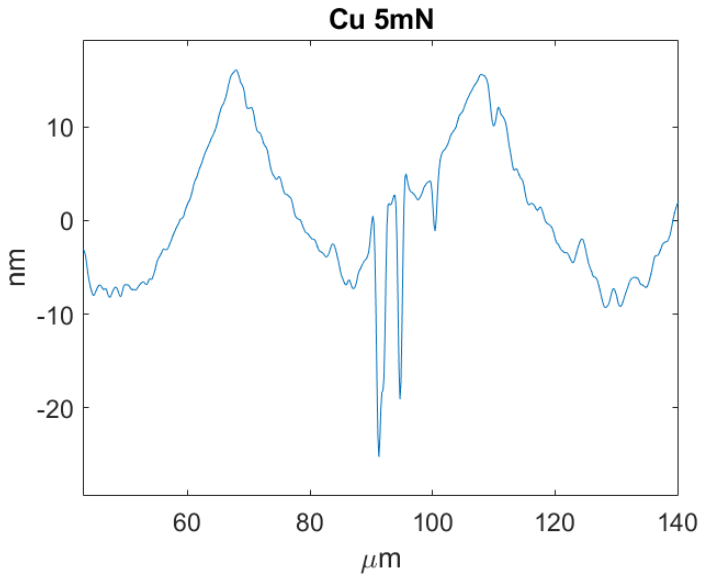

FIGURE 58: Two grooves in DT copper caused by the ruby stylus at a 5 mN load zoomed in

In Mx, laying a slice over the trace in the 10 mN load interferogram and moving the entire slice down showed that the peaks were plowed down and the material was moved, which is evident when looking from FIGURE 56 (a) to FIGURE 57 (b) where the trace was made. By the time the 30 mN load trace was made, the ruby was plowing through the DT copper leaving material on both sides. Grooves could be seen with a slice that was placed orthogonal to the trace. The two grooves were between 80 – 90 nm deep and almost 10 µm apart from the peaks of the plowed-up material in FIGURE 59.

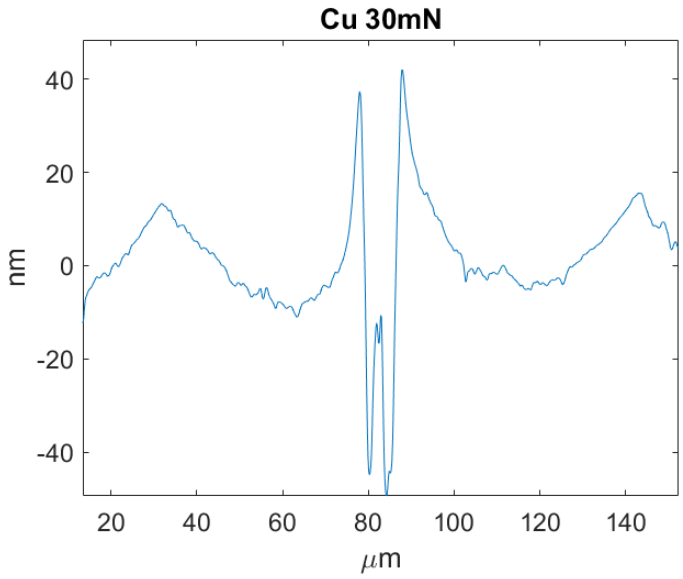

FIGURE 59: Two grooves in DT copper caused by the ruby stylus at a 30 mN load zoomed in

The nose radius of the tool used to DT the copper sample was unknown, but was estimated (~1 mm) using the height and length of the cusp structure when taking a slice orthogonal to the lay in Mx [97]. It is not certain why plastic deformation shows two grooves, so future work with the contact mechanics of the ruby stylus on copper should be looked into further.

The experiment for solid naval brass 464 resulted in no ruby traces present after looking at the NexView interferograms (FIGURE 60). Yield strength handbook values for naval brass 464 did not account for work hardening [98], which may be one source of error in the Hertzian stress calculations for the ruby stylus 20 and 30 mN loads.

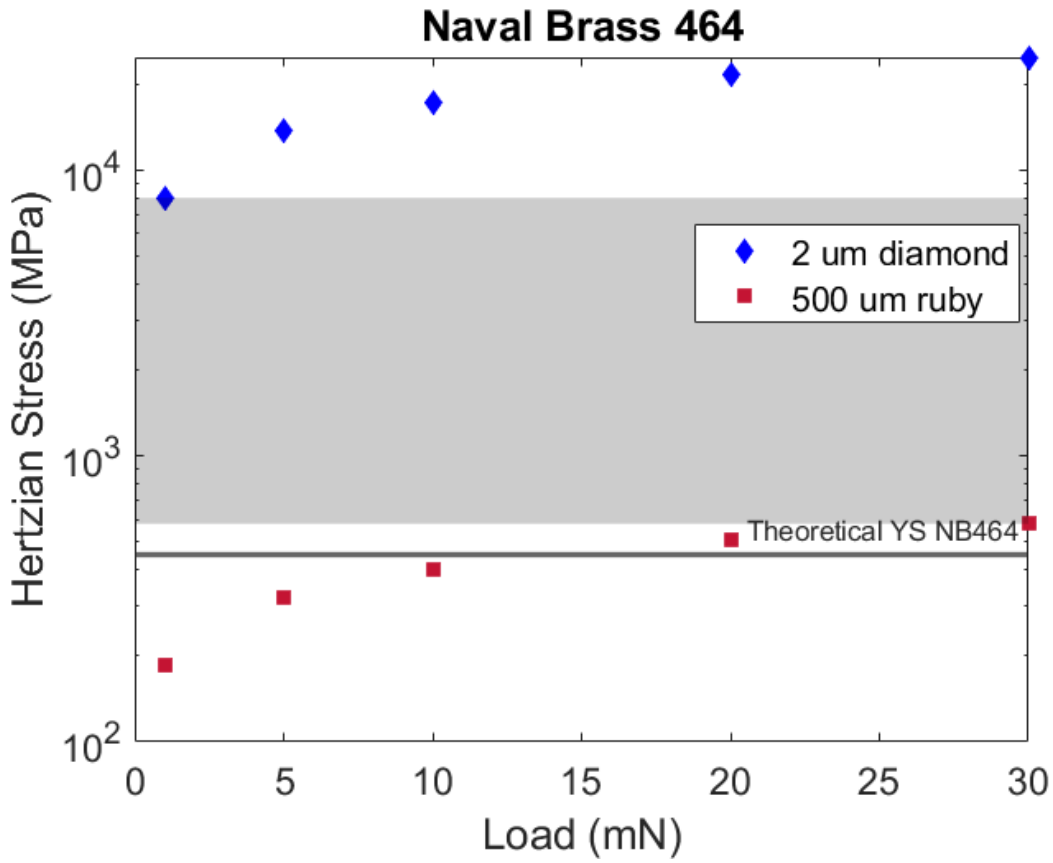

FIGURE 60: Hertzian stresses as a function of the load for naval brass 464

The diamond stylus with a 1 mN load plowed through the brass material leaving a groove that is nearly 490 nm deep in FIGURE 61 (a) & (b). Even with a higher magnification objective, 50x, slopes were too steep to be measured. Most slices had a fraction of the groove shown like the one in FIGURE 61 (b). Brass material was left on both sides above the surface that varied in different heights where here it was almost 370-600 nm high and 3 µm apart peak to peak in FIGURE 61 (b).

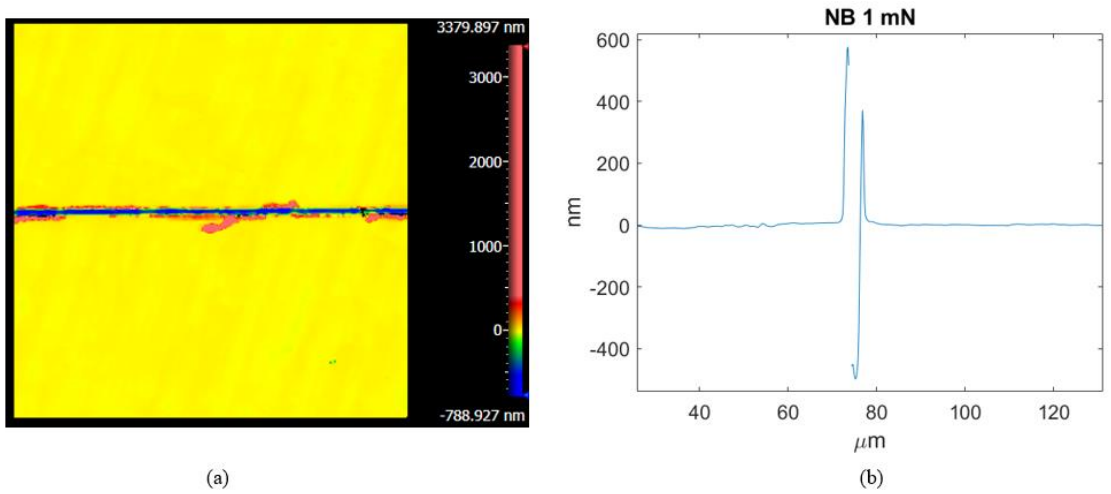

FIGURE 61: (a) 50x objective interferogram of brass after 1 mN diamond trace and (b) slice from the same interferogram in (a)

Another slice with a 30 mN load was observed where the groove depth increased to almost 2 µm and the plowed-up material to nearly 1 µm high and 6 µm apart peak to peak.

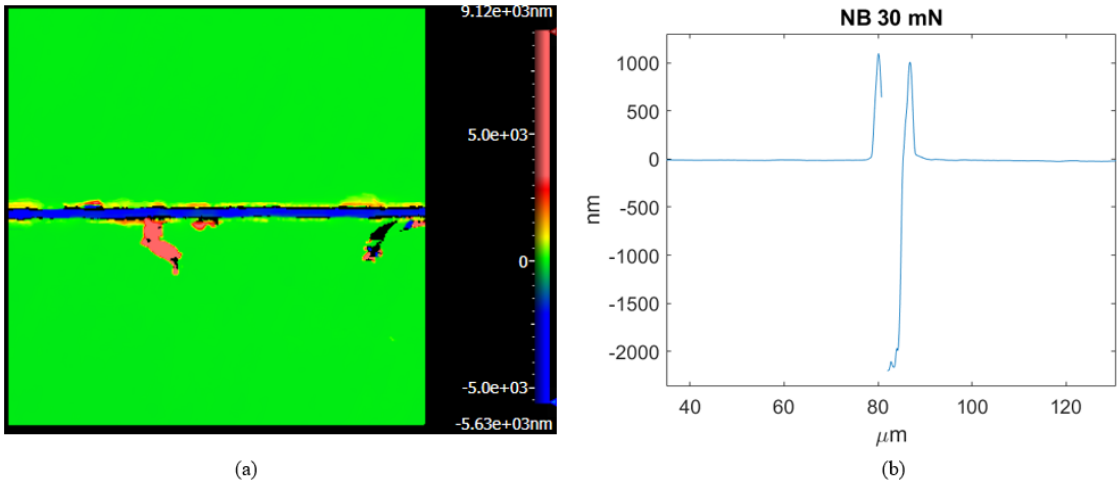

FIGURE 62: (a) 50x objective interferogram of brass after 30 mN diamond trace and (b) slice from the same interferogram in (a)

Optical surfaces that had plastic deformation were examined further according to the depth of the grooves and the loads that were applied. In Mx, slices of grooves were made and then the depths of these grooves were averaged for each material and load. Grooves that were examined above (in FIGURES 50, 58, 59, 61 and 62) had similar trends to the average grooves in FIGURE 63 except for the diamond 1 mN load on naval brass. It was also observed that diamond styli on softer materials like copper and naval brass caused more damage. This was expected since Hertzian stresses are proportional to the load.

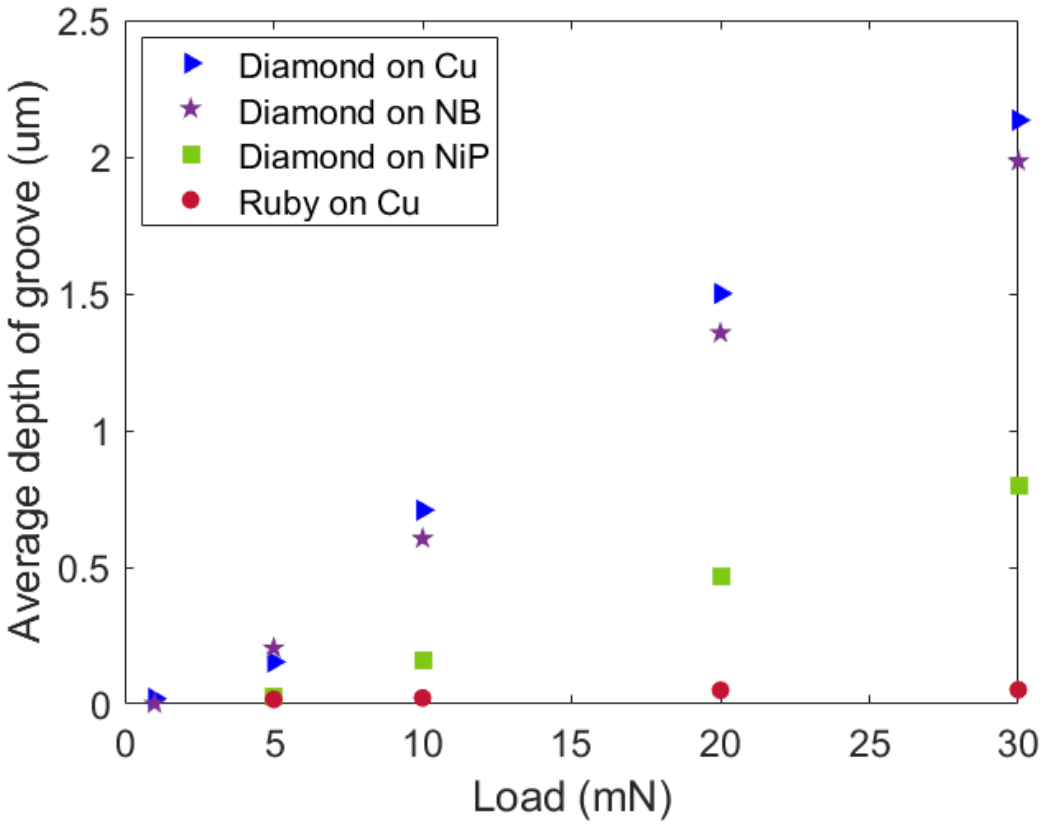

FIGURE 63: Average depth of groove that stylus made with each load

Instead of yield strength, apparent elastic limits are used for BK 7 glass [99], as seen in FIGURE 64.

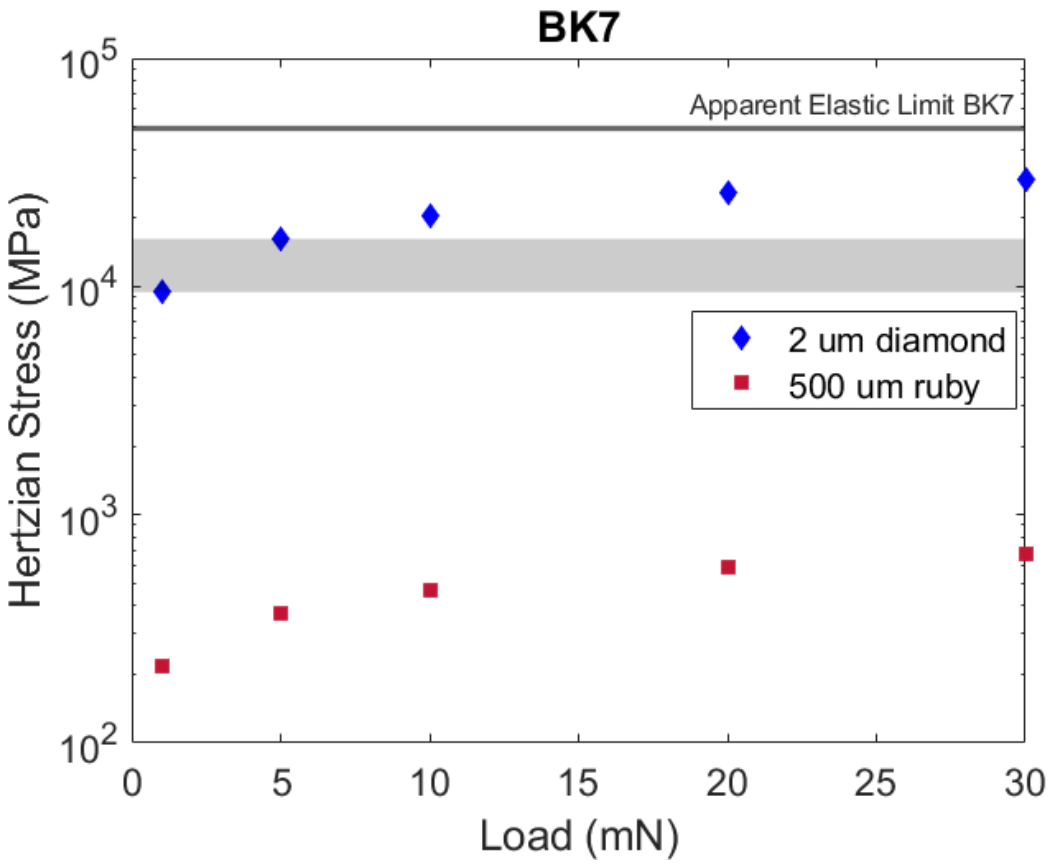

FIGURE 64: Hertzian stresses as a function of the load for BK 7

The experiment resulted in visible traces with the 5, 10, 20 and 30 mN loads for the diamond stylus shown in FIGURE 65 (b), FIGURE 66 (a), (b) and (c) respectively. All measurements had plane filtered where the 30 mN load had an additional high pass filter applied so that the trace was visible. As the load increased so does the PV range of the color bar.

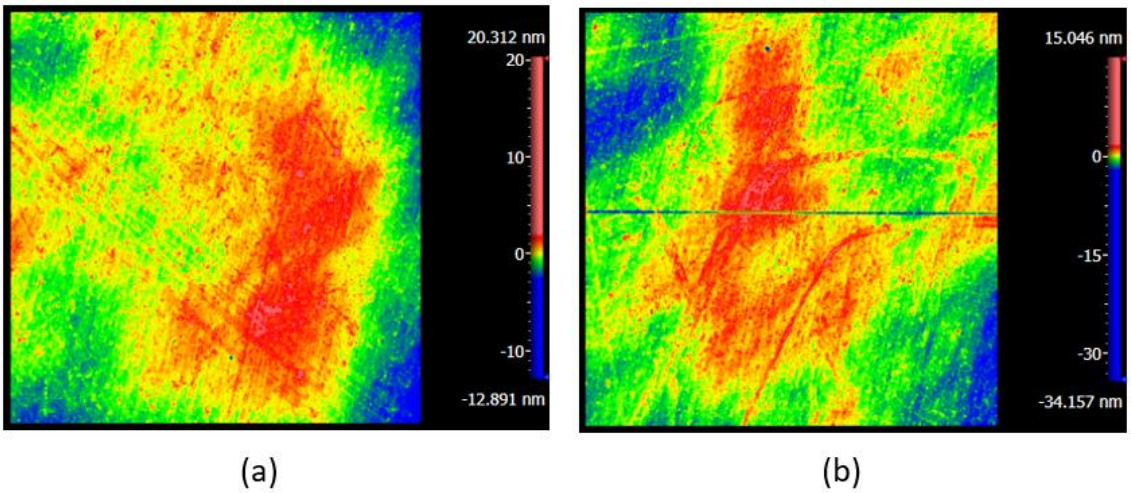

FIGURE 65: 50x objective interferograms of BK 7 after (a) no trace with 1 mN 1oad and (b) a trace with 5 mN load using diamond stylus

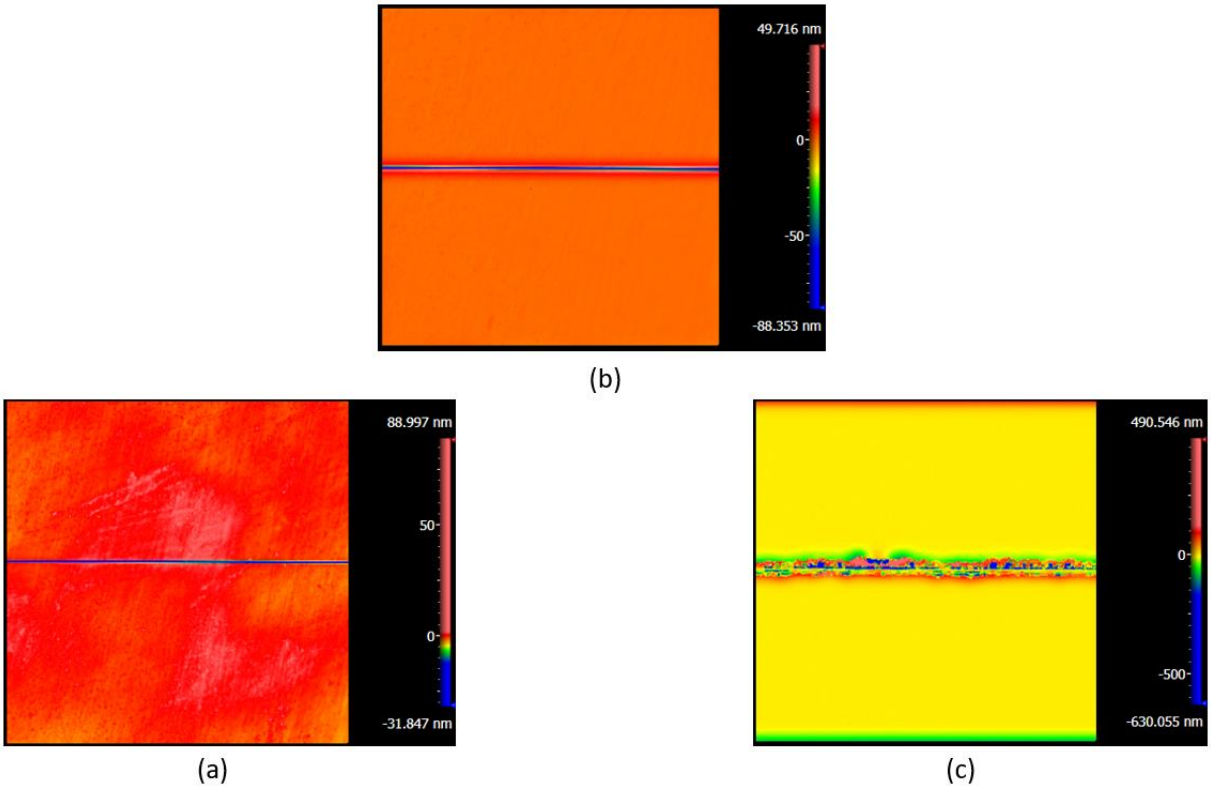

FIGURE 66: 50x objective interferograms of BK 7 after trace with (a) 10 mN (b) 20 mN and (c) 30 mN load using diamond stylus

In the 5 mN load (zoomed in), there was plastic deformation with a groove 2 nm deep (FIGURE 67).

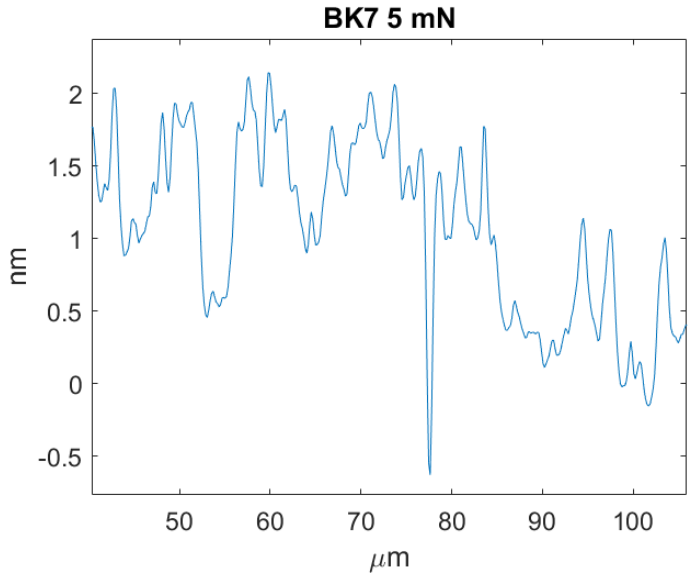

.

FIGURE 67: Groove in BK 7 caused by the diamond stylus at a 5 mN load zoomed in

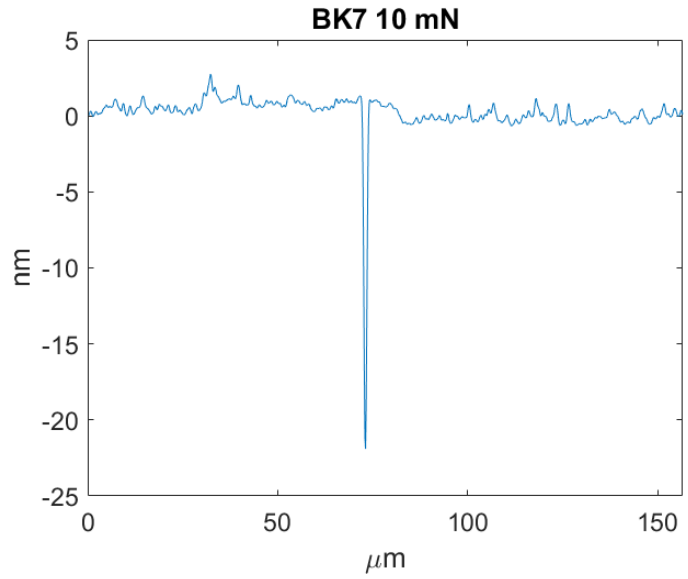

FIGURE 68: Groove in BK 7 caused by the diamond stylus at a 10 mN load

The 10 mN load trace across the BK 7 resulted in nearly a 20 nm deep groove (FIGURE 68). Increasing the load 20 and 30 mN caused plastic deformation with nearly 80 and 600 nm deep grooves as shown in FIGURE 69 and FIGURE 70 respectively. FIGURE 70 also suggests fracture damage as groove depth and material above the surface varied (200 – 600 nm) and (50 – 400 nm) respectively along the trace. Further analysis in crack propagation and fracture of BK 7 at 30 mN could be done.

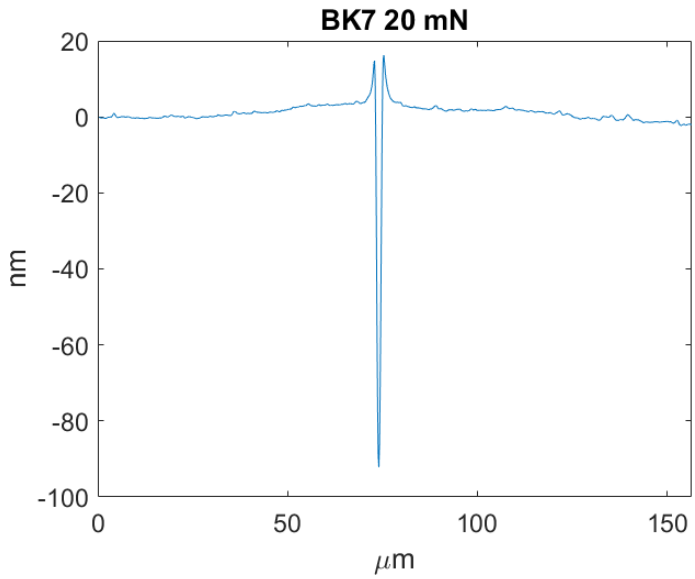

FIGURE 69: Groove in BK 7 caused by the diamond stylus at a 20 mN load

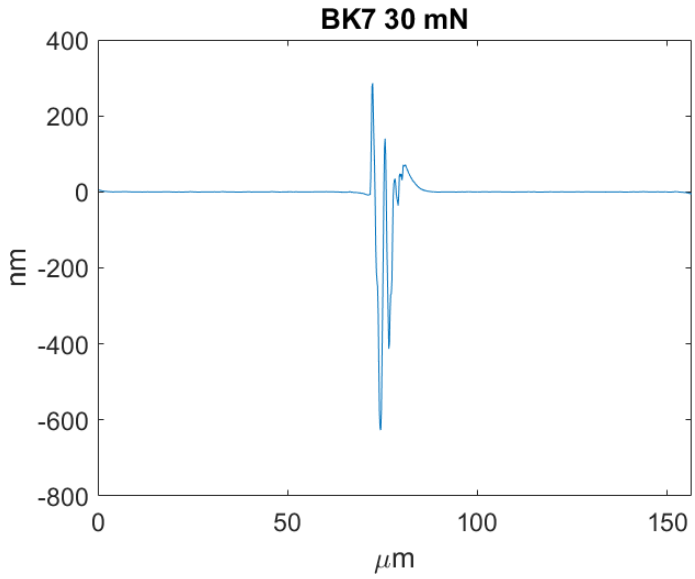

FIGURE 70: Groove in BK 7 caused by diamond stylus 30 mN load

Tactile profilometers are widely used by metrologists, but many optical scientists and engineers recoil in horror at the idea of using them on optical surfaces. Hertzian stresses should be calculated and considered before measuring the optic this way. When the yield strength of an optic's material exceeds the Hertzian stress from the probe's contact, then a stylus profilometer can be safely used, provided the uncertainty in material properties is recognized. The contact mechanics for interaction of spherical probes with diamond turned surface produced with tools of a similar radius need to be investigated.

Apart from testing the Hertzian stresses through experiments, one improvement to the experiment would be to measure the stylus with a SWLI before using and then after each trace. While rapid wear is not expected between diamond and the materials measured, deviations of the probe geometry from the nominal (either from manufacturing or prior use) could have affected the results shown here.

CHAPTER 4: CHARACTERIZING AND TESTING INTERFEROMETERS, SPECIFICALLY THE ZYGO FIZEAU VERIFIRE HD WITH SOME COMPARISONS TO THE ZYGO FIZEAU AT

4.1 Introduction to interferometry, exemplary level 2 data

Interferometers used to measure aspheres and freeforms range from tools in development like multiple wave interferometers (MWI) [100], [101] to tools commercially available such as tilted wave interferometers (TWI) [102], [103] and Fizeau interferometers combined with “nulls”. For rotationally invariant aspheric surfaces, a variety of transmissive null lens designs have been developed [104]. Computer-generated holograms (CGH) [105], [106], have become more common for both aspheric optics and freeforms. The following discussion will be in terms of Fizeau interferometers, which are the most widely deployed high-performance full aperture optical testing method.

Over the last few decades, the demands for metrology tools like Fizeau interferometers have been pushed to measure both form and MSFs of an optical surface [107], [108]. A coherent source gets expanded to a wavefront that is split into two beams, the test and reference beam (FIGURE 71). Light reflected from the surface under

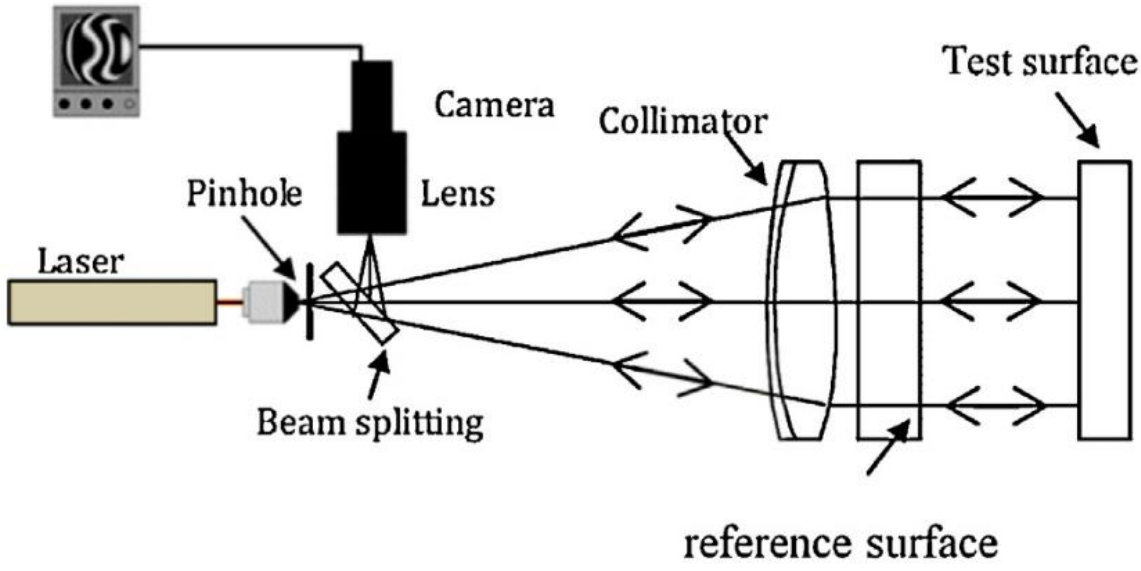

FIGURE 71: Schematic of a Fizeau interferometer [4]

test combines with the light reflected from a known, movable reference surface and produces interference fringes on the CCD. The separation between reference and test surface defines the coherence length required in the source. A variety of Fizeau interferometers are available, most commonly using mechanical phase shifting to modulate phase [109]. Wavelength shifting [110], polarization [111], and carrier fringe implementations [112]. All results given here were obtained using Fizeau interferometers with mechanical phase shifters.

Fizeau interferometers are commercially available with a variety of transmission flats and spheres that allow for measurement of flatness or to a range of departures from specified spherical base radii. The range of transmission spheres (TS) enable measurement of convex surfaces in the converging cone of light or concave surfaces in the diverging cone of light (FIGURE 72) with some constraints.

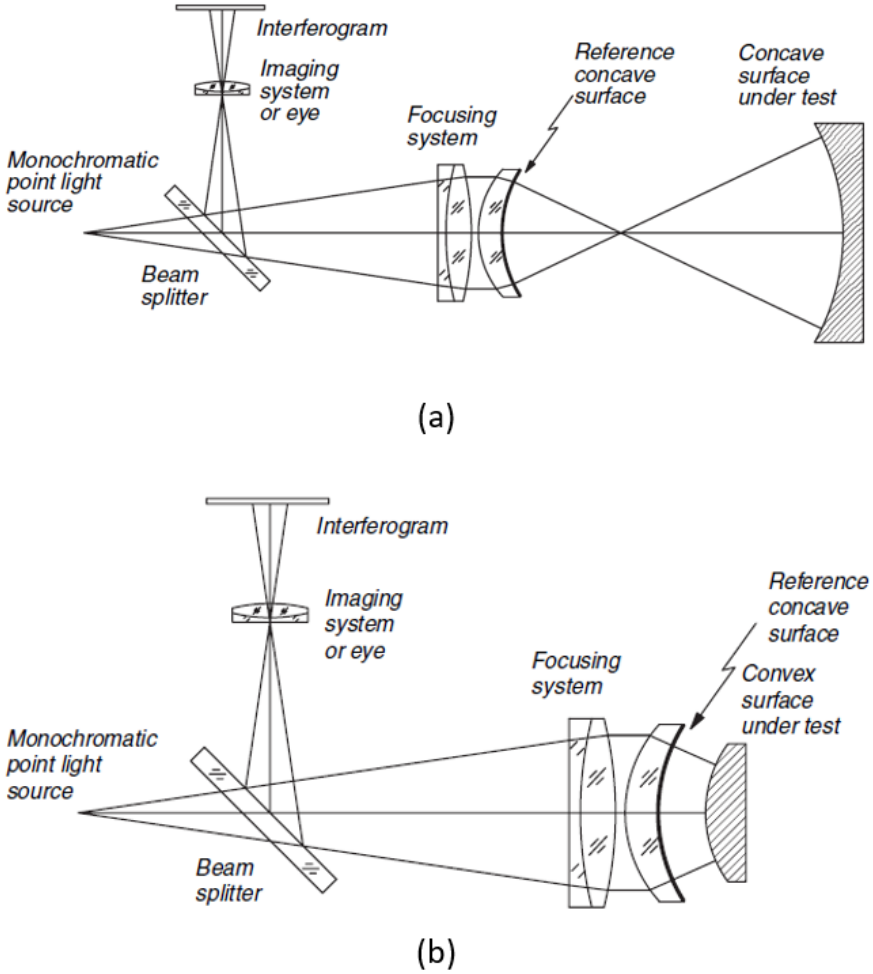

FIGURE 72: Schematic of a Fizeau testing (a) concave surface and (b) convex surface with both using a concave TS [113]

In order to measure an optical surface, the f/# (ratio of focal length/aperture) of a TS must be equal to or "faster" than the R/# (ratio of ROC/clear aperture) of the test surface. A lower f/# represents a faster lens, which in other words, has a wider cone angle of light whereas higher f/#s are slower lenses that have narrower cone angles of light. If the TS is slightly slower, then only a percentage of the surface under test, which is a ratio of the R/# to f/#, will be illuminated and thus measured. Concave test surfaces follow this rule with little restrictions because the diverging part of the cone of light (FIGURE 72

(a)) could extend to the limit imposed by the coherence length of the source. However, longer cavity lengths become more sensitive to air turbulence [114], [115] which, like cavity positioning [116], cause optical path difference (OPD) errors. In FIGURE 73, Sykora points out that TSs relative to different size radii of convex and concave test parts experience non-linear OPD errors in spherical cavities where the maximum errors are at the TS's focus.

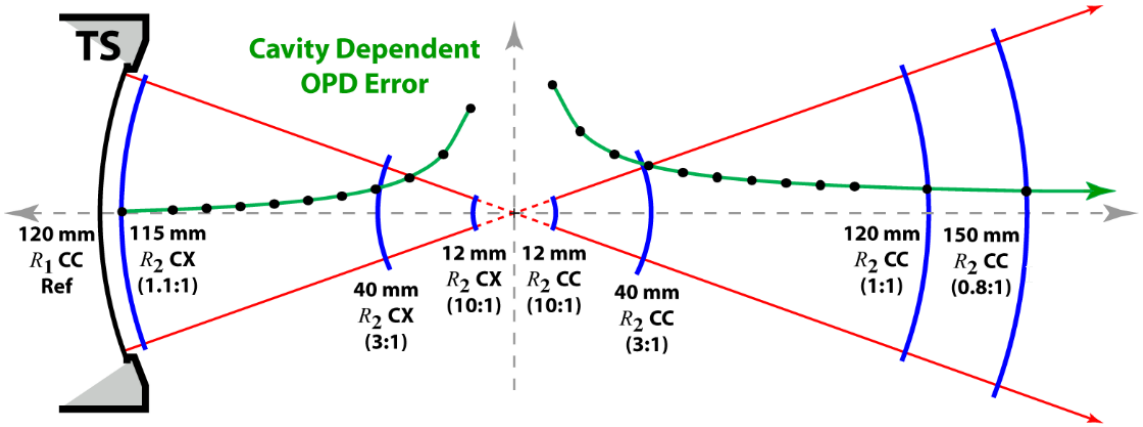

FIGURE 73: Simplified example of OPD errors as a non-linear function of cavity position for both convex and concave test parts [116]

Measuring a convex part follows the same rule as a concave part, but is further constrained by its ROC. Even if the f/# is slightly faster than the R/#, both foci of the TS and convex part may not align due to the convex part having a longer ROC than the focal length of the TS as seen in FIGURE 74 (a). Two solutions, one of which is shown in FIGURE 74 (b) is to increase the aperture of the TS while maintaining the same f/# so that the foci align. The alternative, a slower TS that yields a longer ROC, will provide a percentage of illumination (using the ratio R/# to f/#).

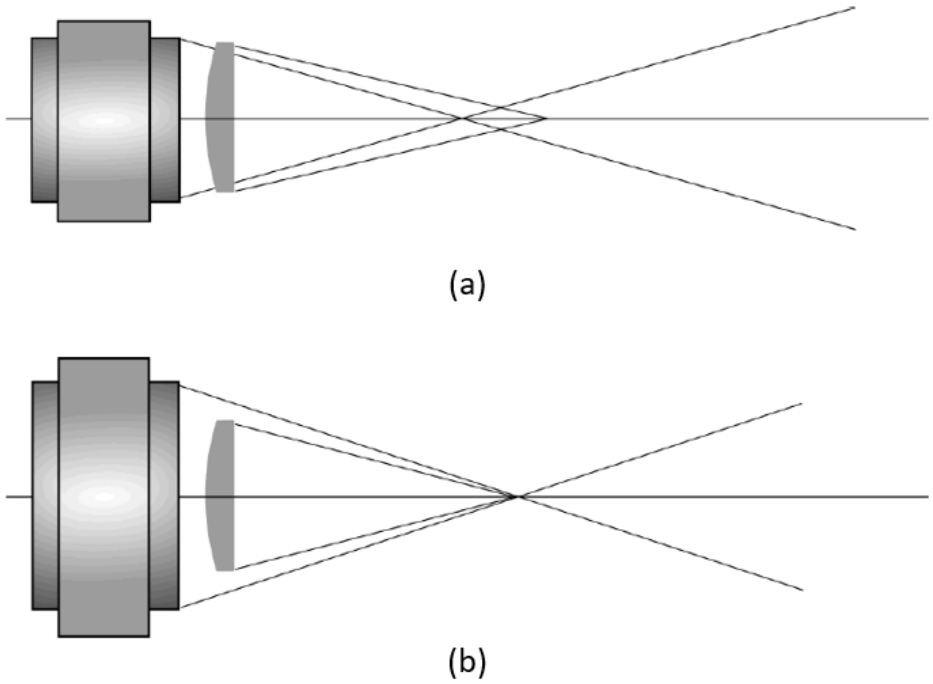

FIGURE 74: Faster TS than convex part where (a) both foci do not align and (b) both foci align and the convex part fits between the TS and its focal point [36]

Mild aspheres and freeforms can be measured with commercially available TSs and with appropriate correction for biases arising from varying slopes over the aperture [117]. Steeper sloped aspheres and freeforms require some form of a null optic (that also needs to be tested) where axially aligning the interferometric parts (especially with fast TSs) within the cavity should be done to limit defocus errors [118]. The steeper sloped the part, the more errors get introduced, sometimes at a quadratic rate or faster [119]. When a surface under test is not in focus, strong slope errors occur at the edge of the test part due to Fresnel diffraction [120]. Measuring, as mentioned above, an axially misaligned spherical optic using a TS adds spurious spherical aberration, which can be evaluated experimentally and compensated numerically [117], one common type of retrace error [121]. More generally, retrace error occurs when the wavefront reflected

from the TF or TS. This has been commonly been attributed to shearing the rays in the interferometer imaging system [107], [120], although the detailed design of those optics has a significant impact on the errors. A uniform tilt across the aperture can introduce coma, although at large tilts, other aberrations are observed (see Section 4.5.5). Retrace errors are minimized by minimizing aligning the test to minimize slopes [120]. As noted above, these errors can be calibrated and compensated computationally, limited by the uncertainty in the calibration results, nulling the fringes as much as possible.

4.2 Interferometry used with computer-generated holograms (CGH), a part specific null

CGH nulls, an alternative to null optics for testing steep aspheres in the early 70s [122], became commercially available increasing the dynamic range of the interferometers to measure freeform optics slightly over a decade ago [123], [124]. CGHs consist of a planar substrate, which has a diffractive microstructure produced by lithography [125]. The diffractive optical element converts the reference wavefront into a wavefront that matches the freeform optic under test producing a null, as shown in FIGURE 75.

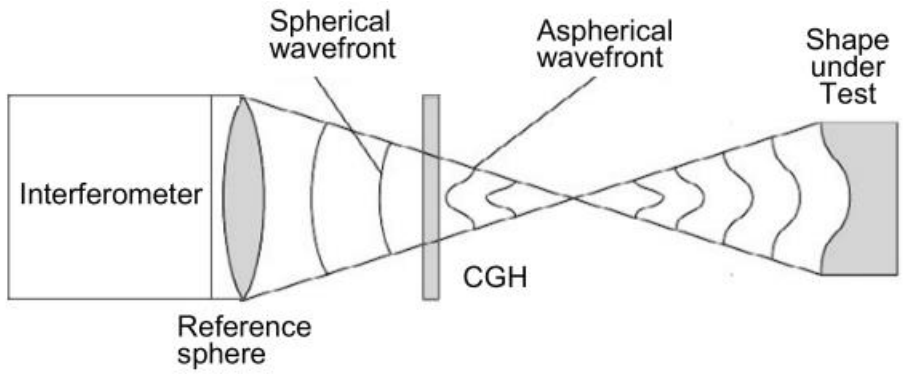

FIGURE 75: Simplified example of how a CGH works [126]

Any CGH null is fabricated for a specific part, which can be timely and expensive. A common placement for the CGH, shown in FIGURE 75, is advantageous since there are no modifications to the interferometer and the diverger lens doesn't need to be included in the raytracing for fabricating the CGH [127].

Sources of measurement errors come from misaligning CGHs in the interferometric cavity [128], [129] where alignment marks are made on the CGH for reproducibility. Other errors that affect the measurement are tolerancing of the CGH substrate and accuracy of the grating patterns [105], [128], [129]. Challenges also arise, one of which is appropriate clamping that is needed to avoid deformation of the CGH or freeform under test [130]. Another challenge is measuring large convex freeform optics when space is limited in the interferometric cavity because a CGH or null is also present within diverging focal length [131].

4.3 FOMCD of the Fizeau Verifire HD & AT interferometers with Transmission Flat (TF), exemplary level 3 data

If a reference flat (aka TF) is used to measure a plano optic in a Fizeau, then the system capability can easily be plotted on an FOMCD. (MATLAB code for Fizeau FOMCD is found in Appendix G). Systems are commercially available with apertures from 100 to 800 mm, with common intermediate apertures of 150, 300, 450, and 600 mm [132]. The Fizeau Verifire HD & AT interferometers, located in the Grigg 108 Lab, use a standard 100 mm TF, which represents λ_{max} in FIGURE 76. The AT has a common 1000 x 1000-pixel detector whereas the HD, a newer instrument, is larger, with a 2300 x 2300-pixel detector.

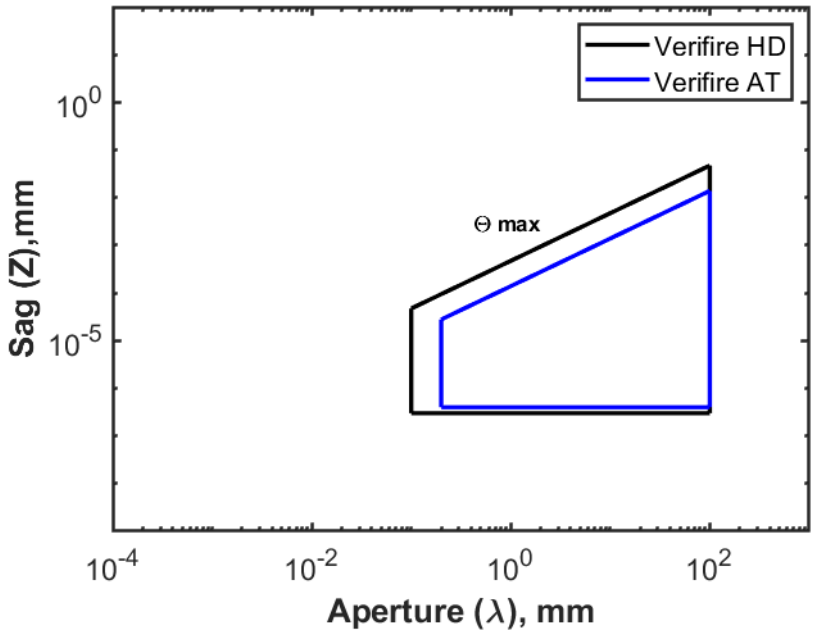

FIGURE 76: CD for the Fizeau Verifire HD & AT interferometers using a TF

TABLE 13: Numerical limits for Fizeau Verifire HD & AT interferometers CD

	Unit	**HD**	**AT**
$\boldsymbol{\theta_{max}}$	(deg)	0.17	0.05
$\boldsymbol{\lambda_{min}}$	(mm)	0.1	0.2
$\boldsymbol{\lambda_{max}}$	(mm)	100	100
$\boldsymbol{Z_{min}}$	(mm)	0.3e-6	0.4e-6
$\boldsymbol{Z_{max}}$	(mm)	0.4	0.3

Like the SWLI NexView, the lateral limit λ_{min} for the HD is also found and measured by the ITF. In FIGURE 77, Zygo had conducted and published the ITF calculations for the HD where it rolls off to Nyquist at nearly 100 µm [35]. Nyquist for the AT was found by calculating the spatial sampling or aperture of the TF divided by the number of pixels from the detector, which was approximately 200 µm.

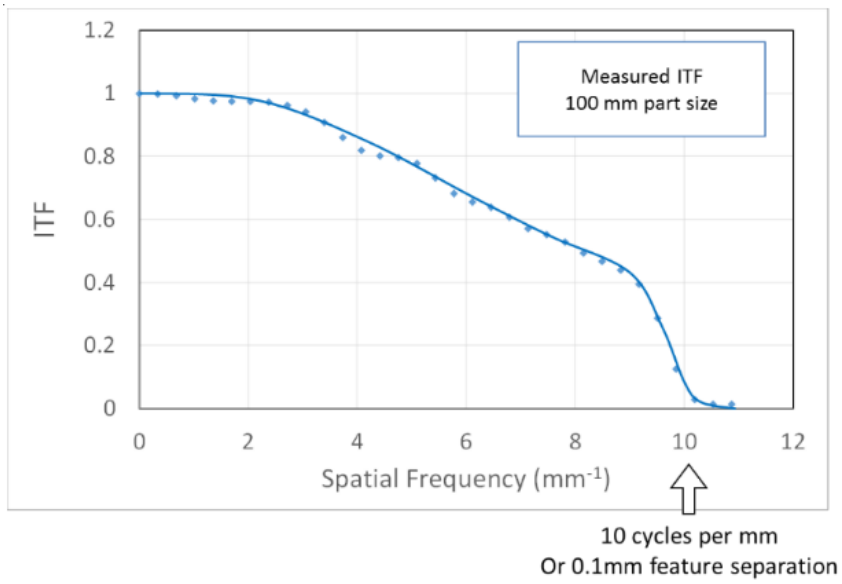

FIGURE 77: ITF for the Fizeau HD performed by Zygo [35]

Both Z_{min} values, a noise floor limit, come from the rms wavefront repeatability, which is "defined by the mean rms difference plus 2x the standard deviation for the differential between all even number measurements and a synthetic reference (an average of all odd measurements)" [20]. Z_{max}, or departure from the reference, is based on a HeNe illumination and found by dividing the maximum number of cycles or fringes across the aperture by number of pixels. According to experiments, the HD can fit 1000 fringes across a 100 mm aperture [35] and the AT 300 fringes[5]. Maximum slopes for both instruments were derived by using Nyquist, which allows the maximum departure that can be measured from a surface. Maximum tilt occurring across two pixels (one fringe) cannot be larger than one wave of OPD, which is half a wave of tilt. Hence, using trigonometry, the angle is calculated to find the maximum slope. Extending this limit may be possible; a base off-axis conic was fit to a mild freeform that resulted in reduced

[5] Based on experiments performed by C.J. Evans at UNCC

surface departures with no other null needed [133]. The maximum departure from the reference is limited where other complex diagrams, such as plotting slope as a function of aperture may be needed. This has been added to possible future work.

In FIGURE 76, the volume of the CD for the AT fits inside the CD for the HD demonstrating that the newer HD's capabilities have increased or improved.

4.4 Illumination diagram of the Fizeau Verifire HD or AT interferometer with TS, exemplary level 3 data

The TS's cone of light, represented by an illumination diagram, was developed since optical measurements cannot be described with a cartesian coordinate system or adapted to a CD (MATLAB code in Appendix H). Measuring a spherical optic such as an asphere or a freeform requires the use of a TS with a CGH. As mentioned in Section 1.4, some of the assumptions made when making an illumination diagram are: 1.) using a CGH with a mount that takes up 100 mm of spacing within the cavity and 2.) concave optics have an imposed physical limitation of 2 m for the table on which the interferometer sits. Otherwise, these illumination beam lengths would be constrained on the right side by the coherence length of the source and turbulence. TS are commercially available with collimated illumination beam apertures commonly found at 100 and 150 mm [134] for a broad range of f/#s.

The TSs at UNCC are the f/.75, f/1.5 and f/3.5 all 100 mm aperture, which were manufactured by OptiMax. The ROC for all three TS were estimated based on commercially available TSs [134], [135]. On the left side in FIGURE 78 are the TSs limited capability to measure convex parts. Making assumption #1 from above, the f/1.5 can measure apertures smaller than 80 mm with ROC less than 120 mm and the f/3.5 can

measure even smaller apertures up to 34 mm with ROC less than 122 mm. The illumination cone for the fast f/.75 is not visible as it would not be able to measure convex parts.

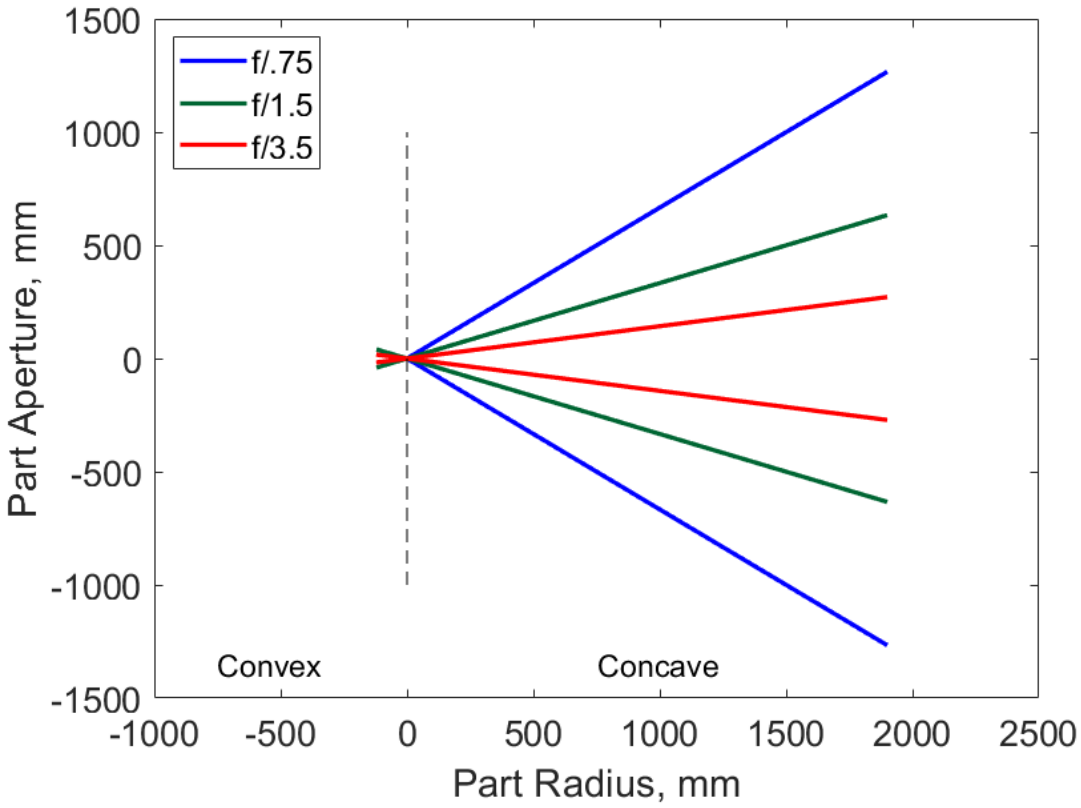

FIGURE 78: Illumination diagram for TSs at UNCC

The right side of FIGURE 78 is an illustration of fast TSs, f/.75 and f/1.5 and slow TS f/3.5 used to measure concave parts. Making assumptions #1 and 2, an f/.75 can measure up to a 2666 mm aperture concave freeform with a ROC of 1900 mm. An f/1.5, with same assumptions, can measure up to a 1266 mm aperture concave freeform with a ROC of 1900 mm as well. The slower f/3.5 TS has the ability to measure apertures up to

542 mm with a ROC of 1900 mm. The speed of the TS is directly proportional to the size of the illumination cone for measuring concave test parts.

4.5 Experiments primarily using the Fizeau HD with some comparisons to the Fizeau AT, a continuation of level 3 data

4.5.1 STR background and the 3 methods used

Please refer to Section 2.3.1 on explanation of STR and the 3 methods used.

4.5.2 STR experimental setup and procedure

The Verifire Fizeau HD is located in a temperature controlled (20C +/- 0.25C) lab in Grigg 108. For the STR setup using the Verifire HD, a transmission flat and reference flat were aligned with 7 cm (and 14 cm for next run) of spacing in the cavity as seen in FIGURE 79. 20 consecutive measurements were taken and piston, tip and tilt were removed in Mx. A mask was also applied trimming the edge due to roll off and then brought into MATLAB to calculate the standard deviation maps and STR values for each of the three methods. No further filtering was performed.

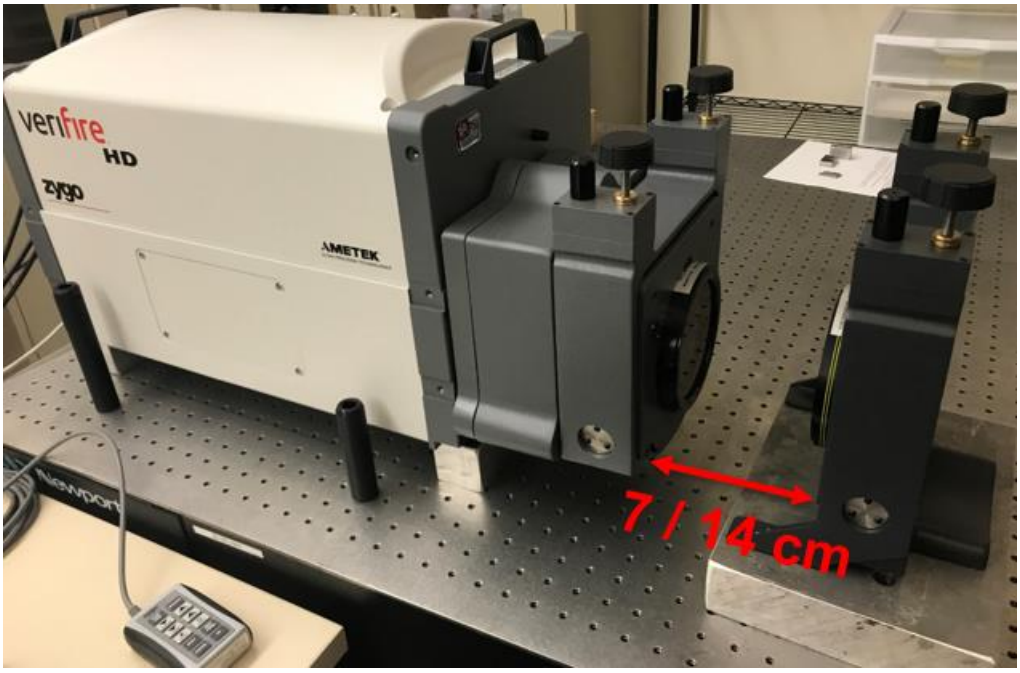

FIGURE 79: STR setup with the Verifire HD

4.5.3 STR results

The standard deviation map with the 7 cm spacing (FIGURE 80 (b)) has almost half the range of the standard deviation map with the 14 cm spacing (FIGURE 81 (b)). The 14 cm standard deviation map also shows more turbulence and thus slightly higher surface parameters, which is expected since the cavity length doubled.

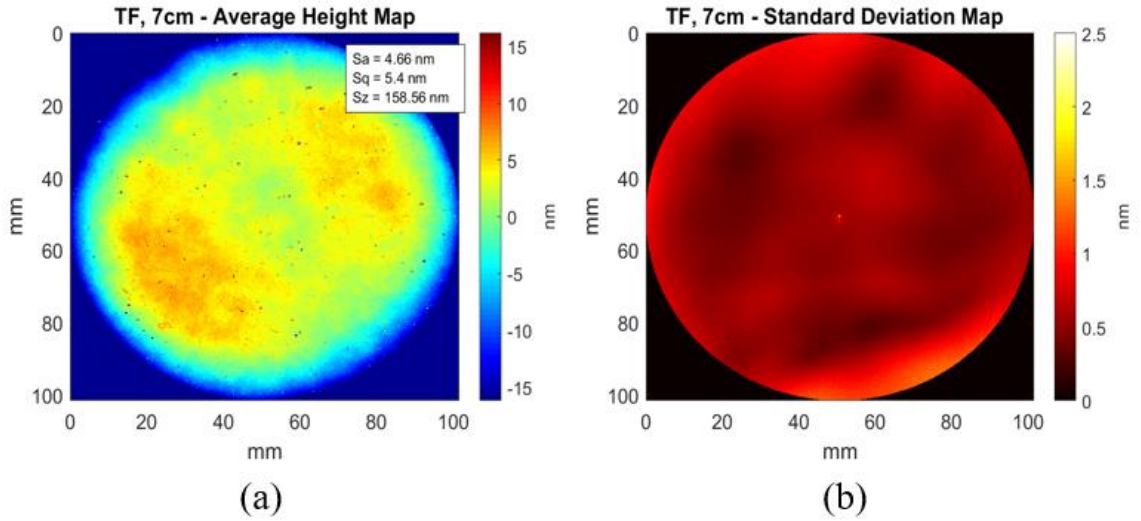

FIGURE 80: (a) Average height map and (b) standard deviation map for 7 cm spacing

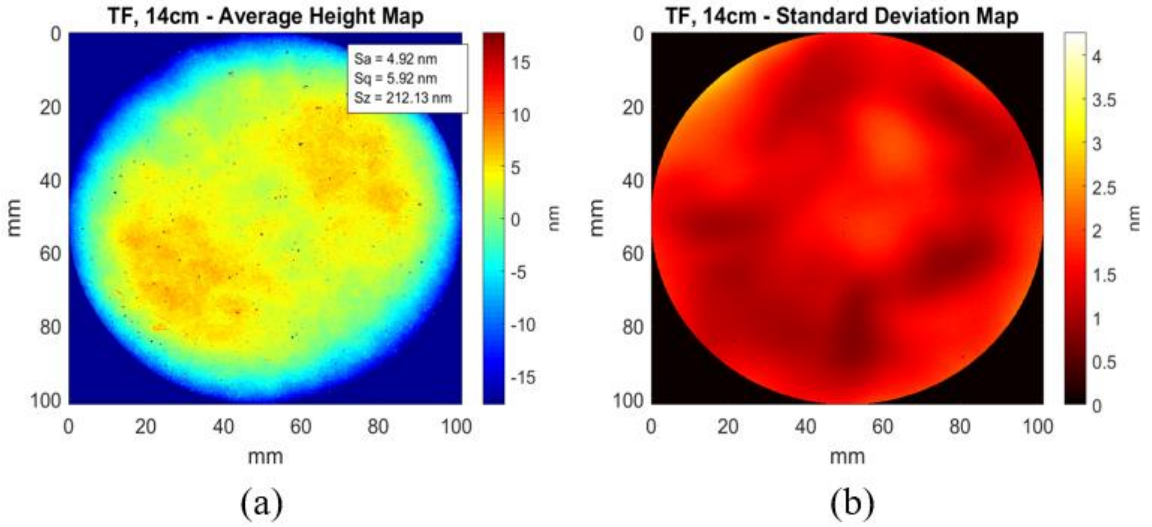

FIGURE 81: (a) Average height map and (b) standard deviation map for 14 cm spacing

Zygo, the manufacturer, states the RMS wavefront repeatability for the Fizeau HD is 0.35 nm [20]. Their method to obtaining this value is similar to the synthetic reference method (method 3), except that it doesn't use any of the measurements that are

subtracted in the average height map. This value is also more likely obtained with the shortest possible cavity length and therefore would result in a smaller STR value.

As shown in TABLE 14, the mean STR values for the three methods demonstrate repeatability for their cavity spacing, but the values of the 14 cm spacing are nearly double for each method. When the interferometric cavity increases, turbulence increases as well. In this case, doubling the size of the interferometric cavity nearly doubled the mean STR values.

TABLE 14: Mean STR values for Verifire HD

	7 cm	**14 cm**
Subtraction Method	0.63 nm	1.19 nm
Synthetic Reference	0.58 nm	1.22 nm
Standard Deviation Map	0.59 nm	1.45 nm

4.5.4 Retrace error experimental setup and procedure

The Verifire Fizeau HD is located in a temperature controlled (20C +/- 0.25C) lab in Grigg 108. The 100 mm TF was initially aligned to the optics in the interferometer followed by the reference flat to obtain a null reference measurement. There is a knob rotation for tilt in the +x – direction, as illustrated in FIGURE 82 where then a measurement is taken. These two steps were repeated until the surface “fell out” and could no longer be detected. These set of steps were then repeated for -x, +y and -y – directions.

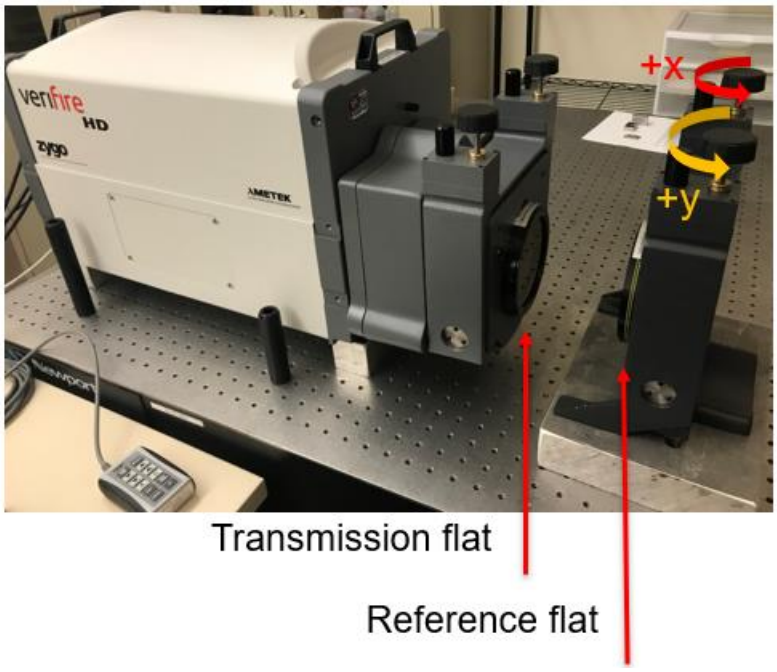

FIGURE 82: Retrace error setup with the Verifire HD

4.5.5 Retrace error results

The measurement data was brought into MATLAB removing piston and plotting Zernike coma versus Zernike tilt coefficients. Data from the previous Fizeau, the Verifire AT was also plotted to show a comparison to the new Fizeau as shown in FIGURE 83. The new Verifire HD has more than double the tilt capability of the previous Verifire AT, which induces less than a quarter coma. These lower retrace errors more than doubled the slope acceptance [108]; so the optics of the new Fizeau, either alone or in combination with updated software, have significantly improved from the previous Fizeau.

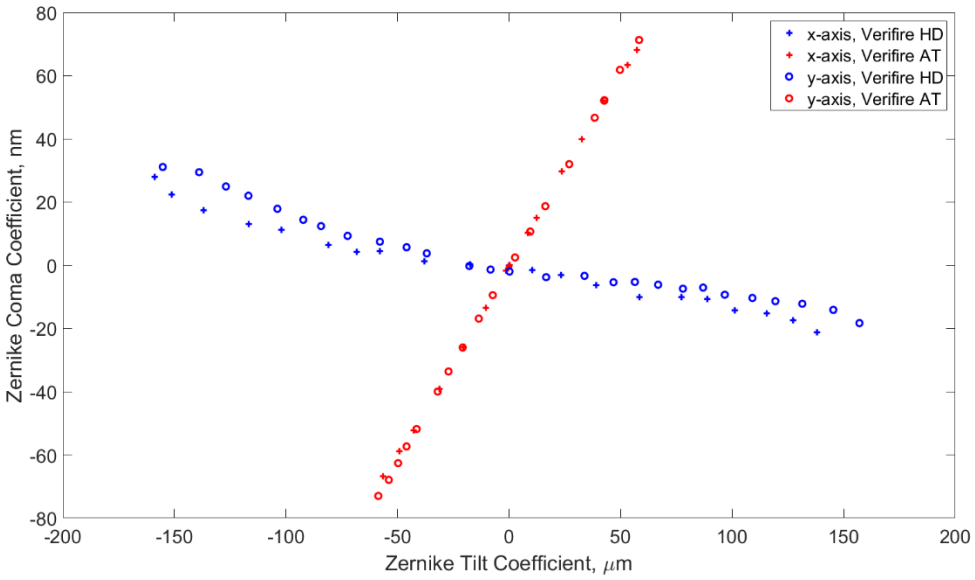

FIGURE 83: Coma as a function of tilt for Verifire HD and AT

The same procedure was also done with plotting Zernike astigmatism vs tilt coefficients as seen in FIGURE 84 for both Verifire HD and AT. The AT's shorter

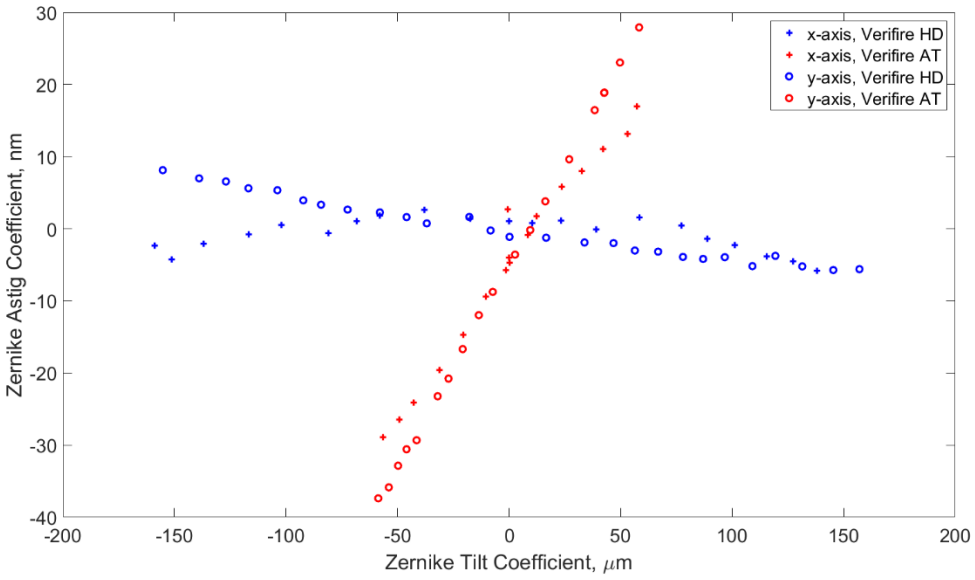

FIGURE 84: Astigmatism as a function of tilt for both Verifire HD & AT

range of tilt induces almost three times more astigmatism than the new HD, again demonstrating that internal optics of the system and/or the software has improved.

CHAPTER 5: CONCLUDING REMARKS AND SUGGESTIONS FOR FUTURE WORK

5.1 Concluding remarks

This project has been a collaboration with CeFO affiliates representing industry and government laboratories, including optics designers, fabricators, and system integrators. Data has been collected on 20 different metrology systems applicable to freeform optics metrology where the current format has been implemented into an 85-page document with navigable links, (that could also be realized as a web page). The hierarchical data structure is a suggested approach to enable optical designers, fabricators, and metrologists to identify early in the process if a part can be measured adequately and cost effectively using existing metrology instruments. Additional information is currently being acquired so it can be integrated into the document.

In this thesis, three (of many) metrology systems were discussed in Chapters 2 – 4 describing the development of their example data sets with first explaining the generic class of instruments (level 2) followed by an FOMCD and/or an illumination diagram (level 3). Chapter 2 focused on SWLIs, showing specific, previously unpublished, spatially correlated contributions to Type A uncertainty evaluation when measuring diamond turned surfaces. Chapter 3 concentrated on stylus profilometers, also with an approach to measuring diamond turned freeform optics. Detailed experiments focused on the consequences of the interaction of probes with the optical surfaces. Handbook values of yield stress ignored work hardening and possible metallurgical transformations in diamond turning of ductile metals. When probe radii of styli were similar to the tool nose radius, the resulting plastic deformation was surprising. Chapter 4 addressed the use of

Fizeau interferometry using both an FOMCD for transmission flats and an illumination diagram for transmission spheres where detailed experiments with Type A uncertainty and retrace errors were performed.

5.2 Future work

Experience data at times led to more unanswered questions. Here is a list of future work that may be considered:

- Currently there is ongoing testing of the RRF whose measurements will be integrated into the document alongside other level 3 experience data
- It was shown through experiments that the Metrology Lab is to specification (for climate control and environmental vibration control), but another test to confirm both the DMI and capacitance probe tests is to place accelerometers on the floor near the NexView and run the elevators while the NexView stage is on. More capacitance probe tests can be done after changing the pressure to the isolation table of the NexView and running the elevator to see where the ideal pounds per square inch (PSI) should be.
- Investigate bright spot in FIGURE 18 (b) by obtaining the pixel location and further filtering to figure out what may have caused the strange pattern. It would also be interesting to apply a narrow high pass filter to the corresponding height map in FIGURE 18 (a) to see what the surface would reveal.
- Consider models of other DT surfaces apart from DT NiP in Sections 2.4 and 2.5.
- Measure anisotropic surfaces with lay in 2 or more different directions. If the standard deviation map suggests it, perform a Monte Carlo analysis on the entire surface (instead of profile) now that a new workstation has been acquired.

- Further investigate what is causing this wave pattern in the average height map in FIGURE 22 (a) for the 2.75x.
- One source of error from the Hertzian stress calculations was that work hardening of the NiP during diamond turning was not taken into consideration; recent investigations suggest that some level of transformation from amorphous include intermetallic formation may be taking place. Further work in this area is required.
- Investigate the contact mechanics for the ruby traces on copper as to why plastic deformation looks as if there are 2 traces.
- Further analysis in crack propagation and fracture of BK 7 at 30 mN could be performed to understand why the trace groove depths and material built up above the surface varied significantly.
- The contact mechanics for interaction of spherical probes with diamond turned surfaces produced with tools of a similar radius need to be investigated.
- While rapid wear is not expected between diamond and the materials measured, deviations of the probe geometry from the nominal (either from manufacturing or prior use) could have affected the results in Chapter 3. One improvement would be to measure the stylus with a SWLI before and after each trace.
- The maximum departure from the reference is limited in the Fizeau CDs. It may be that another type of diagram is needed, such as plotting slope as a function of aperture.

REFERENCES

[1] K. P. Thompson and J. P. Rolland, “Freeform Optical Surfaces: A Revolution in Imaging Optical Design,” *Opt. Photonics News*, vol. 23, no. 6, p. 30, Jun. 2012.

[2] H. Pollicove and D. Golini, “Deterministic manufacturing processes for precision optical surfaces,” *Key Eng. Mater.*, vol. 238–239, no. September 2003, pp. 53–58, 2003.

[3] M. Schinhaerl *et al.*, “Advanced techniques for computer-controlled polishing,” *Curr. Dev. Lens Des. Opt. Eng. IX*, vol. 7060, no. July 2014, p. 70600Q, 2008.

[4] F. Z. Fang, X. D. Zhang, A. Weckenmann, G. X. Zhang, and C. Evans, “Manufacturing and measurement of freeform optics,” *CIRP Ann. - Manuf. Technol.*, vol. 62, no. 2, pp. 823–846, 2013.

[5] “ISO 10110-19:2015 Optics and photonics — Preparation of drawings for optical elements and systems — Part 19: General description of surfaces and components,” Geneva, 2015.

[6] K. Venditti *et al.*, “Design for metrology for freeform optics manufacturing,” *Procedia CIRP*, vol. 84, pp. 169–172, 2019.

[7] “Zygo NexView Specifications,” 2013.

[8] O. Profiler, “Zygo Zegage,” pp. 346–347, 2012.

[9] Mahr, “MarSurf LD 130 /LD 260. The step into a new dimension. The universal contour and surface measuring system as a compact measuring station.,” Göttingen, Germany.

[10] OptiPro, “OptiTrace 5000 Specifications.” [Online]. Available: https://www.optipro.com/optitrace5000-specs.html. [Accessed: 18-Jun-2018].

[11] Ametek, “Taylor Hobson PGI Matrix Spec sheet,” 2017.

[12] “Taylor Hobson Talysurf PGI Freeform Spec Sheet,” 2017.

[13] Panasonic, “Specifications for Ultrahigh Accurate 3-D Profilometer, UA3P-500H.” 2019.

[14] Panasonic, “UA3P Ultrahigh Accurate 3-D Profilometer.” 2018.

[15] P. Features, “PRISMO ® navigator HTG PRISMO ® navigator S-ACC PRISMO – The world ’ s leader in high-speed-Scanning,” 2008.

[16] Zeiss, “F25 Measuring Nanometers Spec Sheet.”

[17] Hexagon AB, “LEITZ PMM-F Product Brochure.” 2018.

[18] T. Noste, C. Evans, J. Miller, and L. Hopper, “Concurrent engineering of a next-generation freeform telescope: metrology and test,” no. May, p. 36, 2019.

[19] OptiPro, “UltraSurf ™ Non-Contact Metrology Systems - UltraSurf 5x 400.” .

[20] Zygo Corporation, “Zygo Fizeau Verifire HD Interferometer Specifications,” p. 8506, 2016.

[21] D. Xu, A. Garcia Coleto, B. Moon, J. Papa, michael Pomerantz, and J. Rolland, “Cascade optical coherence tomography (C-OCT),” *Opt. Express*, vol. 28, no. 14, pp. 19937–19953, 2020.

[22] J. D. Ellis, M. Tangari Larrategui, T. G. Brown, and Y. Zhang, “Calibration methods for a dual-wavelength interferometer system,” vol. 1074707, no. September 2018, p. 6, 2018.

[23] R. Chaudhuri, J. Papa, and J. P. Rolland, “System design of a single-shot reconfigurable null test using a spatial light modulator for freeform metrology,” *Opt. Lett.*, vol. 44, no. 8, p. 2000, 2019.

[24] A. M. Michalko and J. R. Fienup, “Verification of transverse translation diverse phase retrieval for concave optical metrology,” *Opt. Lett.*, vol. 43, no. 19, p. 4827, 2018.

[25] Phasics, “Phasics-SID4-HR.pdf.” .

[26] M. Stedman, “Basis for comparing the performance of surface-measuring machines,” *Precis. Eng.*, vol. 9, no. 3, pp. 149–152, Jul. 1987.

[27] A. Blum and C. Evans, “The history and future of the stedman diagram,” *Proc. - ASPE 2017 Spring Top. Meet. - Precis. Eng. Opt. What are Limits Precision, How to Charact. Them?*, pp. 26–31, 2017.

[28] K. H. Brenner and W. Singer, “Light propagation through,” *Appl. Opt.*, vol. 32, no. 26, pp. 4984–4988, 1993.

[29] “ISO 10110-12:2007 - Optics and photonics -- Preparation of drawings for optical elements and systems -- Part 12: Aspheric surfaces,” Geneva, 2007.

[30] P. de Groot and J. Disciacca, “Surface-height measurement noise in interference microscopy,” 2018.

[31] “ISO 25178-604:2013, Geometrical product specifications (GPS) — Surface texture: Areal — Part 604: Nominal characteristics of non-contact (coherence scanning interferometry) instruments,” Geneva, 2013.

[32] P. De Groot, X. C. De Lega, D. Sykora, and L. Deck, “The Meaning and Measure of Lateral Resolution for Surface Profiling Interferometers,” *Opt. Photonics News*, no. November 2014, 2012.

[33] “ISO 10360-2:2009, Geometrical product specifications (GPS) — Acceptance and reverification tests for coordinate measuring machines (CMM) — Part 2: CMMs used for measuring linear dimensions,” Geneva, 2009.

[34] Zeiss, “PRISMO Navigator Specifications,” no. May. Carl Zeiss Industrial Metrology LLC, 2013.

[35] L. L. Deck and P. J. De Groot, “Using the instrument transfer function to evaluate Fizeau interferometer performance,” *Opt. InfoBase Conf. Pap.*, vol. Part F56-O, p. 3, 2017.

[36] Zygo Corporation, “Transmission Sphere Selection.”

[37] D. Malacara, K. Creath, J. Schmit, and J. C. Wyant, “Testing of Aspheric Wavefronts and Surfaces,” in *Optical Shop Testing*, 3rd ed., D. Malacara, Ed. John Wiley & Sons, Inc, 2007, pp. 435–497.

[38] C. J. Evans and A. D. Davies, “Certification, self-calibration and uncertainty in optical surface testing,” *Int. J. Precis. Technol.*, vol. 3, no. 4, pp. 388–402, 2013.

[39] “ISO 10110-8:2010 - Optics and photonics -- Preparation of drawings for optical elements and systems -- Part 8: Surface texture; roughness and waviness,” Geneva, 2010.

[40] P. de Groot, “Coherence Scanning Interferometry,” *Opt. Meas. Surf. Topogr.*, pp. 187–208, 2011.

[41] P. J. de Groot and X. C. de Lega, “Interpreting interferometric height measurements using the instrument transfer function,” *Fringe 2005*, pp. 30–37, 2006.

[42] “ISO 25178-2: Geometrical product specifications (GPS) - Surface texture: Areal - Part 2: Terms, definitions and surface texture parameters.” 2012.

[43] L. He, C. J. Evans, and A. Davies, “Two-quadrant area structure function analysis for optical surface characterization,” *Opt. Express*, vol. 20, no. 21, p. 23275, Oct. 2012.

[44] Z. Hosseinimakarem, A. D. Davies, and C. J. Evans, “Zernike polynomials for mid-spatial frequency representation on optical surfaces,” in *Reflection, Scattering, and Diffraction from Surfaces V*, 2016.

[45] C. Hovis, H. Shahinian, and C. Evans, “Observations on the effect of retrace error in scanning white light interferometry of smooth optical surfaces,” no. January, p. OM4A.2, 2019.

[46] J. C. Wyant and J. Schmit, “Large field of view, high spatial resolution, surface measurements,” *Int. J. Mach. Tools Manuf.*, vol. 38, no. 5–6, pp. 691–698, 1998.

[47] P. Lonardy *et al.*, “Emerging Trends in Surface Metrology,” 2002.

[48] J. DiSciacca, R. Pultar, X. Colonna de Lega, and P. J. de Groot, “Interferometric measurements of mold-plate assemblies designed for high-volume manufacturing of aspheric microlenses,” vol. m, no. April, p. 24, 2020.

[49] J. H. Burge, P. Su, J. Yellowhair, and C. Zhao, “Optical surface measurements for very large flat mirrors,” *Adv. Opt. Mech. Technol. Telesc. Instrum.*, vol. 7018, p. 701817, 2008.

[50] W. T. Estler, K. L. Edmundson, G. N. I. Peggs, and D. H. Parker, “Large Scale Metrology - An update,” *CIRP Ann.*, vol. 3, no. 2, 2002.

[51] A. Efstathiou *et al.*, “A new swing-arm profilometer for metrology of large aspheric telescope optics,” *EIM Work.*, no. January, 2007.

[52] S. L. O’Dell *et al.*, “X-ray optics at NASA Marshall Space Flight Center,” *EUV X-ray Opt. Synerg. between Lab. Sp. IV*, vol. 9510, no. 256, p. 951003, 2015.

[53] P. de Groot, “Phase Shifting Interferometry,” in *Optical Measurement of Surface Topography*, Berlin, Heidelberg: Springer Berlin Heidelberg, 2011, pp. 167–186.

[54] J. S. Silfies, S. A. Schwartz, and M. W. Davidson, “The Diffraction Barrier in Optical Microscopy,” *Nikon Microscopy U*. [Online]. Available: https://www.microscopyu.com/techniques/super-resolution/the-diffraction-barrier-in-optical-microscopy. [Accessed: 22-Jun-2020].

[55] Zygo Corporation, “Nexview, Newview 8000, Zegage Series Objective Chart,” pp. 346–347, 2014.

[56] P. J. de Groot, “Principles of interference microscopy for the measurement of surface topography,” *Adv. Opt. Photonics*, vol. 5, no. 2, p. 131, 2013.

[57] “ISO 25178-600:2019(en), Geometrical product specifications (GPS) — Surface texture: Areal — Part 600: Metrological characteristics for areal topography measuring methods,” 2019. [Online]. Available: https://www.iso.org/obp/ui/#iso:std:iso:25178:-600:ed-1:v1:en. [Accessed: 05-Jun-2019].

[58] P. J. de Groot, “The Meaning and Measure of Vertical Resolution in Optical Surface Topography Measurement,” *Appl. Sci.*, vol. 7, no. 1, p. 6, 2017.

[59] P. De Groot and J. Disciacca, “Definition and evaluation of topography measurement noise in optical instruments Definition and evaluation of topography measurement noise in optical instruments,” *Opt. Eng.*, vol. 59, no. June, 2020.

[60] C. L. Giusca, R. K. Leach, and F. Helery, “Calibration of the scales of areal surface topography measuring instruments: Part 2. Amplification, linearity and squareness,” *Meas. Sci. Technol.*, 2012.

[61] SVS-VISTEK, “Tap balancing on CCD sensors.” [Online]. Available: https://www.svs-vistek.com/en/knowledgebase/svs-about-machine-vision.php?p=ccd-tap-balancing-959. [Accessed: 12-Dec-2019].

[62] D. J. Whitehouse, “The Properties of Random Surfaces of Significance in their Contact,” University of Leicester (United Kingdom), Ann Arbor, 1971.

[63] G. Rasigni, F. Varnier, M. Rasigni, and J. P. Palmari, “Spectral density function of the surface roughness for polished optical surfaces,” vol. 73, no. 10, pp. 5–9, 1983.

[64] E. L. Church, T. V. Vorburger, and J. C. Wyant, “Direct Comparison Of Mechanical And Optical Measurements Of The Finish Of Precision Machined Optical Surfaces,” *Prod. Asp. Single Point Mach. Opt.*, vol. 0508, no. May, p. 71, 1984.

[65] E. L. Church and P. Z. Takacs, “Optimal estimation of finish parameters,” *Opt. Scatt. Appl. Meas. Theory*, vol. 1530, no. May, pp. 71–85, 1991.

[66] J. M. Elson and J. M. Bennett, “Calculation of the power spectral density from surface profile data,” *Appl. Opt.*, vol. 34, no. 1, p. 201, 1995.

[67] E. Herman, R. Youngworth, and D. Aikens, “Modern optics drawings: the journey from MIL to ANSI to ISO drawing formats,” no. September, p. 27, 2018.

[68] H. Aryan, C. J. Evans, and T. J. Suleski, “On the use of ISO 10110-8 for specification of optical surfaces with mid-spatial frequency errors,” *Opt. InfoBase Conf. Pap.*, vol. Part F56-O, no. c, pp. 2–4, 2017.

[69] J. K. Lawson, C. R. Wolfe, K. R. Manes, J. B. Trenholme, D. M. Aikens, and R. E. English, Jr., “Specification of optical components using the power spectral density function,” *Opt. Manuf. Test.*, vol. 2536, no. May, pp. 38–50, 1995.

[70] T. Hull, M. J. Riso, J. M. Barentine, and A. Magruder, “Mid-spatial frequency matters: examples of the control of the power spectral density and what that means to the performance of imaging systems,” *Infrared Technol. Appl. XXXVIII*, vol. 8353, no. May, pp. 835329-835329–17, 2012.

[71] J. E. Harvey and A. K. Thompson, “Scattering effects from residual optical fabrication errors,” *Int. Conf. Opt. Fabr. Test.*, vol. 2576, no. May, pp. 155–174, 1995.

[72] V. G. Badami and P. J. De Groot, “Displacement measuring interferometry,” *Handb. Opt. Dimens. …*, 2013.

[73] P. J. De Groot, “A review of selected topics in interferometric optical metrology,” *Reports Prog. Phys.*, vol. 82, no. 5, p. ab092d, 2019.

[74] Engineering Toolbox, “Coefficients of Linear Thermal Expansion,” 2003. [Online]. Available: https://www.engineeringtoolbox.com/linear-expansion-coefficients-d_95.html. [Accessed: 06-Jan-2020].

[75] T. R. Thomas, *Rough Surfaces*, 2nd Ed. Imperial College Press, 1999.

[76] R. E. Reason, “Surface finish and its measurement,” *J. Inst. Prod. Eng.*, vol. 23, no. 10, p. 347, 1944.

[77] T. V. Vorburger, E. C. Teague, F. E. Scire, and F. . Rosberry, “Measurements of Stylus Radii,” in *Wear*, 1979, pp. 39–49.

[78] R. K. Leach, “The measurement of surface texture using stylus instruments.,” *Meas. Good Pract. Guid. No. 37*, no. 2, p. 100, 2001.

[79] J. M. Bennett and J. H. Dancy, “Stylus profiling instrument for measuring statistical properties of smooth optical surfaces.”

[80] T. V Vorburger, T. B. Renegar, A. X. Zheng, J. Song, J. A. Soons, and R. M. Silver, “NIST SURFACE ROUGHNESS AND STEP HEIGHT CALIBRATIONS , Measurement Conditions and Sources of Uncertainty,” pp. 1–9, 2009.

[81] J. F. Song and T. V. Vorburger, “Stylus profiling at high resolution and low force,” *Appl. Opt.*, vol. 30, no. 1, p. 42, Jan. 1991.

[82] International Organization for Standardization, “ISO 25178-701: Geometrical product specifications (GPS) — Surface texture: Areal — Part 701: Calibration and measurement standards for contact (stylus) instruments.” Geneva, 2010.

[83] C. L. Giusca, R. K. Leach, F. Helary, T. Gutauskas, and L. Nimishakavi, “Calibration of the scales of areal surface topography-measuring instruments: Part 1. Measurement noise and residual flatness,” *Meas. Sci. Technol.*, 2012.

[84] H. Haitjema and M. A. A. Morel, “Noise bias removal in profile measurements,” *Meas. J. Int. Meas. Confed.*, vol. 38, no. 1, pp. 21–29, 2005.

[85] P. J. de Groot and J. DiSciacca, “Surface-height measurement noise in interference microscopy,” in *Proceedings of the Society of Photo-Optical Instrumentation Engineers*, 2018, no. August, p. 26.

[86] R. Leach and H. Haitjema, “Bandwidth characteristics and comparisons of surface texture measuring instruments,” *Meas. Sci. Technol.*, vol. 21, no. 3, 2010.

[87] International Organization for Standardization, “ISO 25178-3: Geometrical product specifications (GPS) - Surface texture: Areal - Part 3: Specification operators.” 2012.

[88] D. J. Whitehouse and W. L. Wang, “Dynamics and trackability of stylus systems,” 1996.

[89] D. J. Whitehouse, *Handbook of surface and nanometrology, second edition*. CRC Press Taylor & Francis Group, 2002.

[90] D. J. Whitehouse, “Stylus damage prevention index,” *Mech. Eng. Sci.*, vol. 214, no. 7, pp. 975–980, 2000.

[91] G. Schuetz, “Surface Texture From Ra To Rz - Mahr Metrology.” [Online]. Available: https://www.mahr.com/en/Services/Production-metrology/Know-how/Gaging-Tips/Surface-Measurement-Gaging-Tips/?ContentID=19020&Overview=0. [Accessed: 10-Jul-2018].

[92] T. R. Thomas, “Commercial Applications of Precision Manufacturing at the Sub-Micron Level,” in *Proceedings of SPIE*, 1992, vol. 1573, no. April 1992, pp. 188–200.

[93] R. Leach and S. Smith, *Basics of Precision Engineering*. CRC Press Taylor & Francis Group, 2018.

[94] B. R. Lawn, “Indentation of Ceramics with Spheres: A Century after Hertz,” *J. Am. Ceram. Soc.*, vol. 81, no. 8, pp. 1977–1994, Jan. 2005.

[95] T. Fritz, H. S. Cho, K. J. Hemker, W. Mokwa, and U. Schnakenberg, “Characterization of electroplated nickel.”

[96] “Material Properties of Copper - PVD or Electroplated.” [Online]. Available: http://www.mit.edu/~6.777/matprops/copper.htm. [Accessed: 18-Jan-2018].

[97] R. Rhorer and C. Evans, “Fabrication of optics by diamond turning,” *Handb. Opt.*, pp. 41.1-41.13, 1995.

[98] “Uninhibited Naval brass, UNS C46400.” [Online]. Available: http://www.matweb.com/search/datasheet.aspx?matguid=5d0f88a052c54ee28c7e66de6d7f0d92. [Accessed: 18-Nov-2018].

[99] “BK7 Optical material | Ultiquest Technology.” [Online]. Available: http://www.ultiquestcom.com/products/optics/optical-glass-nbk7-b270-and-others.html. [Accessed: 05-Aug-2018].

[100] J. C. Wyant, B. F. Oreb, and P. Hariharan, “Testing aspherics using two-wavelength holography: use of digital electronic techniques,” *Appl. Opt.*, vol. 23, no. 22, p. 4020, 1984.

[101] E. Garbusi, C. Pruss, and W. Osten, “Interferometer for precise and flexible asphere testing,” *Opt. Lett.*, vol. 33, no. 24, p. 2973, 2008.

[102] G. Baer, J. Schindler, C. Pruss, J. Siepmann, and W. Osten, “Calibration of a non-null test interferometer for the measurement of aspheres and free-form surfaces,” *Opt. Express*, vol. 22, no. 25, p. 31200, 2014.

[103] R. Beisswanger, C. Pruss, C. Schober, A. Harsch, and W. Osten, “Tilted wave interferometer in common path configuration: challenges and realization,” no. June 2019, p. 51, 2019.

[104] A. Offner, “Null tests using compensators,” in *Optical Shop Testing*, 2nd ed., D. Malacara, Ed. John Wiley & Sons, 1992, pp. 427–454.

[105] J. C. Wyant and V. P. Bennett, “Using Computer Generated Holograms to Test Aspheric Wavefronts,” *Appl. Opt.*, vol. 11, no. 12, p. 2833, 1972.

[106] S. M. Arnold, “How To Test An Asphere With A Computer Generated Hologram,” *Hologr. Opt. Opt. Comput. Gener.*, vol. 1052, no. May 1989, p. 191, 1989.

[107] L. L. Deck and C. Evans, “High performance Fizeau and scanning white-light interferometers for mid-spatial frequency optical testing of free-form optics,” *Adv. Metrol. X-Ray EUV Opt.*, vol. 5921, no. August 2005, 2005.

[108] D. M. Sykora and P. de Groot, “Instantaneous measurement Fizeau interferometer with high spatial resolution,” *Opt. Manuf. Test. IX*, vol. 8126, no. Figure 1, p. 812610, 2011.

[109] J. Schmit, K. Creath, and J. C. Wyant, “Surface Profilers, Multiple Wavelength, and White Light Interferometry,” in *Optical Shop Testing*, 3rd ed., Malacar, Ed. John Wiley & Sons, Inc, 2007, pp. 667–742.

[110] L. L. Deck, “Fourier-transform phase-shifting interferometry,” *Opt. Soc. Am.*, vol. 42, no. 13, pp. 2354–2365, 2003.

[111] J. Millerd, N. Brock, J. Hayes, M. North-Morris, B. Kimbrough, and J. C. Wyant, “Pixelated Phase-Mask Dynamic Interferometers,” in *Fringe 2005*, W. Osten, Ed. Springer, 2005, pp. 640–647.

[112] M. Takeda, “Spatial-carrier fringe-pattern analysis and its applications to precision interferometry and profilometry: An overview,” *Ind. Metrol.*, vol. 1, no. 2, pp. 79–99, 1990.

[113] P. Hariharan, “Interferometers,” *Springer Ser. Opt. Sci.*, vol. 184, pp. 183–217, 2014.

[114] W. T. Estler, “High accuracy displacement interferometry in air,” *Appl. Opt.*, vol. 24, no. 6, p. 808, 1985.

[115] N. Bobroff, “Residual errors in laser interferometry from air turbulence and nonlinearity,” *Appl. Opt.*, vol. 26, no. 13, p. 2676, 1987.

[116] D. M. Sykora, “A model for cavity induced errors with wavefront slope in high accuracy spherical Fizeau metrology,” *Opt. InfoBase Conf. Pap.*, pp. 1–3, 2008.

[117] C. J. Evans and J. B. Bryan, “Compensation for Errors Introduced by Nonzero Fringe Densities in Phase-Measuring Interferometers,” *CIRP Ann.*, vol. 42, no. 1, pp. 577–580, Jan. 1993.

[118] P. De Groot, T. Dresel, and B. Truax, “Axial alignment for high-precision interferometric measurements of steeply-curved spheres,” *Surf. Topogr. Metrol. Prop.*, vol. 3, no. 4, p. 44004, 2015.

[119] H. Schreiber and J. H. Bruning, “Phase Shifting Interferometry,” in *Optical Shop Testing*, 3rd ed., D. Malacara, Ed. John Wiley & Sons, Inc, 2007.

[120] H. Schreiber and J. H. Bruning, “Phase Shifting Interferometry,” in *In: Malacara 3rd ed. Optical Shop Testing*, John Wiley & Sons, 2007, pp. 547–655.

[121] C. B. Kreischer, “Retrace error: interferometry’s dark little secret,” 2013, vol. 8884.

[122] A. J. MacGovern and J. C. Wyant, “Computer generated holograms for testing optical elements,” *Opt. Soc. Am.*, vol. 10, pp. 619–624, 1971.

[123] Diffraction International, “CGH Nulls,” 2018. [Online]. Available: https://www.diffraction.com/cgh_nulls.php. [Accessed: 29-May-2019].

[124] S. M. Arnold, “Design and Analysis of Diffractive Aspheric Nulls,” in *Proc. of the ASPE Winter Top. Meeting, North Carolina, USA*, 2004.

[125] J. Flugge, K. Wendt, H. Danzebrink, and A. Abou-zeid, “Optical Methods for Dimensional Metrology in Production Engineering,” *CIRP Ann. - Manuf. Technol.*, vol. 51, no. 2, pp. 685–699, 2002.

[126] E. Savio, L. De Chiffre, and R. Schmitt, “Metrology of freeform shaped parts,” *CIRP Ann. - Manuf. Technol.*, vol. 56, no. 2, pp. 810–835, 2007.

[127] J. H. Burge and J. C. Wyant, “Use of computer generated holograms for testing aspheric optics,” *Free. Opt. Des. Fabr. Metrol. Assem.*, 2004.

[128] R. Schreiner, T. Herrmann, J. Röder, S. Müller-Pfieffer, and O. Falkenstörfer, “Design considerations for computer generated holograms as supplement to Fizeau interferometers,” *Opt. Fabr. Testing, Metrol. II*, vol. 5965, no. October 2005, p. 59650K, 2005.

[129] S. Reichelt, C. Pruss, and H. J. Tiziani, “Absolute interferometric test of aspheres by use of twin computer-generated holograms,” *Appl. Opt.*, vol. 42, no. 22, p. 4468, 2003.

[130] C. Schindler, T. Köhler, and E. Roth, “Freeform Optics: current challenges for future serial production,” vol. 1044802, no. October 2017, p. 25, 2017.

[131] J. H. Burge, “Fizeau interferometry for large convex surfaces,” vol. 2536, 1995.

[132] Zygo Corporation, “Transmission Flats.” [Online]. Available: https://www.zygo.com/?/met/interferometers/accessories/transmissionflats/. [Accessed: 19-Jun-2020].

[133] N. Takaki, J. C. Papa, A. Bauer, and J. P. Rolland, “Off-axis conics as base surfaces for freeform optics enable null testability,” *Opt. Express*, vol. 28, no. 8, p. 10859, 2020.

[134] Diffraction International, “Fizeau Transmission Sphere Selector.” [Online]. Available: https://www.diffraction.com/Fizeau_spheres.php. [Accessed: 05-May-2019].

[135] Zygo Corporation, “Transmission Sphere Specifications,” 2010.

APPENDIX A: MATLAB CODE FOR THE NEXVIEW FOMCD

```
%CD for UNCC NV objectives: 2.75x, 10x, 20x, 50x
close all; clear all;clc;

[top_line,bottom_line,left_line,right_line,lambda,lambda_min_line,lambda_max_line] =
NV2pt75x_fxn;

figure
X1 = loglog(lambda, top_line, 'k','Linewidth', 2);
hold on
loglog(lambda, bottom_line, 'k','Linewidth', 2);
loglog(lambda_min_line, left_line, 'k','Linewidth', 2);
loglog(lambda_max_line, right_line, 'k','Linewidth', 2);

%%
[top_line,bottom_line,left_line,right_line,lambda,lambda_min_line,lambda_max_line] =
NV10x_fxn;

X2 = loglog(lambda, top_line, 'b','Linewidth', 2);
hold on
loglog(lambda, bottom_line, 'b','Linewidth', 2);
loglog(lambda_min_line, left_line, 'b','Linewidth', 2);
loglog(lambda_max_line, right_line, 'b','Linewidth', 2);
text((10^-2),(10^-2),'\Theta max','Color','k','FontWeight','Bold','HorizontalAlignment',
'center')

%%
[top_line,bottom_line,left_line,right_line,lambda,lambda_min_line,lambda_max_line] =
NV20x_fxn;

X3 = loglog(lambda, top_line, 'r','Linewidth', 2);
hold on
loglog(lambda, bottom_line, 'r','Linewidth', 2);
loglog(lambda_min_line, left_line, 'r','Linewidth', 2);
loglog(lambda_max_line, right_line, 'r','Linewidth', 2);

%%
[top_line,bottom_line,left_line,right_line,lambda,lambda_min_line,lambda_max_line] =
NV50x_fxn;

X4 = loglog(lambda, top_line, 'g','Linewidth', 2);
hold on
loglog(lambda, bottom_line, 'g','Linewidth', 2);
loglog(lambda_min_line, left_line, 'g','Linewidth', 2);
```

```
loglog(lambda_max_line, right_line, 'g','Linewidth', 2);

 %Nice to see where the lines are
xlim([10e-5 10e2])
ylim([10e-10 10e-1])

xlabel('Aperture (\lambda), mm','FontWeight','Bold');
ylabel('Sag (Z),mm', 'FontWeight','Bold');
set(gca,'Linewidth', 1.5);
ax = gca;
ax.FontSize = 14;

legend([(X1),(X2),(X3), (X4)],{'2.75x','10x','20x','50x'},'Location','northeast');

%%functions for 2.75x, 10x, 20x and 50x

function[top_line,bottom_line,left_line,right_line,lambda,lambda_min_line,lambda_max
_line,z_min] = NV2pt75x_fxn

 %All units in mm
%NexView using 2.75x Objective
%lambda min: 2*2.93um = .00586 mm- Nyquist limit
%lambda max: 3 mm FOV
%zmax (max PV): 150 um = .150 mm the max scan length, but has extended scan
%2e4
%zmin (min PV): 1.2e-4 um = 1.2e-7 mm axial accuracy (could this be axial res of 5
nm?)
%slope limit: 3.71 deg

%Stedman diagram values
lambda_min = (.00586);  %incl nyquist sampling (or limit)
lambda_max = 3;    %lambda max
z_min = (1.2*10^-7);     %Zmin
z_max = .150;        %Rp
theta_max = 3.71*(pi/180); %steepest slope that can be meas, probe flank angle
b = 0*(pi/180);       %slope error of angle, put 0 for unknown
n= 1000;          %number of points for the lines

lambda = exp(linspace( log(lambda_min), log(lambda_max), n)); %lambdamin to max w
log spacing (x-values)
slope_line = (theta_max*lambda/(2*pi));
z_max_line = zeros(1,n) + z_max;    %add vector of zeros to make z_max a vector (y-
values)
z_min_line = zeros(1,n) + z_min;    %add vector of zeros to make z_min a vector (y-
values)
```

```
lambda_min_line = zeros(1,n) + lambda_min; %add vector of zeros to make lambda_min
a vector (x-values)
lambda_max_line = zeros(1,n) + lambda_max; %add vector of zeros to make
lambda_max a vector (x-values)
slope_err_line = (b*lambda/(2*pi));

top_line  = min([z_max_line;slope_line]); %curvature_line; took out
bottom_line = max([z_min_line; slope_err_line]);
left_line = linspace(bottom_line(1), top_line(1),n); %starts@ 1st element in vector
bottom_line to 1st elem in top_line
right_line = linspace(bottom_line(end), top_line(end),n);
 end

function[top_line,bottom_line,left_line,right_line,lambda,lambda_min_line,lambda_max
_line] = NV10x_fxn;

%All units in mm
%NexView using 10x Objective
%lambda min: 2*0.82um = .00164 mm- Nyquist limit
%lambda max: .83 mm FOV
%zmax (max PV): 150 um = .150 mm the max scan length, but has extended scan
%2e4
%zmin (min PV): 1.2e-4 um = 1.2e-7 mm axial accuracy (could this be axial res of 5
nm?)
%slope limit: 14.53 deg

%Stedman diagram values
lambda_min = (.00164);  %incl nyquist sampling (or limit)
lambda_max = 1.5;    %lambda max
z_min = (1.2*10^-7);     %Zmin
z_max = .150;         %Rp
theta_max = 14.53*(pi/180); %steepest slope that can be meas, probe flank angle
b = 0*(pi/180);       %slope error of angle, put 0 for unknown
n= 1000;          %number of points for the lines

lambda = exp(linspace( log(lambda_min), log(lambda_max), n)); %lambdamin to max w
log spacing (x-values)
slope_line = (theta_max*lambda/(2*pi));
z_max_line = zeros(1,n) + z_max;    %add vector of zeros to make z_max a vector (y-
values)
z_min_line = zeros(1,n) + z_min;    %add vector of zeros to make z_min a vector (y-
values)
lambda_min_line = zeros(1,n) + lambda_min; %add vector of zeros to make lambda_min
a vector (x-values)
lambda_max_line = zeros(1,n) + lambda_max; %add vector of zeros to make
lambda_max a vector (x-values)
```

```
slope_err_line = (b*lambda/(2*pi));

top_line  = min([z_max_line;slope_line]); %curvature_line; took out
bottom_line = max([z_min_line; slope_err_line]);
left_line = linspace(bottom_line(1), top_line(1),n); %starts@ 1st element in vector
bottom_line to 1st elem in top_line
right_line = linspace(bottom_line(end), top_line(end),n);
 end

function[top_line,bottom_line,left_line,right_line,lambda,lambda_min_line,lambda_max
_line] = NV20x_fxn

%All units in mm
%NexView using 20x Objective
%lambda min: 2*.41um= .82um = .00082 mm - Nyquist limit
%lambda max: .42 mm FOV
%zmax (max PV): 150 um = .150 mm the max scan length, but has extended scan
%2e4
%zmin (min PV): 1.2e-4 um = 1.2e-7 mm axial accuracy (could this be axial res of 5
nm?)
%slope limit: 21.80 deg

%Stedman diagram values
lambda_min = (.00082);  %incl nyquist sampling (or limit)
lambda_max = .42;    %lambda max
z_min = (1.2*10^-7);     %Zmin
z_max = .150;         %Rp
theta_max = 21.80*(pi/180); %steepest slope that can be meas, probe flank angle
b = 0*(pi/180);       %slope error of angle, put 0 for unknown
n= 1000;          %number of points for the lines

lambda = exp(linspace( log(lambda_min), log(lambda_max), n)); %lambdamin to max w
log spacing (x-values)
slope_line = (theta_max*lambda/(2*pi));
z_max_line = zeros(1,n) + z_max;    %add vector of zeros to make z_max a vector (y-
values)
z_min_line = zeros(1,n) + z_min;    %add vector of zeros to make z_min a vector (y-
values)
lambda_min_line = zeros(1,n) + lambda_min; %add vector of zeros to make lambda_min
a vector (x-values)
lambda_max_line = zeros(1,n) + lambda_max; %add vector of zeros to make
lambda_max a vector (x-values)
slope_err_line = (b*lambda/(2*pi));

top_line  = min([z_max_line;slope_line]); %curvature_line; took out
bottom_line = max([z_min_line; slope_err_line]);
```

```
left_line = linspace(bottom_line(1), top_line(1),n); %starts@ 1st element in vector
bottom_line to 1st elem in top_line
right_line = linspace(bottom_line(end), top_line(end),n);
end

function[top_line,bottom_line,left_line,right_line,lambda,lambda_min_line,lambda_max
_line] = NV50x_fxn;

%All units in mm
%NexView using 50x Objective
%lambda min: .52um = .00052 mm  %optical res considering sparrow criteria
%lambda max: .17 mm FOV
%zmax (max PV): 150 um = .150 mm the max scan length, but has extended scan
%2e4
%zmin (min PV): 1.2e-4 um = 1.2e-7 mm axial accuracy (could this be axial res of 5
nm?)
%slope limit: 28.13 deg

%Stedman diagram values
lambda_min = (.00052);  %incl nyquist sampling (or limit)
lambda_max = 0.17;    %lambda max
z_min = (1.2*10^-7);     %Zmin
z_max = .150;         %Rp
theta_max = 28.13*(pi/180); %steepest slope that can be meas, probe flank angle
b = 0*(pi/180);       %slope error of angle, put 0 for unknown
n= 1000;          %number of points for the lines

lambda = exp(linspace( log(lambda_min), log(lambda_max), n)); %lambdamin to max w
log spacing (x-values)
slope_line = (theta_max*lambda/(2*pi));
z_max_line = zeros(1,n) + z_max;    %add vector of zeros to make z_max a vector (y-
values)
z_min_line = zeros(1,n) + z_min;    %add vector of zeros to make z_min a vector (y-
values)
lambda_min_line = zeros(1,n) + lambda_min; %add vector of zeros to make lambda_min
a vector (x-values)
lambda_max_line = zeros(1,n) + lambda_max; %add vector of zeros to make
lambda_max a vector (x-values)
slope_err_line = (b*lambda/(2*pi));

top_line  = min([z_max_line;slope_line]); %curvature_line; took out
bottom_line = max([z_min_line; slope_err_line]);
left_line = linspace(bottom_line(1), top_line(1),n); %starts@ 1st element in vector
bottom_line to 1st elem in top_line
right_line = linspace(bottom_line(end), top_line(end),n);
end
```

APPENDIX B: MATLAB CODE FOR ALL 3 STR METHODS

```
%3 STR METHODS.
%Written by Kristen Venditti, last edited 10/1/2019
%Method1 fxn - Type A uncertainties, average height and std dev map (de Groot & Evans)
%Method2 fxn - ISO 25178-604 finds rms difference of two layers and divides by sqrt2
%Method3 fxn - More robust way of ISO 25178, finds the average through the stack, takes difference of the avg from each interferogram (msmt) and then finds the rms, which
%rms values are plotted
%Code can be used for glass optics with no NaNs

%% You must change fname & pr
close all; clear all; clc;

%% Change only these parameters (addpath, objective, optictype, pr, fname)
directory = uigetdir;  %opens dialog box that displays folder & returns path that user selects
cd(directory);  %change to directory folder
%adds this path (where STR code is stored) so that it can be referenced
addpath 'C:\Users\Kristen\Documents\Grad School\CeFO 20\A2_FOMCD_Instrument Specs\Experiments for Inteferometers\Matlab code\SWLI'

objective = 2.75  ;            %enter objective # here
optictype = sprintf('NiP');  %'NiP' or 'FS' or  'SiC'
pr = 3 ;                  %change the FOV to '.42'for 20x, '.17'for 50x, '3'for 2.75x
fname = 'NV275x_30um';       %change file name here only
npix = 1024;                %#of pixels

filename1 = sprintf('HM_%s',fname);              %height map png
filename2 = sprintf('Hist_AHM_%s',fname); %hist of AHmap
filename3 = sprintf('SD_b4outliers_%s',fname);    %Std dev map png
filename4 = sprintf('Hist_SD_beforeOutliers_%s',fname);
filename5 = sprintf('SD_afterOutliers_%s',fname); %Std dev map png
filename6 = sprintf('Hist_SD_afterOutliers_%s', fname);  %Hist SDM after outliers
filename7 = sprintf('ISO25178_%s', fname);        %ISO method png
filename8 = sprintf('M3_%s', fname);              %method 3 png

 set(0,'DefaultAxesFontSize', 14);       %sets all grapsh to 14 font

%%
n = 20;            %enter # of measurements that you're analyzing
for k = 1:n
  filename = sprintf('%s_%d.dat',fname,k); %prints fname for %s and k for %d
  a = ReadZygoBinary(filename)*10^9; %stores data from 1 file in a 1024x1024 matrix
```

```
    [b,count(k)] = piston_2d(a); %removes piston from 3D matrix
    [n1, n2] = size(b); %returns the # of n1 rows & n2 columns when b is a matrix
    x = 1:n1;
    y = 1:n2;
    [X, Y] = meshgrid(x,y);     %creates the grid coordinates in x&y to prepare surface
    tip_tilt = interpol(X,Y,b); %tilt fxn
    B{k} = b - tip_tilt(X,Y);   %removes tilt
end

%% When running MC Sim, comment out rest
% [ profile   ] = profile_extraction(B); %used to extract a profile for
%MonteCarlo Profile simulation

% [ alldata , d ] = MonteCarloSim(B);
% B = alldata;
%
% [rot_hm, rot_hm1, res_hm] = STR_rotation_fxn(B);
% B = res_hm;

[avg, sd, sd2, hm_Sa, hm_Sq, hm_rms, hm_Sz, hm_Sz2, pxx, pctile] =
STR_method1_2d_nan_fxn(B);     %fxn to get avg hm and std of all layers

figure %(figure 1)
xya = (0:npix)*(pr/npix);   %changes pixel to resolution (spatial sampling)
imagesc(xya,xya,avg);
c=colorbar;
colormap('jet');
ylabel(c,'nm')
title([optictype, ' - Average Height Map,  ', num2str(objective) 'x' ]);
Sa = hm_Sa;
Sq = hm_Sq;
Sz = hm_Sz;
Sz2 = hm_Sz2;
dim = [.6 .4 .5 .5]; %[x y w h] where xy is, doesn't make sense though, trial & error
s1 = ['Sa = ' num2str(round(Sa,2)) ' nm']; %build string of string, variable, string
s2 = ['Sq = ' num2str(round(Sq,2)) ' nm']; %same as above
s3 = ['Sz = ' num2str(round(Sz2,2)) ' nm'];
stri = {s1, s2, s3}; %a cell array
annotation('textbox', dim, 'String',stri,'BackgroundColor','w','FitBoxToText','on');
xlabel('mm');
ylabel('mm');
saveas(gca, fullfile(directory, filename1),'png'); %saves png in file folder

figure %(figure 2) histogram of avg HM
nbins = 100;
h=histogram(avg,nbins);
```

```
title([optictype ' - Hist. of AHM, ' num2str(objective) 'x']);
%ylabel(
saveas(gca, fullfile(directory, filename2),'png'); %saves png in file folder

figure %(figure3) plots the sd map before outliers are removed
xya = (0:npix)*(pr/npix);  %change pixel to resolution (spatial sampling)
imagesc(xya,xya,sd); c=colorbar; colormap('hot'); ylabel(c,'nm');
title([optictype, ' - Standard Deviation Map,  ', num2str(objective) 'x' ]);
xlabel('mm');
ylabel('mm');
mean_sdmap = nanmean(nanmean(sd));
saveas(gca, fullfile(directory, filename3),'png');

figure %(figure 4);
nbins = 100;
h=histogram(sd,nbins); %histogram of SD map before removing outliers
title([optictype,' - SDM, ', num2str(objective) 'x']);
saveas(gca, fullfile(directory, filename4),'png');

figure %(figure 5) plots sd map after outliers are removed
xya = (0:npix)*(pr/npix);  %change pixel to resolution (spatial sampling)
imagesc(xya,xya,sd2); c=colorbar; colormap('hot'); ylabel(c,'nm');
title([optictype, ' - Standard Deviation Map,  ', num2str(objective) 'x' ]);
xlabel('mm');
ylabel('mm');
mean_sdmap = nanmean(nanmean(sd));
outli = sum(sum(isnan(sd2))); %# of NaNs removed (outliers)
dim = [.6 .4 .5 .5]; %[x y w h]
s4 = ['Outliers = ' num2str(outli)]; %build string of string then variable
stri = {s4};
annotation('textbox', dim, 'String',stri,'BackgroundColor','w','FitBoxToText','on');
saveas(gca, fullfile(directory, filename5),'png');

figure %(figure 6);
nbins = 100;
h=histogram(sd2,nbins); %histogram of SD map removing outliers
title([optictype,' - SDM Outliers Removed, ', num2str(objective) 'x']);
saveas(gca, fullfile(directory, filename6),'png');

[msmts rtmsq] = STR_method2_2d_nan_fxn(B);      %function to get rms/sqrt(2) for
every 2 measurments

 figure; %(figure7)
 plot([1:msmts],(rtmsq),'*');              %plots all values from STR_meth2_rms
 title([optictype, ' - ISO 25178 Method, ', num2str(objective) 'x' ])
 xlabel('Measurement differences');
```

```
 ylabel('Rms divided by square root (nm)');
 avgrms2 = nanmean(rtmsq);
 std2 = std(rtmsq);
 dim = [.6 .4 .5 .5]; %[x y w h] where xy is, doesn't make sense though, trial & error
 s5 = ['Avg rms = ' num2str(round(avgrms2,2)) ' nm']; %build string of string then
variable
 stri = {s5};
 annotation('textbox', dim, 'String',stri,'BackgroundColor','w','FitBoxToText','on');
 saveas(gca, fullfile(directory, filename7),'png');

[rtmsq, n2]= STR_method3_2d_nan_fxn(B);      %function to calc the rms difference

figure; %(figure8)
plot([1:n2],(rtmsq),'*');
title([optictype, ' - RMS of Avg - Msmt, ',num2str(objective) 'x'])
xlabel('Measurement');
ylabel('Rms (nm)');
avgrms3 = nanmean(rtmsq);
s6 = ['Avg rms = ' num2str(round(avgrms3,2)) ' nm']; %build string of string then
variable
stri = {s6};
annotation('textbox', dim, 'String',stri,'BackgroundColor','w','FitBoxToText','on');
%saveas(gca, fullfile(directory, filename8),'png');

filename = 'workspace_variables.mat';
save(filename)

%these are the following function where each fxn is an STR method followed by
%functions for removing piston and tilt

% this fxn calculates the average value of each
% layer, saves the avg value in matrix "avg", calculates
% the stdev and plots the stdev

function [avg, sd, sd2, hm_Sa, hm_Sq, hm_rms, hm_Sz, hm_Sz2, pxx, pctile] =
STR_method1_2d_nan_fxn(a)                  %call avg and stdev

[n1 n2]=size(a);                  %n1=not used, n2=#layers,finding size of matrix: 1x20
[n3 n4] = size(a{1});              %size of measurement: 1024x1024

avg = zeros(n3,n4); %creates a place holder for output matrix, all zeros
sd = zeros(n3,n4);
pctile = 75;    %change percentile to make all values > pctile value to be nans

sum = 0;
alldata = [];       %initialize empty vector
```

```
for i = 1:n3
   for j = 1:n4
      for k = 1:n2
         msd_vector(k) = a{k}(i,j); %vector of n measurements (down the stack),…
                        %so this loop will get all the layers for that pixel
                        %but will only show last msmt pixel
       end
      alldata = [alldata,msd_vector]; %appends "msd_vector" to the end of "alldata"
vector
      avg(i,j) = nanmean(msd_vector); %takes mean of stack ignorning nans to get an avg
      sd(i,j) = nanstd(msd_vector);   %takes std of stack ignoring nans to get std map
   end
end
   %pxx value can change
   pxx = prctile(alldata,pctile); %gives percentile value from "alldata" values
   sd2 = sd;
   %replacing any value greater than  w/ a nan, this is to plot this sd2 graph for visual
purposes
   sd2(sd2 > pxx) = NaN;

%% These are the Surface Parameters for Average Height Map before removing outliers
   hm_Sa = nanmean(nanmean(abs(avg))); %Sa value of avg height map
   hm_Sq = std(alldata);  %Sq, take std of each pixel in stack to get one std for all pixels
in HM
   hm_rms = rms(rms(avg));  %Sq, take rms of stack to get one rms at each pixel & then
rms of all pixels in map
   max_Sp = abs(max(max(alldata))); %Sp value of all data for avg HM
   min_Sv = abs(min(min(alldata))); %Sv value of all data for avg HM
   hm_Sz = max_Sp - min_Sv; %Sz or PV value of all data for avg HM

   hm_Sz2 = peak2peak(alldata);
 %% These are the Sa for Avg HM after removing outliers
%
   avg(avg < -3*hm_Sq | avg > 3*hm_Sq) = NaN; %replacing values outside of +-3*rms
w/ ...
% %                                    %nan to get rid of outliers & make scales similar
%    hm_Sa2 = nanmean(nanmean(abs(avg)));      %Sa 2 after removing outliers
 %    hm_rms2 = nanstd(nanstd(avg));    %rms of new avg HM
%
%    %alldata(alldata < -3*hm_Sq | avg > 3*hm_Sq) = NaN;
%    max_Sp2 = abs(max(max(avg))); %Sp value of all data for avg HM
%    min_Sv2 = abs(min(min(avg))); %Sv value of all data for avg HM
%    hm_Sz2 = max_Sp - min_Sv; %Sz or PV value of all data for avg HM
   End

%Subtraction method: a fxn finds rms difference of two layers and divides by sqrt2
```

```
%the result is a measurement noise Sq and in this case there will be 10
%samples

function [msmts rtmsq] = STR_method2_2d_nan_fxn(B)
[n1 n2] = size(B);
msmts = n2/2;           %#of msmts used (10 in this case)
% p = floor(o);          %#of differences of layers
for k = 1:2:n2            %will run 10x in this case for 20 msmts
   dif =  B{k} - B{k+1};
   rootmeansq = rms(rms(dif),'omitnan');        %rms of each difference vector
   rtmsq(k) = rootmeansq/sqrt(2); %sqrt for every 2 layers storing each ans
%     k = k+2;
end
 rtmsq(2:2:end) = [ ];
%   method 3 fxn aka "subtraction technique" finds the average through the stack, takes
difference of the
%avg of all measurements' matrices from each measurment and finds the rms.
%rms values are plotted

function [rtmsq, n2] = STR_method3_2d_nan_fxn(a)

[n1 n2] = size(a);  %size 1x20
[n3 n4] = size(a{1}); %1024x1024

for i = 1:n3
   for j = 1:n4
      for k = 1:n2
         msd_vector(k) = a{k}(i,j);
      end
      avg(i,j) = nanmean(msd_vector);
   end
end

for k = 1:n2
   dif = a{k} - avg;
   rtmsq(k) = rms(rms(dif),'omitnan');
end

%fxn removes piston from 3-d matrix

function [b, count] = piston_2d(a)
npix = 1024;           %#pixels
c = 0;
count = 0;
B =isnan(a);          %identifies Nans by returning in array w 1-NaN, 0-not a NaN
for i = 1:npix
```

```
    for j = 1:npix
        if B(i,j) == 0      %if not a NaN set = 0 in array B
            c = c + a(i,j);   %then sum all points on 1 map
            count = count + 1;  %then count all #s (not a NaN)
        end
    end
end
avg = c/count;
for i = 1:npix
    for j = 1:npix
        b(i,j) = a(i,j) - avg;  %avg is subtracted fr ea pt in map
    end
end
end

%remove tilt

function [fi, gi] = interpol(X,Y,b)

[Xi, Yi, Zi] = prepareSurfaceData(X,Y,b); %transform data for surface fitting w the fit
fxn
[fi,gi] = fit([Xi, Yi], Zi, 'poly11'); %fit polynomial surface of deg 1 in x&y(calc tip/tilt)
end
```

APPENDIX C: MATLAB CODE FOR CREATING PSD PLOTS

```
%Analyze PSDs wrt STR for surfaces and objectives for avg x
clc; clear all; close all;
 %add path & folder – where to find & pull data from computer
addpath 'C:\Users\Kristen\Documents\Grad School\CeFO 20\A2_FOMCD_Instrument
Specs\Experiments for Inteferometers\Measurements\NexView\PSD plots';
folder = 'C:\Users\Kristen\Documents\Grad School\CeFO 20\A2_FOMCD_Instrument
Specs\Experiments for Inteferometers\Measurements\NexView\PSD plots';

set(0,'DefaultAxesFontSize', 14);       %sets all graphs to 14 font

ob1 = readtable('avgx_R1_FS_275x.csv');
ob2 = readtable('avgx_R1_FS_20x.csv');
ob3 = readtable('avgx_R1_FS_50x.csv');

figure()
loglog(ob1.X, ob1.Y, '*')
hold on
loglog(ob2.X, ob2.Y, '+')
loglog(ob3.X, ob3.Y, 's')
title('R1 Fused Silica Avgx')
xlabel('Spatial Frequency (1/mm)')
ylabel('Power Density (nm^3)')
legend('2.75x', '20x', '50x')
% savefig('R1_FS_Avgx');
```

APPENDIX D: MATLAB CODE AFTER EXTRACTING A PROFILE AND COMPUTING THE MONTE CARLO SIMULATION

```
%8/12/19 Kristen Venditti
%these profiles were taken from DT interferogram phase map using 20x
%objective with 512th row vector for 1st msmt using profile_extraction code
%420/1024 = .400 um/pixel
%there were 1024 pixels increased to by factor of fd40 = 40960 pixels for x-axis
%x-axis: 420um/40960pixel = .01 um/pixel --> 10 nm/scaled pixel
%y-axis: nm height data

clear all; clc; close all;

pfactor = 40; %factor by which to increase profile vector, 40x1024 = 40960
N = 200; %number of profiles

load('profile.mat')

interp_prof = interp(profile{1},pfactor); %increases profile vector by a factor of "pfactor"
i.e. 40
nan_prof1 = NaN(1,4);  %create a 1x4 vector or NaNs
cat_prof{1} = [nan_prof1 , interp_prof , nan_prof1]; %concatenates all 3 vectors &
replaces 1st profile into the 1st cell of cell array


for i = 2:N                         %0:8 = +/-40, 0:10 = +/-50, 0:12 = +/-60 etc
    d = abs(round((rand - 0.5)*24)); %0:10, d = delta that moves certain amt pixels
(elements)where rand is uniformly distr...
                                %interval b/t (0,1)
      beg_nan = NaN(1, 12-d);   %makes 1st vector of NaNs for beg of array
      end_nan = NaN(1, d);      %makes 2nd vector of Nans for end of array
      cat_prof{i} = [beg_nan , interp_prof , end_nan ];    %concatenates profile with nans
in beginning and end of vector
end

n1 = size(cat_prof{1},2);   %gets size of the 2nd term (40968) of profile (1x40968)
for i = 1:n1
       for k = 1:N
          stack_el(k) = cat_prof{k}(i); %gets each element through stack
       end
   sd(i) = std(stack_el,'omitnan');      %performs std dev on ea element in stack
   sd1(i) = std(stack_el,'includenan');  %same as above but includes nans
end

figure  %plot of profile interpolated by a factor
```

```
plot(interp_prof);
xlabel('Subpixel')
ylabel('nm')
title('Profile')

figure  %plot sd using points
plot(sd, '.');
xlabel('Subpixel')
ylabel('nm')
title('SD Map of Profile')

figure   %plot using lines
plot(sd);
xlabel('Subpixel')
ylabel('nm')
title('SD Map of Profile Subpixel level')

sd_d = decimate(sd,40);
figure
plot(sd_d)
xlabel('Pixel')
ylabel('nm')
title('MC Sim. SD Profile')

%% Same profile as above, but taken from the SD Map
load('SDprof.mat')
figure
plot(ans, '.');

figure  %plot comes from a profile taken after STR SD map was done
plot(ans);
xlabel('Pixel')
ylabel('nm')
title('STR SD Profile')
```

APPENDIX E: LABVIEW BLOCK DIAGRAM FOR DATA ACQUISITION OF THE CAPACITANCE PROBE TESTING

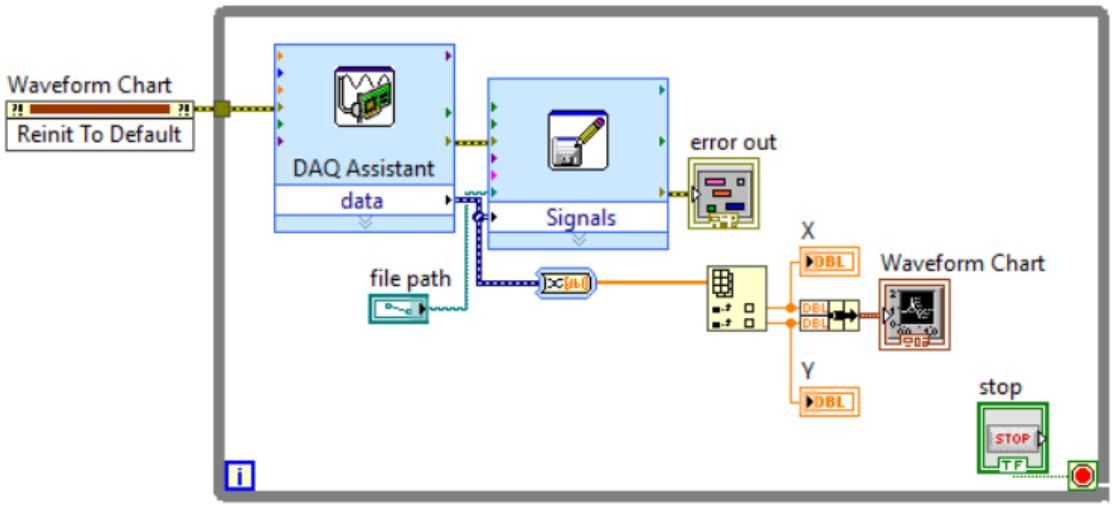

APPENDIX F: MATLAB CODE FOR CAPACITANCE PROBE DATA

```
close all; clear all; clc;
%folder to look through
addpath('C:\Users\Kristen\Documents\Grad School\CeFO 20\A2_FOMCD_Instrument
Specs\Experiments for Inteferometers\NexView MTM Data\CP_Testing\New DAQ
data\Data analysis for stage on and off')

load('x_disp_stageON_raw.mat')
data{1} = x_disp;
load('y_disp_stageON_raw')
data{2} = y_disp;
% load('x_disp_stageOFF_raw.mat')
% data{3} = x_disp;
% load('y_disp_stageOFF_raw.mat')
% data{4} = y_disp;

set(0, 'DefaultAxesFontSize', 16)

%creating vector for x-axis of same size as cap probe data
time_vector = [0:1:size(x_disp,1)-1];
%converting x-axis vector (samples) to seconds (by dividing by sample rate) and then by
60 sec to get mins
time = time_vector/1000/60;

figure
for i = 1:2

   plot(time, data{1,i}) %, colors(i)
   hold on
 end

xlabel('time, (min)')
ylabel('Displacement, (um)')
[~,hobj, ~,~]= legend('x - stage on','y - stage on','Location','northwest');  %'x - stage off','y
- stage off',
hl = findobj(hobj,'type','line');
set(hl,'LineWidth',1.5);
ht = findobj(hobj,'type','text');
set(ht,'FontSize',12);
hold off
 %% Filter & offset
 figure
for i = 1:2
   %filter each data set as it goes through loop
```

```
    data_filt{i} = smoothdata(data{1,i},'gaussian',3);

    %find offset from filtered data
    offset = data_filt{1,i}(1);
    %remove the offset from filt data and save all values in array
    offs_filt{i} = data_filt{1,i} - offset;
    plot(time, offs_filt{1,i})
    hold on
end

xlabel('time, (m)')
ylabel('Displacement filtered, (um)')
[~,hobj, ~,~]= legend('x - stage on','y - stage on','Location','northwest');  %'x - stage off','y
- stage off',
hl = findobj(hobj,'type','line');
set(hl,'LineWidth',1.5);
ht = findobj(hobj,'type','text');
set(ht,'FontSize',12);

figure
plot(time, offs_filt{1,1});
xlabel('time, (m)')
ylabel('x Displacement filtered, (um)')

figure
plot(time, offs_filt{1,2}, 'r');
xlabel('time, (m)')
ylabel('y Displacement filtered, (um)')
```

APPENDIX F: MATLAB CODE FOR THE HERTZIAN STRESSES OF THE MAHR PROFILOMETER STYLI

```
%plots Hertzian stresses calculated from Mathcad and read from Excel
close all; clear all; clc;

[num,txt,raw] = xlsread('LoadVsHzStress');
set(0,'DefaultAxesFontSize', 14);       %sets all graphs to 14 font
PLoad = num(1:end, 1);      %loads 1-30 mN
% ymins = [1.181E10,5.799E8,2.143E8,9.454E9];   %for reference, or loop ;)
% ymaxs = [2.019E10,8.002E9,3.664E8,1.617E10];
% titles = ['Electro-deposited Nickel','Naval brass 464','Copper','BK7'];
x = cat(1,0,PLoad);         %vector of x-values from PLoad, but starting with 0
y = ones(size(x));          %vector of 1's of correct length to multiply by min & max later
NiP_2dia = num(1:end, 2);    %Dia Stylus 2 um
NiP_500r = num(1:end, 3);    %Ruby Stylus 500 um
NB_2dia = num(1:end, 4);    %Dia Stylus 2 um
NB_500r = num(1:end, 5);    %Ruby Stylus 500 um
Cu_2dia = num(1:end, 6);    %Dia Stylus 2 um
Cu_500r = num(1:end, 7);    %Ruby Stylus 500 um
BK_2dia = num(1:end, 8);    %Dia Stylus 2 um
BK_500r = num(1:end, 9);    %Ruby Stylus 500 um

%% Electro-deposited NiP
figure
plot(PLoad, NiP_2dia, 'd', 'MarkerFaceColor', 'b', 'MarkerEdgeColor', 'b', 'MarkerSize', 6)
hold on
plot(PLoad, NiP_500r, 's', 'MarkerFaceColor', '[0.77,0.08,0.20]', 'MarkerEdgeColor',
'[0.77,0.08,0.20]','MarkerSize', 6)
yline(995,'-','Theoretical YS NiP','LineWidth',2);
ymin = 1.181E4*y;       %multiply vector of 1's by min & max
ymax = 2.019E4*y;
YS_x = [x;flip(x)];     %create vectors of values going forward, then backward for area
fill
YS_y = [ymax;fliplr(ymin)];
YS_area = fill(YS_x,YS_y,'k','edgecolor','none');   %fill in area with color, remove edges
set(YS_area,'facealpha',.2)     %set transparency
set(gca, 'YScale', 'log')
xlabel('Load (mN)')
ylabel('Hertzian Stress (MPa)')
title('Hertzian Stresses for Electrodeposited NiP')
legend('2 um diamond', '500 um ruby', 'Location', 'Northwest')

%% Naval Brass 464
figure
```

```
plot(PLoad, NB_2dia, 'd', 'MarkerFaceColor', 'b', 'MarkerEdgeColor', 'b', 'MarkerSize', 6)
hold on
plot(PLoad, NB_500r, 's', 'MarkerFaceColor', '[0.77,0.08,0.20]', 'MarkerEdgeColor',
'[0.77,0.08,0.20]','MarkerSize', 6)
yline(455,'-','Theoretical YS NiP','LineWidth',2);
ymin = 5.799E2*y;       %multiply vector of 1's by min & max
ymax = 8.002E3*y;
YS_x = [x;flip(x)];     %create vectors of values going forward, then backward for area
fill
YS_y = [ymax;fliplr(ymin)];
YS_area = fill(YS_x,YS_y,'k','edgecolor','none');   %fill in area with color, remove edges
set(YS_area,'facealpha',.2)     %set transparency
set(gca, 'YScale', 'log')
xlabel('Load (mN)')
ylabel('Hertzian Stress (MPa)')
title('Hertzian Stresses for Naval Brass 464')
legend('2 um diamond', '500 um ruby', 'Location', 'Northwest')

%% Copper
figure
plot(PLoad, Cu_2dia, 'd', 'MarkerFaceColor', 'b', 'MarkerEdgeColor', 'b', 'MarkerSize', 6)
hold on
plot(PLoad, Cu_500r, 's', 'MarkerFaceColor', '[0.77,0.08,0.20]', 'MarkerEdgeColor',
'[0.77,0.08,0.20]','MarkerSize', 6)
yline(300,'-','Theoretical YS NiP','LineWidth',2);
ymin = 2.143E2*y;       %multiply vector of 1's by min & max
ymax = 3.664E2*y;
YS_x = [x;flip(x)];     %create vectors of values going forward, then backward for area
fill
YS_y = [ymax;fliplr(ymin)];
YS_area = fill(YS_x,YS_y,'k','edgecolor','none');   %fill in area with color, remove edges
set(YS_area,'facealpha',.2)     %set transparency
set(gca, 'YScale', 'log')
xlabel('Load (mN)')
ylabel('Hertzian Stress (MPa)')
title('Hertzian Stresses for Copper')
legend('2 um diamond', '500 um ruby', 'Location', 'Northwest')

%% BK7
figure
plot(PLoad, BK_2dia, 'd', 'MarkerFaceColor', 'b', 'MarkerEdgeColor', 'b', 'MarkerSize', 6)
hold on
plot(PLoad, BK_500r, 's', 'MarkerFaceColor', '[0.77,0.08,0.20]', 'MarkerEdgeColor',
'[0.77,0.08,0.20]','MarkerSize', 6)
yline(49.6E3,'-','Theoretical YS NiP','LineWidth',2);
ymin = 9.454E3*y;       %multiply vector of 1's by min & max
```

```
ymax = 1.617E4*y;
YS_x = [x;flip(x)];     %create vectors of values going forward, then backward for area
fill
YS_y = [ymax;fliplr(ymin)];
YS_area = fill(YS_x,YS_y,'k','edgecolor','none');   %fill in area with color, remove edges
set(YS_area,'facealpha',.2)     %set transparency
set(gca, 'YScale', 'log')
xlabel('Load (mN)')
ylabel('Hertzian Stress (MPa)')
title('Hertzian Stresses for BK7')
legend('2 um diamond', '500 um ruby', 'Location', 'Northwest')
```

APPENDIX G: MATLAB CODE FOR THE FOMCD OF THE ZYGO FIZEAU VERIFIRE HD & AT

```
%CD for UNCC Zygo Fizeau Verifire HD & AT
close all; clear all;clc;

[top_line,bottom_line,left_line,right_line,lambda,lambda_min_line,lambda_max_line,
slope_line] = ZygoVerifireHD;

figure
X1 = loglog(lambda, top_line, 'k','Linewidth', 2);
hold on
loglog(lambda, bottom_line, 'k','Linewidth', 2);
loglog(lambda_min_line, left_line, 'k','Linewidth', 2);
loglog(lambda_max_line, right_line, 'k','Linewidth', 2);

%%
[top_line,bottom_line,left_line,right_line,lambda,lambda_min_line,lambda_max_line,
slope_line] = ZygoVerifireAT;

X2 = loglog(lambda, top_line, 'b','Linewidth', 2);
loglog(lambda, bottom_line, 'b','Linewidth', 2);
loglog(lambda_min_line, left_line, 'b','Linewidth', 2);
loglog(lambda_max_line, right_line, 'b','Linewidth', 2);
hold off

%Nice to see where the lines are
xlim([10e-5 10e2])
ylim([10e-10 10e1])
text((6*10^-1),(2*10^-1),'\Theta max','FontWeight','Bold','HorizontalAlignment', 'center')
legend([X1, X2], {'Verifire HD', 'Verifire AT'})
xlabel('Aperture (\lambda), mm','FontWeight','Bold');
ylabel('Sag (Z),mm', 'FontWeight','Bold');
set(gca,'Linewidth', 1.5);
ax = gca;
ax.FontSize = 14;

%%function for HD
function[top_line,bottom_line,left_line,right_line,lambda,lambda_min_line,lambda_max
_line, slope_line] = ZygoVerifireHD

%All units in mm
%Zygo Fizeau Verifire HD for TF
%lambda min: 0.1 mm - Nyquist limit
%lambda max: 100 mm largest aperture at UNCC
```

```
%zmax (max PV): 0.5 mm 2kx2k detector, 1000 cycles over 100 mm = 1000/2000
%zmin (min PV): 0.3e-6 mm Zygo Verfire spec sheet- RMS wavefront
%repeatability
%slope limit: .17 deg, comes from calc 1000 waves across aperture at 1/2
%wave = 500 wave*633nm = .3mm. Arcsin(.3/100) = .17 deg

%Stedman diagram values
lambda_min = (.1);  %incl nyquist sampling (or limit)
lambda_max = 100;    %lambda max
z_min = (0.3e-6);     %Zmin
z_max = 0.4;         %Rp
theta_max = .17*(pi/180); %steepest slope that can be meas,
b = 0*(pi/180);       %slope error of angle, put 0 for unknown
n= 1000;          %number of points for the lines

lambda = exp(linspace( log(lambda_min), log(lambda_max), n)); %lambdamin to max w
log spacing (x-values)
slope_line = (theta_max*lambda/(2*pi));
z_max_line = zeros(1,n) + z_max;    %add vector of zeros to make z_max a vector (y-
values)
z_min_line = zeros(1,n) + z_min;    %add vector of zeros to make z_min a vector (y-
values)
lambda_min_line = zeros(1,n) + lambda_min; %add vector of zeros to make lambda_min
a vector (x-values)
lambda_max_line = zeros(1,n) + lambda_max; %add vector of zeros to make
lambda_max a vector (x-values)
slope_err_line = (b*lambda/(2*pi));

top_line  = min([z_max_line;slope_line]); %curvature_line; took out
bottom_line = max([z_min_line; slope_err_line]);
left_line = linspace(bottom_line(1), top_line(1),n); %starts@ 1st element in vector
bottom_line to 1st elem in top_line
right_line = linspace(bottom_line(end), top_line(end),n);
end

%%function for the AT
function[top_line,bottom_line,left_line,right_line,lambda,lambda_min_line,lambda_max
_line, slope_line] = ZygoVerifireAT

%All units in mm
%Zygo Fizeau Verifire HD for TF
%lambda min: 0.1 mm - Nyquist limit
%lambda max: 100 mm largest aperture at UNCC
%zmax (max PV): 0.5 mm 2kx2k detector, 1000 cycles over 100 mm = 1000/2000
%zmin (min PV): 0.3e-6 mm Zygo Verfire spec sheet- RMS wavefront
%repeatability
```

```
%slope limit: .05 deg, comes from calc 300 waves across aperture at 1/2
%wave = 150 wave*633nm = .094mm. Arcsin(.094/100) = .05 deg
%Stedman diagram values
lambda_min = (.2);  %incl nyquist sampling (or limit)
lambda_max = 100;    %lambda max
z_min = (0.4e-6);     %Zmin
z_max = 0.3;         %Rp
theta_max = .05*(pi/180); %steepest slope that can be meas
b = 0*(pi/180);       %slope error of angle, put 0 for unknown
n= 1000;          %number of points for the lines

lambda = exp(linspace( log(lambda_min), log(lambda_max), n)); %lambdamin to max w
log spacing (x-values)
slope_line = (theta_max*lambda/(2*pi));
z_max_line = zeros(1,n) + z_max;    %add vector of zeros to make z_max a vector (y-
values)
z_min_line = zeros(1,n) + z_min;    %add vector of zeros to make z_min a vector (y-
values)
lambda_min_line = zeros(1,n) + lambda_min; %add vector of zeros to make lambda_min
a vector (x-values)
lambda_max_line = zeros(1,n) + lambda_max; %add vector of zeros to make
lambda_max a vector (x-values)
slope_err_line = (b*lambda/(2*pi));

top_line  = min([z_max_line;slope_line]); %curvature_line; took out
bottom_line = max([z_min_line; slope_err_line]);
left_line = linspace(bottom_line(1), top_line(1),n); %starts@ 1st element in vector
bottom_line to 1st elem in top_line
right_line = linspace(bottom_line(end), top_line(end),n);
end
```

APPENDIX H: ILLUMINATION DIAGRAM FOR THE VERIFIRE HD & AT TS

```
%Plot illumination diagram for interferometers HD & AT at UNCC
%there is a f/.75, f/1.5 and f/3.5 all 100 mm aperture
clear all;
clc;
close all;

set(0,'DefaultAxesFontSize', 16);       %sets all graphs to 14 font

%0.75 TS for concave test part (will be in blue)
x_75=[0 1900];
y_75=[0 1900/.75/2];
p_75top = plot(x_75, y_75,   x_75,-y_75, 'Color',[0/255 0/255 255/255], 'Linewidth',2);
%set(get(get(p_75top(2),'Annotation'),'LegendInformation'),'IconDisplayStyle','off');
hold on

%1.5 TS for convex test parts (will be in green)
x1_5cx = [0 121.2]; %creates vector 0-121.2
y1_5cx = [0 121.2/1.5/2]; %creates vector 0-40
p1_5cx = plot(-x1_5cx, y1_5cx,   -x1_5cx, -y1_5cx, 'Color',[0/255 102/255 51/255],
'Linewidth',2);
%set(get(get(p1_5cx(2),'Annotation'),'LegendInformation'),'IconDisplayStyle','off');

%1.5 TS for concave test parts (will be in green)
x1_5cc =[0 1900];
y1_5cc =[0 1900/1.5/2];
p1_5cc = plot(x1_5cc, y1_5cc,   x1_5cc, -y1_5cc, 'Color',[0/255 102/255 51/255],
'Linewidth',2);

%3.5 TS for convex test parts (will be in red)
x3_5cx =[0 122];
y3_5cx =[0 122/3.5/2];
p3_5cx = plot(-x3_5cx, y3_5cx,  -x3_5cx, -y3_5cx, 'Color',[255/255 0/255 0/255],
'Linewidth',2);
set(get(get(p3_5cx(2),'Annotation'),'LegendInformation'),'IconDisplayStyle','off');

%3.5 TS for concave test parts (will be in red)
x3_5cc =[0 1900];
y3_5cc =[0 1900/3.5/2];
p3_5cc = plot(x3_5cc, y3_5cc,  x3_5cc, -y3_5cc, 'Color',[255/255 0/255 0/255],
'Linewidth',2);


%to plot a line at 0 b/t CX and CC parts
```

```
x = [0 0];
y = [-1000 1000];
plot(x, y, '--', 'Color','k')
hold off

legend([p_75top(1) p1_5cc(1) p3_5cc(1)], {'f/.75','f/1.5', 'f/3.5'},'Location','northwest')

xlim([-1000 2500]); ylim([-1500 1500]);
xlabel('Part Radius, mm'); ylabel('Part Aperture, mm');
text(-750,-1350, 'Convex','FontSize',14)
text(750,-1350, 'Concave','FontSize',14)
set(gca,'Linewidth', 1.5);
ax = gca;
ax.FontSize = 14;
```

APPENDIX I: MATLAB CODE FOR COMPUTING STR FOR FIZEAU

```
%3 STR METHODS.
%Written by Kristen Venditti, last edited 10/1/2019
%Method1 fxn - Type A uncertainties, average height and std dev map (de Groot &
Evans)
%Method2 fxn - ISO 25178-604 finds rms difference of two layers and divides by sqrt2
%Method3 fxn - More robust way of ISO 25178,finds the average through the stack,
takes difference of the
%avg from each interferogram (msmt) and then finds the rms, which rms values are
plotted

 %% You must change fname & pr
close all; clear all;clc;

%% Change only these parameters (addpath, objective, optictype, pr, fname)
directory = uigetdir;  %opens dialog box that displays folder & returns path that user
selects
cd(directory);  %change to directory folder
%adds this path (where STR code is stored) so that it can be referenced
addpath 'C:\Users\Kristen\Documents\Grad School\CeFO 20\A2_FOMCD_Instrument
Specs\Experiments for Inteferometers\Matlab code\Verifire';

optictype = sprintf('TF, 14cm');  %'NiP' or 'FS' or  'SiC'
pr = 101.6;                 %4" dia = 101.6 mm,
fname = 'S_14cm';       %change file name here only

filename1 = sprintf('HM_%s',fname);             %height map png
filename2 = sprintf('Hist_AHM_%s',fname); %hist of AHmap
filename3 = sprintf('SD_b4outliers_%s',fname);    %Std dev map png
filename4 = sprintf('Hist_SD_beforeOutliers_%s',fname);
filename5 = sprintf('SD_afterOutliers_%s',fname); %Std dev map png
filename6 = sprintf('Hist_SD_afterOutliers_%s', fname);  %Hist SDM after outliers
filename7 = sprintf('ISO25178_%s', fname);       %ISO method png
filename8 = sprintf('M3_%s', fname);             %method 3 png

set(0,'DefaultAxesFontSize', 14);       %sets all grapsh to 14 font

%%
n = 20;            %enter # of measurements that you're analyzing
for k = 1:n
  filename = sprintf('%s_%d.dat',fname,k); %prints fname for %s and k for %d
  B{k} = ReadZygoBinary(filename)*10^9; %stores data from 1 file in a 1024x1024
matrix
   end
```

```
[avg, sd, sd2, hm_Sa, hm_Sq, hm_rms, hm_Sz, hm_Sz2, pxx, pctile] =
STR_method1_2d_nan_fxn(B);     %fxn to get avg hm and std of all layers

figure %(figure 1)
xya = (0:2304)*(pr/2304);   %changes pixel to resolution = spatial sampling (101.6/2304
= .044 mm/pixel)
imagesc(xya,xya,avg);
c=colorbar;
colormap('jet');
ylabel(c,'nm')
title([optictype, ' - Average Height Map']);
Sa = hm_Sa;
Sq = hm_Sq;
Sz = hm_Sz;
Sz2 = hm_Sz2;
dim = [.6 .4 .5 .5]; %[x y w h] where xy is
s1 = ['Sa = ' num2str(round(Sa,2)) ' nm']; %build string of string, variable, string
s2 = ['Sq = ' num2str(round(Sq,2)) ' nm']; %same as above
s3 = ['Sz = ' num2str(round(Sz2,2)) ' nm'];
stri = {s1, s2, s3};
annotation('textbox', dim, 'String',stri,'BackgroundColor','w','FitBoxToText','on');
xlabel('mm');
ylabel('mm');
saveas(gca, fullfile(directory, filename1),'png'); %saves png in file folder

figure %(figure 2) histogram of avg HM
nbins = 100;
h=histogram(avg,nbins);
title([optictype ' - Hist. of AHM, ']);
%ylabel(
saveas(gca, fullfile(directory, filename2),'png'); %saves png in file folder

figure %(figure3) plots the sd map before outliers are removed
xya = (0:2304)*(pr/2304);  %change pixel to resolution (spatial sampling)
imagesc(xya,xya,sd); c=colorbar; colormap('hot'); ylabel(c,'nm');
title([optictype, ' - Standard Deviation Map  ']);
xlabel('mm');
ylabel('mm');
mean_sdmap = nanmean(nanmean(sd));
saveas(gca, fullfile(directory, filename3),'png');

figure %(figure 4);
nbins = 100;
h=histogram(sd,nbins); %histogram of SD map before removing outliers
title([optictype,' - SDM, ']);
```

```
saveas(gca, fullfile(directory, filename4),'png');

figure %(figure 5) plots sd map after outliers are removed
xya = (0:2304)*(pr/2304);  %change pixel to resolution (spatial sampling)
imagesc(xya,xya,sd2); c=colorbar; colormap('hot'); ylabel(c,'nm');
title([optictype, ' - Standard Deviation Map  ' ]);
xlabel('mm');
ylabel('mm');
mean_sdmap = nanmean(nanmean(sd));
outli = sum(sum(isnan(sd2))); %# of NaNs removed (outliers)
dim = [.6 .4 .5 .5]; %[x y w h] where xy is, doesn't make sense though, trial & error
s4 = ['Outliers = ' num2str(outli)]; %build string of string then variable
stri = {s4};
annotation('textbox', dim, 'String',stri,'BackgroundColor','w','FitBoxToText','on');
saveas(gca, fullfile(directory, filename5),'png');

figure %(figure 6);
nbins = 100;
h=histogram(sd2,nbins); %histogram of SD map removing outliers
title([optictype,' - SDM Outliers Removed ']);
saveas(gca, fullfile(directory, filename6),'png');

[msmts rtmsq] = STR_method2_2d_nan_fxn(B);      %function to get rms/sqrt(2) for
every 2 measurments

 figure; %(figure7)
 plot([1:msmts],(rtmsq),'*');              %plots all values from STR_meth2_rms
 title([optictype, ' - ISO 25178 Method, ' ])
 xlabel('Measurement differences');
 ylabel('Rms divided by square root (nm)');
 avgrms2 = nanmean(rtmsq);
 std2 = std(rtmsq);
 dim = [.6 .4 .5 .5]; %[x y w h] where xy is, doesn't make sense though, trial & error
 s5 = ['Avg rms = ' num2str(round(avgrms2,2)) ' nm']; %build string of string then
variable
 stri = {s5};
 annotation('textbox', dim, 'String',stri,'BackgroundColor','w','FitBoxToText','on');
 saveas(gca, fullfile(directory, filename7),'png');

[rtmsq, n2]= STR_method3_2d_nan_fxn(B);      %function to calc the rms difference

figure; %(figure8)
plot([1:n2],(rtmsq),'*');
title([optictype, ' - RMS of Avg - Msmt '])
xlabel('Measurement');
ylabel('Rms (nm)');
```

```
avgrms3 = nanmean(rtmsq);
s6 = ['Avg rms = ' num2str(round(avgrms3,2)) ' nm']; %build string of string then
variable
stri = {s6};
annotation('textbox', dim, 'String',stri,'BackgroundColor','w','FitBoxToText','on');
saveas(gca, fullfile(directory, filename8),'png');

filename = 'workspace_variables.mat';
save(filename)

% this fxn calculates the average value of each
% layer, saves the avg value in matrix "avg", calculates
% the stdev and plots the stdev

function [avg, sd, sd2, hm_Sa, hm_Sq, hm_rms, hm_Sz, hm_Sz2, pxx, pctile] =
STR_method1_2d_nan_fxn(a)                    %call avg and stdev

[n1 n2]=size(a);                  %n1=not used, n2=#layers,finding size of matrix: 1x20
[n3 n4] = size(a{1});               %size of measurement: 1024x1024

avg = zeros(n3,n4); %creates a place holder for output matrix, all zeros
sd = zeros(n3,n4);
pctile = 65;    %change percentile to make all values > pctile value to be nans

sum = 0;
alldata = [];       %initialize empty vector
for i = 1:n3
   for j = 1:n4
      for k = 1:n2
         msd_vector(k) = a{k}(i,j); %vector of n measurements (down the stack),...
%so this loop will get all the layers for that pixel, but will only show last msmt pixel

      end
      alldata = [alldata,msd_vector]; %appends "msd_vector" to the end of "alldata"
vector
      avg(i,j) = nanmean(msd_vector); %takes mean of stack ignorning nans
                              %taking avg of all the n heights to
                              %get a avg HM
      sd(i,j) = nanstd(msd_vector);   %takes std of stack ignoring nans to get std map
   end
 end
   %pxx value can change
   pxx = prctile(alldata,pctile); %gives percentile value from "alldata" values
   sd2 = sd;
   %replacing any value greater than  w/ a nan, this is to plot this sd2 graph for visual
purposes
```

```
   sd2(sd2 > pxx) = NaN;

%% These are the Surface Parameters for Average Height Map before removing outliers
   hm_Sa = nanmean(nanmean(abs(avg))); %Sa value of avg height map
   hm_Sq = nanstd(alldata);  %Sq, take std of each pixel in stack to get one std for all
pixels in HM
   hm_rms = rms(rms(avg,'omitnan'),'omitnan');  %Sq, take rms of stack to get one rms at
each pixel & then rms of all pixels in map

   max_Sp = abs(max(max(alldata))); %Sp value of all data for avg HM
   min_Sv = abs(min(min(alldata))); %Sv value of all data for avg HM
   hm_Sz = max_Sp - min_Sv; %Sz or PV value of all data for avg HM

   hm_Sz2 = peak2peak(alldata);

%% These are the Sa for Avg HM after removing outliers
%
   avg(avg < -3*hm_Sq | avg > 3*hm_Sq) = NaN; %replacing values outside of +-3*rms
w/ ...
% %                                    %nan to get rid of outliers & make scales similar
%    hm_Sa2 = nanmean(nanmean(abs(avg)));      %Sa 2 after removing outliers

%    hm_rms2 = nanstd(nanstd(avg));    %rms of new avg HM
%
%    %alldata(alldata < -3*hm_Sq | avg > 3*hm_Sq) = NaN;
%    max_Sp2 = abs(max(max(avg))); %Sp value of all data for avg HM
%    min_Sv2 = abs(min(min(avg))); %Sv value of all data for avg HM
%    hm_Sz2 = max_Sp - min_Sv; %Sz or PV value of all data for avg HM
end
%Subtraction method: a fxn finds rms difference of two layers and divides by sqrt2
%the result is a measurement noise Sq and in this case there will be 10
%samples

function [msmts rtmsq] = STR_method2_2d_nan_fxn(B)
[n1 n2] = size(B);
msmts = n2/2;          %#of msmts used (10 in this case)
% p = floor(o);         %#of differences of layers
for k = 1:2:n2           %will run 10x in this case for 20 msmts
   dif =  B{k} - B{k+1};
   rootmeansq = rms(rms(dif),'omitnan');       %rms of each difference vector
   rtmsq(k) = rootmeansq/sqrt(2); %sqrt for every 2 layers storing each ans
%    k = k+2;
end

rtmsq(2:2:end) = [ ];
```

```
%method 3 fxn aka "subtraction technique" finds the average through the stack, takes
difference of the
%avg of all measurements' matrices from each measurment and finds the rms.
%rms values are plotted

function [rtmsq, n2] = STR_method3_2d_nan_fxn(a)

[n1 n2] = size(a);  %size 1x20
[n3 n4] = size(a{1}); %1024x1024

for i = 1:n3
   for j = 1:n4
      for k = 1:n2
         msd_vector(k) = a{k}(i,j);
      end
      avg(i,j) = nanmean(msd_vector);
   end
end

for k = 1:n2
   dif = a{k} - avg;
   rtmsq(k) = rms(rms(dif),'omitnan');
end
```

APPENDIX J: MATLAB CODE FOR PULLING IN ZERNIKE POLYNOMIAL COEFFICIENTS AND PLOTTING

```
%can be used for any zernike coefficient vs tilt
close all; clear all; clc;

%new fiz is zernike fringe w/ piston included, old fiz is listed in excel
old_fizeau = uigetfile('*.csv', 'Old Fizeau data'); %Verifire AT
new_fizeau = uigetfile('*.csv', 'New Fizeau data'); %Verifire HD

Zo = csvread(old_fizeau, 1,0);
Zn = csvread(new_fizeau, 2,1);

%x tilt data for HD in x
xn_tilt = Zn(2:22,2)*(1)/1000; %Zernike coef, divide to get um
xn_coma = Zn(2:22,7); %Zern coef
figure;
plot(xn_tilt, xn_coma, 'b+','linewidth',2)
hold on
%tilt data for AT in x
xo_tilt = Zo(1:16,1)/1000; %Zernike coef
xo_coma = Zo(1:16,6); %Zern coef
plot(xo_tilt, xo_coma, 'r+','linewidth',2)

 %y tilt data for HD in y
yn_tilt = Zn(26:end,3)*(1)/1000; %Zernike coef %divide to get um
yn_coma = Zn(26:end,8); %Zern coef
plot(yn_tilt, yn_coma, 'bo','linewidth',2)
%y tilt data for AT in y
yo_tilt = Zo(17:end,2)/1000; %Zernike coef
yo_coma = Zo(17:end,7); %Zern coef
plot(yo_tilt, yo_coma, 'ro','linewidth',2)
xlabel('Zernike Tilt Coefficient, \mum')
ylabel('Zernike Coma Coefficient, nm')
legend('x-axis, Verifire HD','x-axis, Verifire AT', 'y-axis, Verifire HD ', 'y-axis, Verifire
AT' )
set(0,'DefaultAxesFontSize', 18);       %sets all grapsh to 18 font
%
```